Dissertation

submitted to the
Combined Faculty of Mathematics, Engineering and Natural Sciences
of Heidelberg University, Germany
for the degree of
Doctor of Natural Sciences

Put forward by

Edith Baader

Born in: Troisdorf, Germany

Oral examination: 3rd of June, 2025.

Patient Risk-Minimizing Optimization of Tube Current, Tube Voltage, and Spiral Start Angle in X-Ray Computed Tomography

Referees: Prof. Dr. Mark E. Ladd
Prof. Dr. Marc Kachelrieß

Patient Risk-Minimizing Optimization of Tube Current, Tube Voltage, and Spiral Start Angle in X-Ray Computed Tomography

This thesis proposes two automatic exposure control (AEC) techniques to reduce the radiation risk of computed tomography (CT) scans for patients. Modern AEC includes the selection of a constant tube voltage and tube current modulation (TCM) meaning that the tube current is adjusted per projection angle and longitudinal position. While conventional TCM minimizes the tube current time product as a surrogate for patient dose, TCM methods minimizing a risk measure (riskTCM) such as the effective dose have been proposed. This thesis proposes a risk-minimizing tube current and tube voltage modulation (riskTCTVM). For simulated circular scans, riskTCTVM showed effective dose decreases of less than 1 % at constant noise for unenhanced scans and up to 35 % at constant contrast-to-noise ratio for iodine-enhanced scans compared to riskTCM. The second proposed technique is an optimized tube start angle selection that decreases the effective dose especially for spiral scans with high pitch values, i.e. for high table increments per tube rotation compared to the scanner's collimation. For a collimation of 80 mm and a pitch value of 3, the mean reduction in effective dose was in simulations 16 % compared to the mean dose over all start angles which models current clinical practice with a random start angle.

Patientenrisiko-minimierende Optimierung von Röhrenstrom, Röhrenspannung und Spiralstartwinkel für die Röntgen-Computertomographie

In dieser Dissertation werden zwei Techniken zur automatischen Belichtungssteuerung (AEC) vorgeschlagen, um das Strahlenrisiko von Computertomographie (CT) Scans für Patienten zu reduzieren. Die moderne AEC umfasst die Wahl einer konstanten Röhrenspannung sowie die Röhrenstrommodulation (TCM), d.h. dass der Röhrenstrom an den Projektionswinkel und die longitudinale Position angepasst wird. Während die herkömmliche TCM das Röhrenstrom-Zeit-Produkt als Surrogat für die Patientendosis minimiert, wurden TCM-Methoden vorgeschlagen, die ein Risikomaß wie die effektive Dosis minimieren (riskTCM). Diese Arbeit schlägt eine risikominimierende Röhrenstrom- und Röhrenspannungsmodulation (riskTCTVM) vor. Für simulierte Kreisscans zeigte riskTCTVM eine Verringerung der effektiven Dosis im Vergleich zu riskTCM um weniger als 1 % bei konstantem Rauschen für Nativscans und bis zu 35 % bei konstantem Kontrast-zu-Rausch-Verhältnis für Scans mit Jod als Kontrastmittel. Die zweite vorgeschlagene Technik ist eine optimierte Auswahl des Startwinkels der Röhre, die die effektive Dosis insbesondere bei Spiralscans mit hohen Pitchwerten, d.h. bei hohem Tischvorschub pro Röhrenumdrehung im Vergleich zur Kollimierung des Scanners, reduziert. Für eine Kollimierung von 80 mm und einem Pitchwert von 3 betrug die mittlere Reduktion der effektiven Dosis in Simulationen 16 % im Vergleich zur mittleren Dosis über alle Startwinkel, was die aktuelle klinische Praxis mit einem zufälligen Startwinkel modelliert.

Contents

List of Acronyms

AEC . . . . . Automatic exposure control

ALARA . . . . . As low as reasonably achievable

ATVS . . . . . Automatic tube voltage selection

CNR . . . . . Contrast-to-noise ratio

CNRD . . . . . Dose-weighted contrast-to-noise ratio

CT . . . . . Computed tomography

CTDI . . . . . CT dose index

DLP . . . . . Dose-length-product

DSCT . . . . . Dual source CT

FOM . . . . . Field of measurement

HU . . . . . Hounsfield units

ICRP . . . . . International Commission on Radiological Protection

LNT . . . . . Linear-non-threshold

mAsTCM . . . . . mAs–minimizing tube current modulation

noTCM . . . . . Constant tube current

osTCM . . . . . Organ-specific tube current modulation

PMMA . . . . . Polymethyl methacrylate

riskTCM . . . . . Risk–minimizing tube current modulation

riskTCTVM . . . . . Risk–minimizing tube current and tube voltage modulation

SSCT . . . . . Single source CT

TCM . . . . . Tube current modulation

TVM . . . . . Tube voltage modulation

List of Tables

List of Figures

1 Introduction

Medical imaging has become essential for a wide range of medical diagnostics as well as treatment planning and guidance. Whereas several imaging techniques have been developed since the discovery of X-rays and are now routinely used, X-ray imaging techniques still have a crucial role in medical imaging. While X-ray radiographs provide a two-dimensional projection through the patient body, X-ray computed tomography (CT) offers a three-dimensional reconstruction of the patient volume based on X-ray projections taken from a range of view angles. Nowadays, CT scans can be acquired in submillimeter spatial resolution [1], thus allowing to visualize tiny structures. Furthermore, due to the advancements in scan speed, whole-body CT scans can nowadays acquired in a few seconds which is beneficial for example for oncologic staging and trauma imaging [2]. The high temporal and spatial resolution of CT even allows the use of CT for cardiac imaging applications [3].

The use of CT, however, is accompanied by concerns regarding radiation dose. The employed X-rays are ionizing radiation that can have negative effects on the human body. Typically, the received doses during one CT scan are in the range of a few millisieverts [4] and are therefore in the order of the annual global average dose per person received from natural sources which is about 2.4 mSv [5]. For such small dose levels, no direct harmful tissue reactions have been observed but stochastic effects such as the induction of cancer are of concern. However, the risk for these stochastic effects is hard to quantify in epidemiological studies [6]. Therefore, as the exact risk for these low doses is not clear, assumptions about the risk have to be made for radiation protection purposes. A common procedure is to extrapolate risk data for higher radiation doses to these small dose values [7] under the assumption that the associated risk is proportional to the received dose. This assumption is called the linear-non-threshold (LNT) model [8]. The LNT model hence assumes that any small dose increases the radiation risk. Following the LNT model therefore implies that the radiation exposure in medical examinations should be as low as reasonably achievable (ALARA) [9] since for large numbers of people undergoing CT scans, even a small risk per scan could result in a notable number of cancer cases [7].

To comply with the ALARA principle, there are different strategies to reduce the dose of CT scans. These strategies can broadly be divided into three categories, namely strategies aiming to improve X-ray detection, image reconstruction, and radiation exposure. Ideally, all strategies should be combined to achieve the highest dose reduction. The detection of X-rays, for example, was improved by developing detectors with

less electronic noise [2]. Less noise in the projection data leads to less noise in the reconstructed image which allows the reduction of the tube current of the X-ray tube and thus the dose of a scan. This is due to the inverse relationship of tube current and noise, i.e. a higher tube current leads to less noise, and due to the fact that the dose is proportional to the tube current. Similarly, scan dose can be decreased if image noise is reduced directly by the reconstruction. Advancements in reconstruction techniques include for example iterative reconstruction techniques and deep learning-based image reconstruction [2], [3]. An apparent strategy to reduce radiation exposure is appropriate collimation to expose the patient only to X-rays whose signal will be used for reconstruction. Furthermore, low-energy photons with a low probability of reaching the detector can be removed from the spectrum by prefilters [3]. Moreover, modern scanners employ so-called automatic exposure control (AEC) techniques. This thesis proposes two new approaches to existing AEC techniques.

Modern AEC techniques include automatic tube voltage selection (ATVS) and tube current modulation (TCM). The tube voltage affects the photon's energy spectrum. With increasing voltage, the energy spectrum is shifted to higher energies and the maximum photon energy is increased. Which voltage results in the lowest dose at constant image quality depends on patient thickness and whether a contrast agent is present. The tube current instead determines the photon flux of the X-ray beam. As the tube current directly influences the image noise, the tube current should be set just high enough to achieve the required noise level. Furthermore, it has been shown to be beneficial to adjust the tube current to the X-ray projection, especially if different projections exhibit high differences in attenuation [10], [11]. This principle, i.e. to adapt the tube current to the projection and thus modulate the tube current as a function of tube position, is called TCM. Conventional TCM implementations on clinical scanners minimize the tube current time product of the scan. However, while radiation dose is proportional to the tube current, the radiation risk is also influenced by the irradiated organs as different organs respond differently to radiation. Therefore, TCM implementations aiming to reduce the dose to certain radiosensitive organs such as the breast or the thyroid are also common in clinical scanners [12]–[14]. Also techniques minimizing a risk metric such as the effective dose, which is a weighted sum of organ doses, have been proposed [15], [16]. Reference [15] shows that such risk-minimizing TCM is beneficial for all anatomical regions with mean effective dose reductions from about 10 % for the head and 30 % for the abdomen compared to conventional TCM at constant image quality. However, as on clinical CT scanners, the tube voltage remains constant with this approach. Therefore, the first approach in this thesis extends the risk-minimizing TCM by a voltage modulation, i.e. tube current and tube voltage are simultaneously optimized to reduce the effective dose at constant image quality.

The second approach in this thesis aims to reduce the effective dose by an optimal selection of the tube start angle in spiral CT scans. In current clinical practice, the tube start angle is not controlled and can be considered a random scan parameter. However, studies have shown the effect of the tube start angle on individual organ doses and an optimal selection of the tube start angle to reduce the dose to single organs has been considered [17], [18]. The second approach in this thesis extends this idea to a reduction

of the effective dose by an optimization of the tube start angle.

The thesis is structured as follows: the second chapter introduces aspects of X-ray physics and CT techniques that are fundamental to this work. The third chapter presents the proposed risk-minimizing tube current and tube voltage modulation and the fourth chapter the start angle optimization. Both chapters contain a more detailed introduction to the topic, a description of the used materials and methods, and the results. The thesis concludes with a summary and discussion as the fifth chapter and conclusions as the sixth chapter.

2 X-Ray Physics and CT Techniques

This chapter reviews concepts of X-ray physics and CT techniques that form the basis for this thesis. The chapter is primarily based on reference [1] and the reader is referred to this book chapter for a more general introduction to CT.

CT scanners measure the attenuation of X-rays for different view angles of an object and reconstruct the spatial distribution of the attenuation coefficient for this object. This principle allows to create cross-sectional images of patients for medical imaging. Section 2.1 introduces the X-ray interactions with matter which result in the attenuation of X-rays and the deposition of radiation dose in the scanned patient for the clinical X-ray energy range. Section 2.2 outlines the setup of a clinical CT scanner with the principal components for the measurement of X-ray attenuation. Section 2.3 describes the CT reconstruction technique from the measured attenuation data that is considered in this thesis. Section 2.4 presents and discusses quantities of radiation dose and radiation risk for the scanned patient and section 2.5 describes exposure control techniques relevant to this thesis that are already in clinical practice or have been proposed to reduce the radiation risk of CT scans.

2.1 X-Ray Interactions with Matter

Beer-Lambert Law

X-ray photons interact with a certain probability when traversing matter. For a thin monochromatic X-ray beam with energy E, the number of photons N that traverse a thin homogeneous absorber with linear attenuation coefficient μ and thickness d on a straight line can be described by the Beer-Lambert law [19]–[22]:

$$N = N_0 e^{-\mu(E)d}. \tag{2.1}$$

Here, N_0 denotes the initial number of photons of the X-ray beam and N the average number of photons that traverse the absorber without interaction. All other photons either scatter or get absorbed [1].

The attenuation coefficient $\mu(E)$ is material-dependent. For inhomogeneous materials with location-dependent attenuation coefficient $\mu(E, \boldsymbol{r})$ like the human body, the

exponent $\mu(E)d$ in equation (2.1) has to be replaced by a line integral:

$$N = N_0 e^{-\int d\lambda\ \mu(E, \boldsymbol{s} + \lambda\boldsymbol{\Theta})} \tag{2.2}$$

where $\boldsymbol{s}$ denotes the considered starting point and $\boldsymbol{\Theta}$ the direction of the X-ray [1].

X-Ray Interactions

For the photon energies in clinical CT with energies up to 150 keV, three types of interactions contribute to the photon attenuation described by equation (2.2). These interactions are Rayleigh scattering, Compton scattering, and the photoelectric effect [22]:

- Rayleigh scattering denotes the elastic scattering of the photon with an atom meaning that the photon changes its direction without energy transfer. The attenuation coefficient of Rayleigh scattering rises with the atomic number and strongly decreases with photon energy.
- Compton scattering describes the inelastic scattering with a weakly bound electron in which part of the photon's energy is transferred to the electron. The probability for Compton scattering decreases with increasing photon energy but the relative energy transfer rises with photon energy.
- In the case of the photoelectric effect, the photon interacts with the whole atom and transfers its energy to an atomic electron which is released. The kinetic energy of the released electron is the photon's energy minus the binding energy of the electron. However, the probability of the photoelectric is the highest when the photon's energy is equal to or slightly higher than the binding energy which leads to edges in the energy dependence of the attenuation coefficient at the respective binding energies. Furthermore, the photoelectric attenuation coefficient μ_{photo} strongly decreases with photon energy E, i.e. $\mu_{\text{photo}} \propto E^{-3}$, and strongly increases with the atomic number Z of the material, i.e. $\mu_{\text{photo}} \propto Z^{3-4}$. The strong dependence on the atomic number is especially relevant for the imaging of bones surrounded by soft tissue.

The total attenuation coefficient $\mu(E)$ is the sum of the individual attenuation coefficients of these interactions. For all interaction processes, the linear attenuation coefficient rises linearly with the density of the material. Figure 2.1 shows the contribution of the three interactions to the attenuation coefficient $\mu(E)$ of water divided by the water density; the attenuation of water is important in the imaging of patients as water is a predominant material in the human body. For small photon energies, the photoelectric effect is the dominant cause of attenuation whereas the Compton effect dominates for higher energies. The contribution of Rayleigh scattering is minor. Furthermore, figure 2.1 shows the comparison of the linear attenuation coefficient of water to the one of bone and iodine. Iodine is relevant for medical imaging as iodine is a common

contrast medium that is administered to patients to increase the contrast of structures of diagnostic interest.

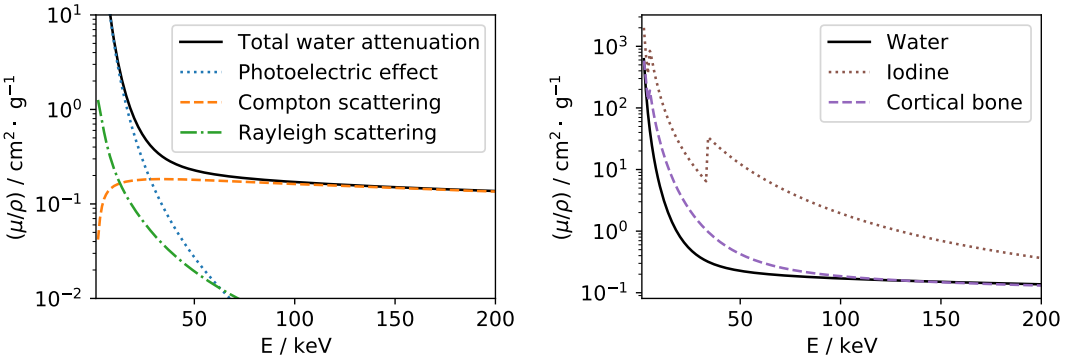

Figure 2.1: Comparison of the contribution of Rayleigh scattering, Compton scattering, and photoelectric effect to the total attenuation coefficient μ of water divided the water density ρ as a function of photon energy E (left) and the comparison of the attenuation of water, bone, and iodine (right). Attenuation data was taken from reference [23] and the composition of skeleton cortical bone from reference [24].

2.2 CT Scanner Setup

2.2.1 Scanner Geometry

Figure 2.2 shows a sketch of the geometry of a clinical scanner with its basic components to measure the X-ray attenuation. The X-rays are produced by an X-ray tube and traverse a system of prefilters before impinging on the patient. Behind the patient, the detector is located which detects the photons that passed through the patient. Both the X-ray tube and the detector rotate around the isocenter to generate attenuation data for different view angles that is necessary for reconstruction. The distance from the X-ray tube to the isocenter is denoted with R_F and the distance from the isocenter to the detector with R_D. The sum of both distances, that is, the distance from the X-ray tube to the detector is denoted with $R_\mathrm{FD} = R_\mathrm{F} + R_\mathrm{D}$. The field of measurement (FOM) for which the attenuation distribution can be reconstructed for this setup is displayed in light gray. The following subsections describe the X-ray tube, the collimation and prefiltration of the X-rays, the detector, and common scan trajectories in more detail.

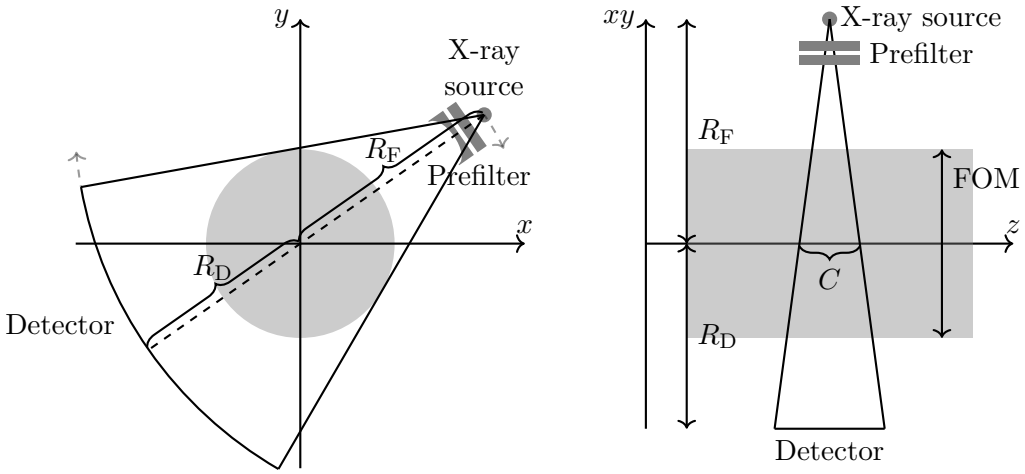

Figure 2.2: Sketch of the lateral (left) and longitudinal geometry (right) of a clinical CT scanner.

2.2.2 X-Ray Tube

The general working principle of an X-ray tube is based on the acceleration of electrons towards the anode which subsequently leads to the generation of X-rays by interactions of the electrons with the anode material. The electrons are released by the cathode, a current-carrying filament and the number of released electrons is proportional to the applied tube current [1]. The electrons are then accelerated in vacuum towards the anode by the applied acceleration voltage U which is called tube voltage in the following. The tube voltage causes an acceleration up to a final kinetic energy of $E_{\text{kin}} = eU$ where e denotes the electric charge of an electron [25]. In clinical practice, tube voltages between 80 kV and 140 kV are common but also 70 kV and 150 kV are available in certain systems [1]. When the electrons hit the anode, two forms of processes lead to the generation of X-rays. The first one is the so-called bremsstrahlung: in the electric field of the atomic nuclei, the electrons are decelerated and emit photons which carry part of their kinetic energy [25]. The energy spectrum of these photons is continuous with the maximum energy being equal to the kinetic energy of the electrons E_{kin} before the interaction [25], i.e. is for a voltage of $U = 120\,\text{kV}$ for example, the maximum photon energy is 120 keV. The second process occurs when electrons hit atomic electrons which are then ejected from the atom. The vacancy in the respective shell is subsequently filled by an electron of a higher shell which releases a photon during the transition; the energy of the photon equals the difference in binding energy of the respective shells [25]. Thus, the photons created by this process only have certain energies which is why these photons are called characteristic X-ray radiation. Figure 2.3 shows a typical X-ray spectrum with continuous bremsstrahlung spectrum and characteristic peaks.

However, about 99 % of the electrons' energy is transferred by Coulomb interactions with atomic orbital electrons of the anode; these interactions do not produce X-ray photons but heat the anode [25]. This heating requires the cooling of the anode and a

limit on the applied tube current to prevent the anode from overheating and to increase the lifetime of the anode [1]. Modern X-ray tubes in clinical scanners allow the user to choose tube currents up to 1300 mA [3]. Furthermore, the maximum available tube current set by the vendors decreases with scan time [1].

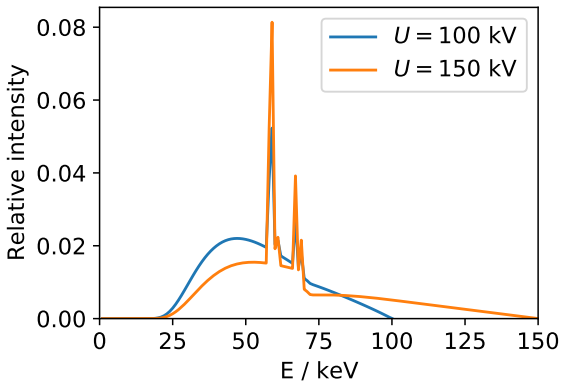

Figure 2.3: X-ray spectra simulated based on a semiempirical model [26] for tube voltages U of $U = 100\,\mathrm{kV}$ (in blue) and $U = 150\,\mathrm{kV}$ (in orange). Prefiltration was modeled with 6 mm aluminum as in chapters 3 and 4. Both spectra were normalized to unit area.

2.2.3 Collimation and Prefiltration

Only the photons reaching the detector contribute to the signal measured by the detector which is used for image reconstruction. Therefore, the X-ray beam is collimated in a way that the patient is only exposed to X-rays directed towards the detector. In cases where not all data measured by the detector is used for reconstruction, for example at the beginning and end of a spiral scan, dynamic collimators are used that block unused radiation [27].

Furthermore, the X-rays traverse a system of prefilters before impinging on the patient. As for the collimation, the goal is that the patient is spared from unusable radiation [1]. As the attenuation coefficient rises with decreasing energy (compare figure 2.1), the probability for low-energy photons is low to pass the patient and reach the detector. Prefilters absorb these photons with a higher probability than photons with higher energy and thus harden the spectrum, i.e. the mean energy of the spectrum is increased.

Moreover, X-rays passing through the periphery of the patient have a shorter path through the patient and are less attenuated than X-rays passing through the central regions of the patient. Therefore, less photons are necessary to achieve the same signal-to-noise ratio for periphery regions. This is considered by bowtie filters whose thickness is higher for larger angles in the X-ray fan than for central angles of the fan beam [1] (compare figure 2.2).

2.2.4 Detectors

The detector segment behind the patient is divided into several detector pixels to measure the attenuation of X-rays that traversed the patient along different lines. In most clinical scanners today, the detection mechanism of these detector pixels is based on scintillators such as gadolinium oxysulfide (Gd_2O_2S) [1]. In the scintillator, the X-ray photons are converted into optical photons which are detected by a photodiode. The amount of optical photons and thus the registered signal at the photodiode is proportional to the energy of the incoming photon; the detector signal is hence weighted by the photon's energy. Furthermore, the rate of incoming photons hitting on one detector pixel in CT is higher than the temporal resolution of today's clinical scintillator-based detectors so that the signals of several photons add up in the detector [1]. Therefore, this type of detector is called energy-integrating detector.

In 2021, Siemens released the first clinical scanner with photon-counting detectors [28]. These detectors are based on semiconductors that convert an X-ray photon directly into an electric signal proportional to the detected photon's energy [1]. This signal acquisition is short enough that single photons can be detected and counted. The use of photon-counting detectors has several advantages including a higher radiation dose efficiency compared to energy-integrating detectors [29]–[31]. However, the use of photon-counting detectors in clinical CT systems is still fairly new, and energy-integrating detectors are still the predominant type of detectors. In this thesis, an energy-integrating detector is considered.

2.2.5 Scan Trajectories

The reconstruction of a CT image requires measurements of the X-ray attenuation from a range of view angles of the patient. In the first CT scanners, this was achieved by a circular trajectory of the X-ray tube and the detector [1], that is, the X-ray tube and the detector rotate around the patient while the patient table is fixed. With such a scan, only the region inside the collimation of the scanner can be imaged. To increase the longitudinal coverage, several circular scans can be performed; between those scans, the patient table is moved along the longitudinal axis. This procedure is called sequence scan [1]. Since the development of scanners enabling a continuous rotation of X-ray tube and detector in the late 80s, spiral trajectories were introduced which are commonly used nowadays [1]. In spiral trajectories, the X-ray tube rotates continuously while the patient table is moved with a constant speed. Thus, from the patient's perspective, the X-ray tube follows a spiral trajectory. A characteristic property of spiral trajectories is the pitch value p. The pitch value $p = d/C$ relates the table increment d during one rotation to the collimation C at the isocenter.

2.3 CT Reconstruction

As described in the previous section, CT scanners acquire X-ray images for a range of view angles. This section introduces the reconstruction process from the acquired

X-ray images to CT images. Subsection 2.3.1 describes how approximate line integrals can be retrieved from the detector measurements by preprocessing steps including water precorrection. Subsection 2.3 presents the basic analytical reconstruction method, namely filtered back projection in parallel beam geometry. Subsection 2.3.3 discusses how filtered back projection can be performed in fan beam geometry, which corresponds to the geometry in clinical CT scanners which is considered in this thesis. Finally, subsection 2.3.4 introduces Hounsfield units, the unit that is used to display the result of the reconstruction.

2.3.1 Preprocessing With Water Precorrection

In the monochromatic case, the line integral of the attenuation coefficient can be retrieved by calculating the negative logarithm of the measured signal relative to the signal without the object (compare equation (2.2)):

$$\int d\lambda \; \mu(\boldsymbol{s} + \lambda\boldsymbol{\Theta}) = -\ln \frac{N}{N_0}.$$

As discussed in subsection 2.2.4, conventional energy-integrating detectors do not count the photon numbers N and N_0 but the detected signal is proportional to the energy. Hence, for a monochromatic X-ray beam the fraction of the detector signals with and without object should equal the fraction of the photon numbers N and N_0. However, the signal at the detector is the integral of photons with different energies. The polychromatic projection value q, that is the logarithm of the detected signal normalized to the signal without object, can be modeled by the following expression:

$$q = -\ln \int dE w(E) e^{-\int d\lambda \; \mu(E, \boldsymbol{s} + \lambda\boldsymbol{\Theta})}. \tag{2.3}$$

Here, $w(E)$ denotes the detected spectrum without the scanned object normalized to one which can be modeled by

$$w(E) \propto \underbrace{n(U,E)}_{\text{tube spectrum}} \cdot \underbrace{e^{-\sum_i \mu_{\mathrm{PF}_i}(E) \cdot d_{\mathrm{PF}_i}}}_{\text{prefilter}} \cdot \underbrace{E \cdot (1 - e^{-\mu_{\mathrm{D}}(E) d_{\mathrm{D}}})}_{\text{detector}}.$$

The first term refers to the emitted spectrum by the X-ray tube which is governed by the applied tube voltage (compare figure 2.3). The second term describes the attenuation by prefilters, here abbreviated with PF. The last term models the detector including the proportional energy weighting in energy-integrating detectors and the probability for the photons to get detected. The probability for detection can be modeled by the probability to interact with the detector material which is the counter probability of no interaction given by the Beer-Lambert law.

To retrieve line integrals for reconstruction, the expression of the measured polychromatic projection value q (compare equation (2.3))) can be simplified under the

assumption that the scanned object consists of only one material; in clinical CT, this material is water as an approximation for the human body. Following this assumption of only one material present, the attenuation coefficient can be decomposed into an energy-dependent part $\psi(E)$ and a location-dependent part $f(\boldsymbol{r})$ [1]. A possible choice is for example $\psi(E) = \left(\frac{\mu}{\rho}\right)(E)$ and $f(\boldsymbol{r}) = \rho(\boldsymbol{r})$ but modifications, for example including a normalization factor are possible and can be useful. The decomposition into $\psi(E)$ and $f(\boldsymbol{r})$ gives

$$q = -\ln \int dE w(E) e^{-\psi(E) \int d\lambda \; f(\boldsymbol{s} + \lambda \boldsymbol{\Theta})} \tag{2.4}$$

$$= -\ln \int dE w(E) e^{-\psi(E) p} \quad \text{with} \quad p = \int d\lambda \; f(\boldsymbol{s} + \lambda \boldsymbol{\Theta}). \tag{2.5}$$

In the second step, the line integral was replaced by the value p which is called the projection value in the following. The relation between p and q is non-linear and cannot be solved analytically. However, the function $q(p)$ is monotonously increasing and can be inverted numerically or by a look-up table. Hence, the measured polychromatic projection values q can be converted into monochromatic values p which can then be used for reconstruction. This conversion from polychromatic to monochromatic projection values is necessary because so-called cupping artifacts appear if the polychromatic projection value q is used for reconstruction (compare figure 2.4). These artifacts appear because the function $q(p)$ is concave [1], i.e. q increases slower than p and short intersections appear disproportionate more attenuating than higher intersections. As a result, peripheral regions appear more attenuating than central regions (compare figure 2.4). Due to the assumption that the patient consists only of water, the correction of these artifacts by converting from q to p prior to reconstruction is called water precorrection.

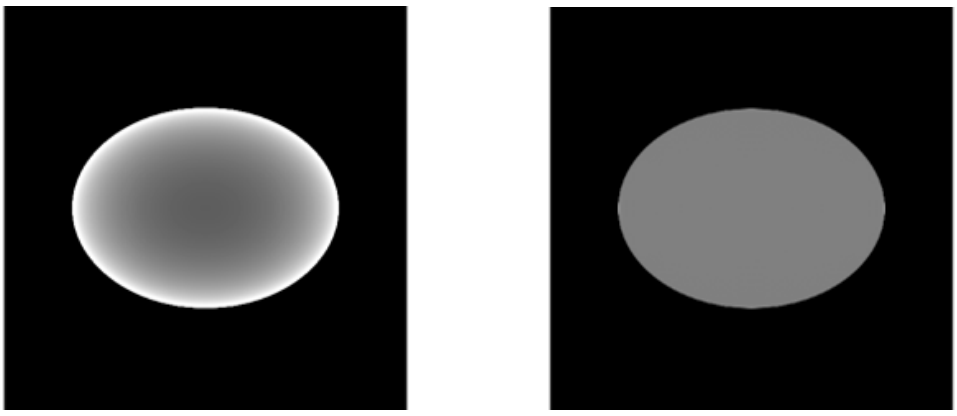

Figure 2.4: Simulation of an ellipse-shaped water phantom reconstructed without water precorrection (left) and with water precorrection (right). Without water precorrection, the edges of the phantom appear brighter, i.e. more attenuating than the central region.

2.3.2 Reconstruction in Parallel Beam Geometry

The monochromatic line integrals defined by equation (2.5) can be used to reconstruct the spatial distribution of the function f which is linked to the attenuation coefficient. In parallel beam geometry, which is assumed in the following, a volume is reconstructed slice by slice. Hence, the problem is reduced to a two-dimensional problem. The X-rays can then be parameterized by their angle ϑ and their distance ξ to the isocenter (compare figure 2.5). This gives the relation $\xi = x\cos\vartheta + y\sin\vartheta$. Hence, the line

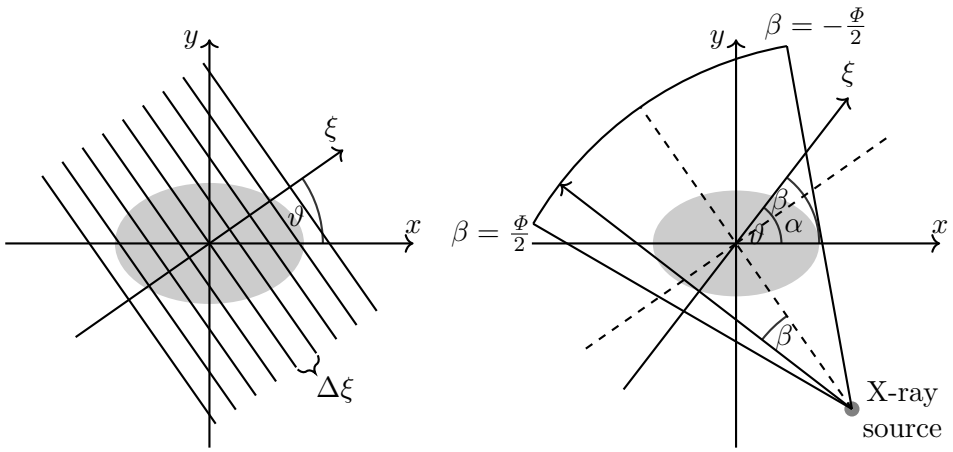

Figure 2.5: Sketch of the coordinate systems for the parallel beam geometry (left) and the fan beam geometry (right). The sketch of the fan beam geometry is inspired by reference [32].

integral can be rewritten as

$$\begin{aligned} p(\vartheta,\xi) &= \int d\lambda f(\boldsymbol{s}+\lambda\boldsymbol{\Theta}) \\ &= \int dxdyf(x,y)\delta(x\cos\vartheta + y\sin\vartheta - \xi). \end{aligned}$$

The set of all possible line integrals is called Radon transformation which was originally introduced in reference [33]. Reference [33] also includes an inverse transform to retrieve the function f. Here, we follow the derivation of this inverse transform as presented in reference [1].

A useful result for reconstructing $f(x,y)$ gives the Fourier transform of $p(\vartheta,\xi)$:

$$\begin{aligned} P(\vartheta,\xi) &= \int d\xi p(\vartheta,\xi)\cdot e^{-2\pi iu\xi} \\ &= \int dxdyf(x,y)\cdot e^{-2\pi iu(x\cos\vartheta + y\sin\vartheta)} \end{aligned}$$

Comparing this result with the two-dimensional Fourier transform F of f

$$F(u_x, u_y) = \int dxdy f(x,y) \cdot e^{-2\pi i(u_x x + u_y y)}$$

shows that the one-dimensional Fourier transform $P(\vartheta, \xi)$ is equal to the two-dimensional Fourier transform F of f with $u_x = u\cos\vartheta$ and $u_y = u\cos\vartheta$:

$$P(\vartheta, \xi) = F(u\cos\vartheta, u\cos\vartheta).$$

This relation is known as the Fourier-slice-theorem. In principle, this relation could be used directly to reconstruct $f(x,y)$. However, the measured data are discrete and on a polar grid. Hence, a gridding from polar coordinates to Cartesian coordinates would be necessary before the inverse Fourier transform. Instead, the following analytical steps can be performed. The inverse Fourier transform in polar coordinates with $u_x = u\cos\vartheta$ and $u_y = u\cos\vartheta$ and thus $du_x du_y = |u| du d\vartheta$ gives

$$f(x,y) = \int_0^\pi d\vartheta \int_{-\infty}^{\infty} du|u| P(\vartheta, u) e^{-2\pi i u(x\cos\vartheta + y\sin\vartheta)} \tag{2.6}$$

$$= \int_0^\pi d\vartheta \int_{-\infty}^{\infty} du K(u) P(\vartheta, u) e^{-2\pi i u(x\cos\vartheta + y\sin\vartheta)}. \tag{2.7}$$

The introduction of $K(u)$ in the second line helps to recognize that the convolution theorem can be applied which states that the Fourier transform of the convolution of two functions g_1 and g_2

$$(g_1 * g_2)(x) = \int dy\ g_1(y) g_2(x-y)$$

is equal to the multiplication of the respective Fourier transforms G_1 and G_2:

$$\mathsf{F}(g_1 * g_2) = (\mathsf{F}g_1)(\mathsf{F}g_2) = G_1 G_2. \tag{2.8}$$

Taking the inverse Fourier transform of equation (2.8) gives

$$g_1 * g_2 = \mathsf{F}^{-1}((\mathsf{F}g_1)(\mathsf{F}g_2)) = \mathsf{F}^{-1}(G_1 G_2)$$

and equation (2.7) can be rewritten as

$$f(x,y) = \int_0^\pi d\vartheta p(\vartheta, \xi) * k(\xi)|_{\xi = x\cos\vartheta + y\sin\vartheta} \tag{2.9}$$

Hence, $f(x,y)$ can be reconstructed by the convolution of the projection data $p(\vartheta, \xi)$ with the so-called reconstruction kernel

$$k(\xi) = \mathsf{F}^{-1} K(u) = \int du|u| e^{2\pi i u\xi} = \frac{-1}{2\pi^2 \xi^2}$$

and the subsequent backprojection of the filtered projection data into the image.

The discrete form of the reconstruction kernel can be calculated to

$$k_m = \begin{cases} (2\Delta\xi)^{-2} & \text{if } m = 0, \\ -(\pi m \Delta\xi)^{-2} & \text{if } m \in 2\mathbb{Z}+1, \\ 0 & \text{otherwise.} \end{cases}$$

According to equation (2.9), projection data from 180° are necessary for the reconstruction. The inverse operation, that is obtaining projection data from an object as it occurs in a CT scanner, is called forward projection.

2.3.3 Reconstruction in Fan Beam Geometry

In clinical CT, the X-rays are emitted in a fan beam. In fan beam geometry, the lines from the X-ray tube to the detector can be parameterized by the tube angle α and the angle within the fan β (compare figure 2.5). The relation to the coordinates in parallel beam geometry is given by the following equations

$$\vartheta = \alpha + \beta \quad \text{and} \quad \xi = -R_\mathrm{F} \sin\beta.$$

Thus, every line described by (ϑ, ξ) in parallel geometry can be related to a line (α, β) in fan beam geometry and the conversion from parallel beam geometry to fan beam geometry can be performed by rebinning. This is the most convenient procedure and the one considered in this thesis. Other options include a coordinate transform or modifications of the convolution process in equation (2.9) [1]. To fulfill the condition that projection data from 180° are necessary for the reconstruction in parallel geometry, it follows for the fan beam geometry that projection data for angles of α for 180° plus the fan angle Φ are necessary (compare figure 2.6).

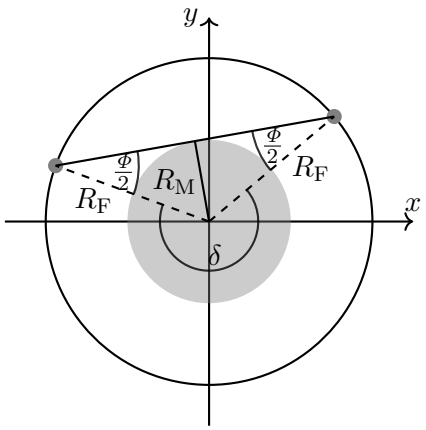

Figure 2.6: Sketch of the acquisition requirement for the fan beam geometry. The black circle represents the circular trajectory of the X-ray tube and the gray circle the FOM with R_{M} =FOM/2. For a ray emitted at half the fan angle Φ at a tube angle α, the tube has to travel $\delta = 360° - (180° - \Phi) = 180° + \Phi$ to emit the corresponding complementary ray so that every point in the FOM is covered by 180° in parallel beam geometry.

2.3.4 Hounsfield Units

For a more intuitive interpretation of the reconstructed attenuation values, the attenuation data are usually displayed in Hounsfield units (HU) which defines a scale relative to the attenuation of water:

$$CT(\boldsymbol{r}) = \frac{\mu(\boldsymbol{r}) - \mu_{\mathrm{Water}}}{\mu_{\mathrm{Water}}} \cdot 1000 \text{ HU}.$$

This definition of the so-called CT value results in water having a CT-value of zero and air of -1000 HU. Dividing the attenuation value into the material-dependent part and the density and assuming that there is water at the location $\boldsymbol{r}$, the CT value can also be interpreted as a density value:

$$CT(\boldsymbol{r}) = \frac{\psi_{\mathrm{Water}} \cdot \rho(\boldsymbol{r}) - \psi_{\mathrm{Water}} \cdot \rho_{\mathrm{Water}}}{\psi_{\mathrm{Water}} \cdot \rho_{\mathrm{Water}}} \cdot 1000 \text{ HU} = \frac{\rho(\boldsymbol{r}) - \rho_{\mathrm{Water}}}{\rho_{\mathrm{Water}}} \cdot 1000 \text{ HU}.$$

A CT-value of -1000 HU then relates to a density of zero, a CT-value of zero equal to the density of water, and a CT-value of 1000 HU equal to twice the density of water.

The CT-values are usually displayed as grayscale values. Characteristic for the display is the center C and the width W; all values below $C - W/2$ are displayed black and all values above $C + W/2$ white. For all values between $C - W/2$ and $C + W/2$, the brightness increases linearly from black to white.

2.4 Radiation Dose and Radiation Risk

This section introduces basic dose metrics and discusses their link to radiation risks for patients. The section closes with a review of the dose measures currently used to evaluate of CT scan dose levels.

2.4.1 Dose Metrics

Absorbed dose The basic quantity in radiation dosimetry is the absorbed dose D which is defined by the mean energy deposit $d\epsilon$ to an infinite small mass element dm [22]

$$D = \frac{d\epsilon}{dm}.$$

The unit of the absorbed dose is Gray (Gy) where one Gray is defined as one Joule per kilogram, that is 1 Gy=1 J kg^{-1}.

Organ dose While the absorbed dose specifies the dose at one location $\boldsymbol{r}$, the absorbed dose is commonly averaged over larger tissues or organs for radiation protection purposes in the low dose regime [8]. The mean dose across one tissue or organ T is thereby calculated by

$$D_T = \frac{\int_T D(\boldsymbol{r})\rho(\boldsymbol{r})dV}{\int_T \rho(\boldsymbol{r})dV}.$$

Equivalent dose For the biological effect, also the type of radiation is relevant, that is the type of particles. This is considered by the so-called equivalent dose H_T for which the organ dose values caused by different types of radiation are weighted by a radiation weighting factor w_R:

$$H_T = \sum_R w_R D_T$$

For electrons and photons, however, the radiation weighting factor is one [8]. Hence, the numerical value of the absorbed dose D_T and the equivalent dose H_T is the same for the application in CT. However, it is convention that the unit of the equivalent dose is Sievert (Sv) where 1 Sv=1 J kg^{-1}.

Effective dose Overall measures of the radiation detriment have to consider that different organs exhibit different sensitivities towards radiation [34]. A widely used dose metric for radiation protection purposes is the effective dose D_{eff} given by

$$D_{\text{eff}} = \sum_T w_T D_T. \tag{2.10}$$

where w_T denotes the tissue weighting factors recommended and updated by the International Commission on Radiological Protection (ICRP) [8]; the sum of the tissue

Table 2.1: Tissue weighting factors as recommended by the ICRP [8].

Tissue	Tissue weighting factor w_T	$\sum w_T$
bone-marrow (red), colon, lung, stomach, breast, remainder tissues*	0.12	0.72
gonads	0.08	0.08
bladder, esophagus, liver, thyroid	0.04	0.16
bone surface, brain, salivary glands, skin	0.01	0.04
	Total	1.00

* remainder tissues (14 in total, 13 in each sex): adrenals, extrathoracic tissue, gall bladder, heart, kidneys, lymphatic nodes, muscle, oral mucosa, pancreas, prostate (♂), small intestine, spleen, thymus, uterus/cervix (♀).

weighting factors is one (compare table 2.1).

2.4.2 Radiation Risk

As introduced in section 2.1, X-ray photons can ionize atoms and molecules via Compton scatter and photoelectric effect. These ionizations can directly or indirectly damage the cell. Direct refers here to processes in which the ionizing radiation directly alters biomolecules or the DNA. In indirect processes, the radiation interacts with the cytoplasm, the cell water, or neighboring structures of the DNA which then induces chemical processes affecting the DNA and other biomolecules [35]. Fortunately, the human body is used to ionizing radiation and has sophisticated repair mechanisms; for a homogeneous body exposure of 2.4 mGy about $5 \cdot 10^{14}$ ionizations can be estimated to occur per kilogram body weight [35]; the value of 2.4 mGy corresponds approximately to the worldwide annual average effective dose of 2.4 mSv [5], [35]. However, for high dose rates that induce the death or malfunction of a larger group of cells, harmful tissue reactions occur ranging from organ damage or loss to radiation disease and death [8], [34], [36]. These effects usually have a tissue or organ and individual dependent threshold below which the effect does not occur and above which the severity increases [34], [36]. The lowest such observed thresholds are in the range from 100 mSv to 500 mSv [36]. The received doses during one CT scan usually are in the range of a few milli-Sievert below 10 mSv [1], [4] and thus are in the low-dose range of doses up to about 100 mSv [8]. For doses below 100 mSv, it is assumed that no clinically relevant tissue effects occur directly after the irradiation [8]. Nevertheless, stochastic effects leading to cancer development or heritable effects in descendants might occur [8]. These effects are called stochastic as not the severity but the probability to occur increases with dose. However, the relation between dose and the probability of stochastic effects is scientifically not clear as it is hard to quantify it in epidemiological studies for such low doses [6]. Due to the missing data, the dose-effect-relation is highly discussed [37]. Some studies even

suggest that there might be positive effects of low dose exposure [37]. For radiation protection purposes, however, it is commonly assumed that there exists no threshold dose for stochastic effects and that the probability increases linearly with dose. This assumption is called the linear-non-threshold (LNT) theory and is adopted by several international committees [8]. The ICRP, for example, estimates that the cancer risk is 5.5 % per Sievert [8]. Due to the large number of CT examinations, even such low probabilities could lead to a considerable number of cancer cases [7].

For radiological protection purposes, the ICRP furthermore recommends tissue weighting factors for the effective dose defined by equation (2.10). The most important data source for the derivation of these weighting factors stems from survivors of the atomic bombs in Japan. Furthermore, the weighting factors represent an average over age and sex [8]. The considered organs and their respective weighting factors have been updated by the ICRP since the introduction of the effective dose in 1977 [38]. Currently, weighting factors are provided for 14 organs and a remainder group of tissues consisting of further 14 tissues (compare table 2.1); for these remainder tissues, the ICRP concludes that there is evidence for radiation risk of the whole group of tissues but the risk for any individual tissue is unclear. Therefore, the ICRP concluded that all considered tissues should be assigned a small weight [8]. The use of the effective dose is intended for planning and optimization of radiation exposure as well as the retrospective assessment of dose protection and for comparing different procedures with each other. The effective dose is not intended to determine individual radiation risks.

2.4.3 Clinical Operational Quantities

There is no way to measure equivalent or effective dose in a patient directly [8]. Even if it were possible to place several dosimeters into a patient's body as it is possible for phantoms and corpses, these dosimeters would only measure point doses instead of the complete dose distribution. Therefore, radiation protection in CT is based on surrogate dose metrics or so-called operational quantities [8] from which equivalent and effective doses can be estimated.

A standard metric in CT is the so-called CT dose index (CTDI) [1]. The CTDI is measured in a cylindrical polymethyl methacrylate (PMMA) zylinder with a diameter of 16 cm for head and child scans and 32 cm for thorax and abdomen scans of adults [1]. In the phantom, dosimeters are inserted at the center and four positions at the periphery of the phantom equally spaced in angle. For the measurement, the phantom is placed perpendicular to the tomographic plane, and the dose is measured in a longitudinal range of 100 mm around the slice position. The measured dose is divided by the collimation C of the scanner. This procedure defines the so-called CTDI_{100} value [1]:

$$\mathrm{CTDI}_{100} = \frac{1}{C} \int_{-50\,\mathrm{mm}}^{+50\,\mathrm{mm}} dz D(z).$$

To account for the dose differences across the phantom, the dose values measured in

the center and the peripheral positions are weighted in the following way:

$$\mathrm{CTDI_w} = \frac{1}{3}\mathrm{CTDI}_{100}^{\mathrm{central}} + \frac{2}{3}\mathrm{CTDI}_{100}^{\mathrm{peripheral}}.$$

This formula for the so-called weighted CT dose index (CTDI)-value can be derived as the average dose absorbed in the phantom under the assumptions that the dose rises linearly with the radius and is independent of the angular position [39].

For spiral scans, the weighted CTDI-value is weighted by the pitch value [1]:

$$\mathrm{CTDI_{vol}} = \frac{\mathrm{CTDI_w}}{p}.$$

CTDI-values are usually stored in the scanner in mGy/100 mA s for different voltages and prefilter settings. Thus, the CTDI-value of a scan can be calculated by multiplying the tabulated value for the respective setting by the employed tube current time product, i.e. the integral of the tube current over the scan time.

To estimate the effective dose from the CTDI-value, the dose-length-product (DLP) is calculated in a first step which considers the length L of the scan:

$$\mathrm{DLP} = \mathrm{CTDI_{vol}} \cdot L.$$

Using Monte Carlo simulations, so-called k-factors have been determined to convert from the DLP to an estimate of the effective dose:

$$D_{\mathrm{eff}} \approx k \cdot \mathrm{DLP}.$$

These k-factors are given for different body regions and different ages and are published for example by the European Commission and the National Radiological Protection Board [1]. However, the factors are not patient-specific but can be interpreted as the dose of an average patient [1].

2.5 Exposure Control

To keep the radiation exposure for the patient as low as reasonably achievable (ALARA) [9], the applied radiation should be tailored to the patient to achieve the desired image quality at minimum risk. This adjustment includes the tube current which controls the number of photons emitted by the X-ray tube and the tube voltage which affects the photons' energy distribution. Furthermore, prefilters in front of the X-ray tube can be used to attenuate low-energy photons. The role and control of these three parameters are discussed in the following subsections.

2.5.1 Tube Current

The tube current controls the number of photons emitted by the X-ray tube. The number of photons is proportional to the tube current and determines the noise in the

projection data measured at the detector. The noise on the projection values in turn is almost linearly propagated to the image noise by the reconstruction [1].

For a monochromatic X-ray, the number of detected photons N described by the Beer-Lambert law and by the detection efficiency of the detector follows a Poisson distribution [1]. This relation implies that the variance of N is equal to its expectation value: $\sigma_N^2 = N$. By defining the projection value as $p = -\ln(N/N_0)$, it follows by error propagation and omission of any uncertainty on N_0, that the projection variance σ_p^2 is inverse to N and thus also to N_0 and the tube current I:

$$\sigma_p^2 \propto \frac{1}{N} \propto \frac{1}{N_0} \propto \frac{1}{I}.$$

Hence, the selection of the tube current value is a trade-off between image noise and patient dose; for a higher tube current, the image noise decreases but the patient dose increases.

Constant Tube Current

Initially, CT scanners were operated with a constant tube current, that is, for every projection, the same tube current was applied. For a constant tube current, the lowest constant value to achieve the requested image noise should be selected to decrease patient dose. However, patient attenuation can highly vary between different view angles which leads to high differences in photon statistics at the detector and streak artifacts in the image. This effect is especially pronounced in the shoulder and pelvis region with high differences in attenuation between lateral and and anterior-posterior views. Furthermore, the dose received by radiation-sensitive organs at the periphery of the body is higher for tube positions anterior to these organs than for tube positions posterior to them. For both reasons, i.e. the variation in attenuation and the dependence of organ doses on the tube position, a sophisticated allocation of tube current can reduce patient dose at constant image quality. This concept to distribute the tube current is called tube current modulation (TCM).

Conventional mAs-Minimizing TCM

Initial work on TCM aimed at minimizing the mAs-product of the scan while keeping the image noise constant [10], [11]. The mAs-product of the scan refers here to the integral of the tube current over the scan time. Nowadays, all modern scanners are equipped with a TCM based on this concept which can therefore be considered conventional. Due to the minimization of the mAs-product, it is referred to as mAsTCM in the following.

The basic relation of the tube current for mAsTCM can be derived within a few mathematical steps [10]. The noise variance of the central pixel of the reconstructed image σ_C^2, can be calculated by the sum of the projection variances for the central ray $\sigma_p^2(\alpha)$ over all views α. For the monochromatic approximation, the projection variance $\sigma_p^2(\alpha)$ is given by $\sigma_p(\alpha)^2 = N(\alpha) = e^{p(\alpha)}/N_0(\alpha)$ with $p(\alpha)$ denoting the projection value and $N_0(\alpha)$ the number of emitted photons. The noise variance of the central pixel can

hence be calculated by

$$\sigma_{\mathrm{C}}^2 = \sum_{\alpha} \sigma_p(\alpha)^2 = \sum_{\alpha} \frac{e^{p(\alpha)}}{N_0(\alpha)}. \tag{2.11}$$

Minimizing σ_{C}^2 under the condition that the mAs-product stays constant, i.e. the sum over all emitted photons $\sum_\alpha N_0(\alpha)$ stays constant, yields the following results:

$$N_0(\alpha) \propto I(\alpha) \propto \sqrt{e^{p(\alpha)}}.$$

Hence, to minimize the noise of the central pixel at constant mAs-product, the tube current for every view $I(\alpha)$ should be chosen proportional to the square root of the attenuation for the central ray of this view. This implies that the knowledge of the attenuation for every view is required to perform this modulation on a scanner. Usually, this information is approximated from topograms taken before the scan but older systems offered by Philips and Siemens also used data acquired during the scan from the last semicircle [40]. An overview of different TCM implementations and their respective names by different vendors is given in reference [40].

Organ-Specific TCM

As different organs are more sensitive to radiation than others, it can be beneficial to lower the radiation received by organs with a high sensitivity to radiation. Therefore, different vendors have equipped their scanners with organ-specific TCM (osTCM) [12]–[14]. These include for example osTCM for the breast, the thyroid, or the eyes. In front of the organ in question, the tube current is lowered. In contrast to the conventional TCM, the modulation is not adapted to the patient, but the tube current is typically lowered in a predefined angular interval.

Risk-minimizing TCM

While mAsTCM reduces the amount of emitted photons and organ-specific TCM reduces the dose to particularly sensitive organs, none of these methods minimizes the radiation risk directly. Already a few decades ago, it was suggested to minimize the effective dose [41] and computer simulations have shown the potential to decrease the effective dose at constant image quality [15], [16]. In reference [15], this TCM was named risk–minimizing tube current modulation (riskTCM), and the decrease in effective dose was demonstrated in simulations for different patients and body regions from head to pelvis. However, to minimize the effective dose, the effective dose has to be estimated before the scan. In the proposed approaches, this effective dose estimation includes a prior estimation of the dose distribution and an organ segmentation from which organ doses and the effective dose are calculated [15], [16]. For the optimization, the image noise is estimated by error propagation, and the effective dose is minimized at a constant noise level.

2.5.2 Tube Voltage Selection

The tube voltage affects the photons' energy distribution. Higher voltages shift the photons' energies to higher energies and increase the maximum photon energy (compare figure 2.3). A higher photon energy leads at constant tube current to less projection noise but also usually to a higher deposited dose for the patient sizes and voltages in clinical CT. For some energy, the trade-off between noise and dose is optimal; this energy depends on the object's attenuation. In general, the optimal energy and thus also the optimal voltage increases with patient diameter. As for the conventional mAsTCM, the patient's diameter can be approximately derived from the topogram. One way to then choose the optimal voltage is by using a library with phantom measurements of different sizes [42].

In the case of iodine-enhanced scans, the contrast-to-noise ratio (CNR) might be the more appropriate quantity to optimize. Iodine contrast is higher at low voltages due to the k-edge of iodine at 33 keV (compare figure 2.1). Therefore, the optimal voltage is lower for contrast-enhanced scans but still increases with patient size.

Furthermore, especially if the optimal voltage is low, tube current limits can apply if the patient is not sufficiently thin for the desired image quality. Then, higher tube voltages have to be selected for which less tube current is necessary due to better photon statistics and the higher photon output at the same tube current value. The procedure of automatic tube voltage selection (ATVS) is therefore as follows [43]: from the topogram and the desired image quality parameter, the necessary tube current for every voltage is determined. Low tube voltages for which the tube current exceeds the tube current limit are excluded from the selection. From the remaining tube voltages, the one resulting in the lowest CTDI value is selected. In contrast to the tube current which is usually modulated, the voltage remains constant throughout the scan.

2.5.3 Prefilters

Prefilters harden the spectrum by attenuating low-energy photons more than photons with higher energy. This mechanism is used to absorb low-energy photons with a low probability of passing the patient and reaching the detector. Furthermore, a harder spectrum might be more dose-efficient depending on the patient size. However, with increasing prefilter thickness, also the necessary tube power increases as the prefilter attenuates the whole spectrum. Therefore, the available prefilters are a compromise between thickness and the available tube power [1]. Currently, only two vendors use removable prefilters in their systems, namely Siemens with tin filters up to 0.7 mm and Canon with a silver filter of undisclosed thickness [3]. Furthermore, GE uses a copper prefilter in one system for the acquisition of the topogram [3].

3 Tube Current and Tube Voltage Modulation

This chapter presents the study on a novel risk-minimizing tube current and tube voltage modulation (riskTCTVM). As introduced in chapter 2, modern clinical scanners employ automatic exposure control techniques including tube current modulation (TCM) and the selection of a constant voltage. This chapter gives a deeper introduction on the selection of the optimal voltage and previous research on tube voltage modulation in section 3.1. Section 3.2 describes the materials and methods used for this study and section 3.3 presents the results. A discussion of the proposed risk-minimizing tube current and tube voltage modulation is given in chapter 5.

3.1 Introduction

The tube voltage affects the photons' energy distribution. With increasing tube voltage, the maximum photon energy increases and the energy distribution is shifted towards higher energies. Moreover, the attenuation of the photons depends on the traversed material and the photons' energies. As CT measures the attenuation of X-rays, there exists an optimal X-ray energy that depends on the optimization criteria. For small homogeneous cylinders with diameter D and linear attenuation coefficient μ, one finds that the energy E_{opt} which fulfills $\mu(E_{\text{opt}}) = 2/D$ minimizes the number of photons required to achieve a given signal-to-noise ratio [44]. This results in an optimum energy of about 1 MeV for a water cylinder with diameter $D = 30\,\text{cm}$ [44]. This energy drops to 70 keV if the absorbed dose at the center of the phantom is considered instead of the number of incident photons [41]. However, while monochromatic X-ray sources such as synchrotron radiation exist [45], conventional CT scanners contain X-ray tubes that emit a spectrum of X-ray energies. Therefore, later studies focused primarily on the optimal choice of tube voltage.

In one study, the optimal voltage was defined as the one that maximizes the dose-weighted contrast-to-noise ratio (CNRD) and was determined for a range of cylindrical water phantoms and quasianthropomorphic phantoms of the thorax and abdomen [46]. The considered contrasts were calcium, iodine, and an energy-independent soft tissue contrast. The dose in the phantoms was defined as a weighting of peripheral and central dose analogously to CTDI_w, a commonly used dose measure which is based

on measurements in acrylic cylinders (compare subsection 2.4.3). Simulations were performed for voltages from 40 kV to 140 kV and measurements for voltages from 60 kV and 140 kV. The authors found that the common settings of 120 kV to 140 kV are suited for soft tissue imaging and that voltages below 80 kV are advantageous for calcium (bone) and iodine imaging.

A further study described a workflow for choosing the optimal voltage [42]. This workflow requires a database generated by preceding phantom measurements or an equivalent mathematical model that can generate the same values. For an image quality parameter, iodine contrast-to-noise ratio (CNR) with a noise constraint was proposed. The authors argue that in some iodine-enhanced exams, there are structures relevant for the diagnosis with a small enhancement that do not benefit from the higher contrast at lower tube voltages. The noise constraint is a parameter in the optimization that reflects how much increase in noise can be tolerated.

Nowadays, modern clinical scanners are equipped with automatic tube voltage selection (ATVS). These ATVS systems retrieve attenuation information from topograms and then select the voltage that results in the lowest dose that stays within the tube current limit for a certain image quality level for a specific imaging task (e.g. soft tissue with or without contrast, CT angiography, etc.) [43].

In conclusion, it is recognized that the optimal voltage depends on patient attenuation and the imaging task. However, patient attenuation varies within one scan; while TCM accounts for these changes to use the X-rays more efficiently, current ATVS systems choose a constant voltage resulting in a compromise between different projection angles. After the introduction of TCM, it was imagined that tube voltage modulation (TVM) could be developed similarly to TCM [47] and there are a few proposals of TVM in literature.

Some TVM techniques were proposed for material testing applications [48]–[50] where the differences in attenuation for different projection angles can be enormous. Also, for cone-beam C-arm systems, a tube voltage modulation can be beneficial [51]–[53]. In the field of clinical CT, a variation of the tube voltage throughout the scan was also proposed to perform material decomposition with a conventional single-energy CT system [54]–[56]. For photon-counting CT systems, TVM has also been studied to reduce noise in material decomposition tasks [57].

Regarding a dose reduction in clinical CT, one study investigated the potential reduction in breast dose by using different voltages for anterior and posterior views [58]. However, this study lacked an investigation of the image quality, and therefore the potential reduction in breast dose at constant image quality for this strategy remains unknown. In this chapter, the potential of reducing the effective dose by a tube voltage modulation in addition to TCM for unenhanced scans at constant noise and for iodine-enhanced scans at constant CNR is studied for different patients, anatomical regions, and different voltage ranges. The study builds upon previous work presented in references [59] and [60].

3.2 Materials and Methods

3.2.1 General Concept

For the optimization of the risk–minimizing tube current and tube voltage modulation (riskTCTVM), circular scans with a tube current value $I(\alpha)$ and a tube voltage value $U(\alpha)$ for every projection angle α were considered. For a given modulation, the effective dose for these parameter settings is calculated using a patient and slice-specific look-up table. Furthermore, the noise inside the patient's body and the contrast of a simulated iodine disk inserted in the center of the considered slice are estimated. Consecutively, the resulting CNRD is calculated. To maximize the CNRD, the tube current and tube voltage curves are optimized using the L-BFGS-B algorithm [61], [62]. For scans without contrast material or for TCMs at constant voltage, the dose-weighted noise, i.e. the denominator of the CNRD is minimized.

The following sections are organized as follows: Section 3.2.2 describes the used patient models, section 3.2.3 the determination of the effective dose per scan using Monte Carlo dose simulations, section 3.2.4 the noise estimation and section 3.2.5 the contrast estimation. The optimization, baseline TCMs, and the calculation of relative effective doses at constant noise or constant CNR are described in section 3.2.6.

3.2.2 Patient Models

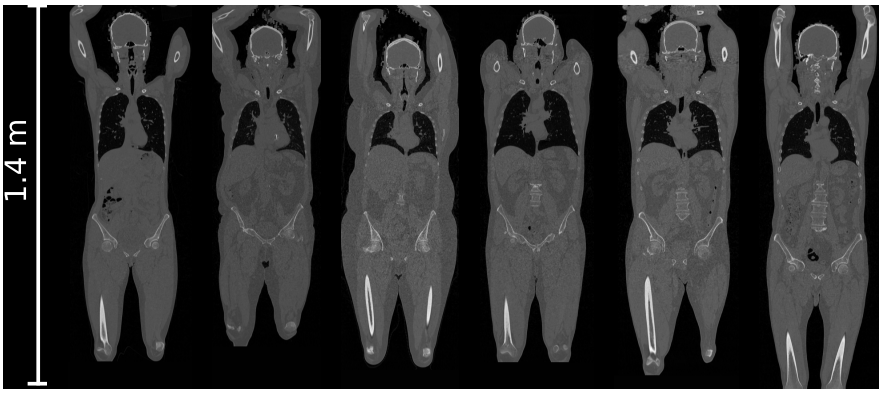

Figure 3.1: Coronal views of the considered three female (left) and three male (right) patients from the Visceral dataset [63].

The patient models are based on CT datasets of three female and three male patients from the Visual Concept Extraction Challenge in Radiology (Visceral) [63] (see figure 3.1). The CT scans were acquired unenhanced and have a field of view from the head to the knee of the patients [63]. Organ segmentations that were created for the study of a risk-minimizing tube current modulation (riskTCM) as described in reference [15] were used for the calculation of organ doses.

3.2.3 Dose Model

Per-View Dose Simulations

For the dose simulations, every voxel of the patients' CT volume was assigned to one of five materials (air, lung tissue, fat, water, bone) using a threshold-based segmentation, and the corresponding density was calculated from the CT value. With our in-house Monte Carlo dose simulation software, dose distributions for tube positions

$$\boldsymbol{s}(\alpha, z) = \begin{pmatrix} R_\mathrm{F} \sin\alpha \\ -R_\mathrm{F} \cos\alpha \\ z \end{pmatrix} \quad \text{with } R_\mathrm{F} = 595\,\mathrm{mm}$$

on a circular trajectory were created, i.e. at a fixed longitudinal table position z and projection angles α covering 360° with an angular increment of 10°. Simulations were performed for longitudinal positions z from the shoulder to the pelvis of the patients with an increment of about 38 mm. In the following, the dependency on z is dropped for better readability. The scanner geometry of a Somatom Definition Flash scanner with a collimation of 38.4 mm, a source-to-isocenter distance of $R_\mathrm{F} = 595$ mm, a source-to-detector distance of 1085.6 mm, and a field of measurement of 500 mm was considered. Furthermore, the photons were attenuated by a bowtie filter. Dose distributions for photon energy intervals of 5 keV from 20 keV to 150 keV were simulated. To calculate the per-view effective dose for arbitrary tube voltages, Tucker spectra [26] with 6 mm aluminum prefiltration were used. The dose values for the different simulated photon energies were then weighted according to these Tucker spectra.

Calculation of per-View Effective Dose

From the per-view dose distributions $D(\alpha, \boldsymbol{r})$, organ doses $D_T(\alpha)$ were obtained by calculating the mean organ dose, i.e. the total deposited energy in that organ divided by the organ mass, which is given by the integral of the density $\rho(\boldsymbol{r})$ over the organ volume:

$$D_T(\alpha) = \frac{\int_T D(\alpha, \boldsymbol{r})\rho(\boldsymbol{r})dV}{\int_T \rho(\boldsymbol{r})dV}.$$

Building a weighted sum of these organ doses with organ weighting factors w_T, per-view effective doses were calculated by

$$D_\mathrm{eff}(\alpha) = \sum_T w_T D_T(\alpha).$$

All 14 organs with a weighting factor w_T equal to or greater than 0.01 in the recommendations of the International Commission on Radiological Protection (ICRP) [8] were considered (compare table in figure 3.2). All other tissues were treated as one single organ and assigned the weighting factor for the remainder tissues.

Finally, the obtained per-view effective dose values $D_{\text{eff}}(\alpha)$ for the photon energy intervals were weighted according to their intensity in the generated Tucker spectra to obtain per-view effective doses $D_{\text{eff}}(\alpha, U)$ for different voltages U. The created Tucker spectra model the photon output per electron considering that different voltages result in different numbers of photons per electron.

Tissue	Tissue weighting factor w_T	$\sum w_T$
bone-marrow (red), colon, lung, stomach, breast, remainder tissues	0.12	0.72
gonads	0.08	0.08
bladder, esophagus, liver, thyroid	0.04	0.16
bone surface, brain, salivary glands, skin	0.01	0.04
	Total	1.00

Figure 3.2: Tissue weighting factors as recommended by the ICRP [8] and color scheme used in this study to label the different organs.

Calculation of Effective Dose per Scan

To obtain the overall effective dose for a circular scan, the sum over the per-view effective doses multiplied by the respective tube current $I(\alpha)$ was calculated:

$$D_{\text{eff}}(I, U) = \sum_{\alpha} I(\alpha) \cdot D_{\text{eff}}(\alpha, U(\alpha)).$$

3.2.4 Noise Estimation

To estimate the image noise, we need to propagate the expected noise in the rawdata domain to the image domain. For every intersection through the patient, a water-equivalent pathlength l_{W} for water of density $\rho_{\text{W}} = 1\,\text{g}\,\text{cm}^{-3}$ with mass attenuation coefficient $\psi_{\text{W}}(E)$ and an intersection through iodine with density $\rho_{\text{I}} = 4.93\,\text{mg}\,\text{cm}^{-3}$ with mass attenuation $\psi_{\text{I}}(E)$ was considered. This leads to a polychromatic attenuation value q for the projection angle α and the angle β within the fan of

$$q(\alpha, \beta) = -\ln \int dE\, w(E, U, \beta) e^{-l_{\text{W}}(\alpha,\beta)\psi_{\text{W}}(E) - l_{\text{I}}(\alpha,\beta)\psi_{\text{I}}(E)}. \tag{3.1}$$

Here, E denotes the photon energy and $w(E, U, \beta)$ the normalized detected spectrum. The detected spectrum $n_0(E, U, \beta)$ was modeled as follows:

$$n_0(E, U, \beta) = \underbrace{n_\mathrm{T}(E, U)}_{\text{Tucker spectrum}} \cdot \underbrace{e^{-\mu_\mathrm{B}(E) \cdot d_\mathrm{B}(\beta)}}_{\text{Bowtie}} \cdot \underbrace{E \cdot (1 - e^{-\mu_\mathrm{D}(E) d_\mathrm{D}})}_{\text{Detector}}.$$

The first term $n_\mathrm{T}(E, U)$ denotes the voltage-dependent Tucker spectrum [26] with 6 mm aluminium prefiltration. The second term models the attenuation by the bowtie filter, and the third term the detection of an energy-integrating detector for which a $d_\mathrm{D} = 1.4\,\mathrm{mm}$ thick gadolinium oxysulfide scintillator layer with a density of $7.32\,\mathrm{g\,cm^{-3}}$ was considered. The integral of the detected spectrum over the energy is denoted here with $N_0(U, \beta)$, i.e. $N_0(U, \beta) = \int dE n_0(E, U, \beta)$. Consecutively, the normalized detected spectrum is given by $w(E, U, \beta) = n_0(E, U, \beta)/N_0(U, \beta)$.

The water-equivalent intersection lengths were obtained by forward projection of the density of the patient CT volume and dividing by $\rho_\mathrm{W} = 1\,\mathrm{g\,cm^{-3}}$. As in reference [15], the forward projection was performed for different detector rows and an average over the detector width was performed by

$$l_\mathrm{W}(\alpha, \beta) = \frac{1}{B} \int_{-B/2}^{+B/2} db\; l_\mathrm{W}(\alpha, \beta, b)$$

where B denotes the width of the detector in the isocenter, i.e. the collimation.

The detected signal S at the detector is described by $S = I \cdot N_0 \cdot e^{-q}$. Following the derivation of image noise in reference [15], this signal S was assumed to be Poisson-distributed, i.e. $\mathrm{Var}\, S = S$. By error propagation and assuming no uncertainty on I and N_0, this yields a variance of the polychromatic attenuation of

$$\mathrm{Var}\; q = \frac{e^q}{I \cdot N_0} \quad \text{for} \quad q = \ln(S) - \ln(I \cdot N_0).$$

Note that the norm of the detected spectrum was omitted in the variance calculation in references [59] and [60] but should be considered due to the dependence of N_0 on the voltage.

For image reconstruction, the measured polychromatic attenuation values are water-precorrected. Water precorrection relates the polychromatic attenuation values to single intersection lengths with water p:

$$q = Q(p) = -\ln \int dE\, w(E, U, \beta) e^{-p \psi_\mathrm{W}(E)}. \tag{3.2}$$

Equation (3.2) is a bijective relation between p and q and $p = P(q, w)$ denotes the water precorrection function. The water precorrection $p = P(q, w)$ was performed using tabulated values that were created for every spectrum $w := w(E, U, \beta)$, i.e. for every voltage U and every angle β within the fan.

Propagating the noise of q to p yields

$$\text{Var } p \propto \frac{e(p,w)}{I \cdot N_0} \text{ with } e(p,w) = (P'(Q(p),w))^2 e^{Q(p)}. \tag{3.3}$$

This relation was similarly derived in reference [15]. Following reference [15], it was assumed that complementary rays are weighted in a statistically optimal way, i.e. inversely to their variance. Thus, the variance of the projection value for two complementary rays at source positions α_C and α_D is given by

$$\begin{aligned} V_\mathrm{opt} &= \frac{1}{1/V_\mathrm{D} + 1/V_\mathrm{C}} \\ &= \left(\frac{I_\mathrm{D} \cdot N_0(U_\mathrm{D}, +\beta)}{e(p(\alpha_\mathrm{D}, +\beta), w(U_\mathrm{D}, +\beta))} + \frac{I_\mathrm{C} \cdot N_0(U_\mathrm{C}, -\beta)}{e(p(\alpha_\mathrm{C}, -\beta), w(U_\mathrm{C}, -\beta))} \right)^{-1}. \end{aligned}$$

The statistically optimal weighting of complementary rays allows the optimization to turn off the tube current for projection angles with a high effective dose.

For the optimization, the image noise throughout the whole patient's body was considered. Similar to reference [15], the overall noise was computed as the weighted sum of noise values for different positions across the patient's body:

$$N(I,U) = \int dxdy\, w(\boldsymbol{r}) \sqrt{\int d\vartheta \left(\frac{I_\mathrm{D} \cdot N_0(U_\mathrm{D}, +\beta)}{e(p(\alpha_\mathrm{D}, +\beta), w(U_\mathrm{D}, +\beta))} + \frac{I_\mathrm{C} \cdot N_0(U_\mathrm{C}, -\beta)}{e(p(\alpha_\mathrm{C}, -\beta), w(U_\mathrm{C}, -\beta))} \right)^{-1}}. \tag{3.4}$$

Here, $w(\boldsymbol{r})$ denotes the weight given to the noise at different locations $\boldsymbol{r}$ in the image. In this study, this weight was set to one inside the patient and zero outside. However, $w(\boldsymbol{r})$ could also be used to enhance the image quality for specific anatomical regions for a specific diagnostic task. The angle ϑ denotes here the angle of a ray going through the point $\boldsymbol{r} = (x, y)$ in parallel beam geometry. The distance of that ray to the isocenter is then given by $\xi = x\cos\vartheta + y\sin\vartheta$. The corresponding tube angle α and the angle β within the fan can be retrieved using the equations $\vartheta = \alpha + \beta$ and $\xi = -R_\mathrm{F}\sin\beta$.

3.2.5 Contrast Estimation

To investigate the benefit of a tube voltage modulation for contrast-enhanced scans, an iodine disk of 2 cm diameter and density $\rho_\mathrm{I} = 4.93\,\mathrm{mg\,cm^{-3}}$, i.e. iodine diluted by a factor of 1000, was artificially inserted into the CT images in the isocenter.

The water precorrection assumes that the whole patient consists of water. Hence, the contrast in the reconstructed image corresponds to the density that water would require to exhibit the same attenuation as the contrast material. We can therefore add the following third expression of the polychromatic attenuation value q to equations

(3.1) and (3.2):

$$\begin{aligned} q &= -\ln\int dE\, w(E,U,\beta) e^{-l_\mathrm{W}\psi_\mathrm{W}(E) - l_\mathrm{I}\psi_\mathrm{I}(E)} \\ &= -\ln\int dE\, w(E,U,\beta) e^{-p\psi_\mathrm{W}(E)} \\ &= -\ln\int dE\, w(E,U,\beta) e^{-(l_\mathrm{W} + l_\mathrm{I}C_\mathrm{I})\psi_\mathrm{W}(E)}. \end{aligned}$$

We can hence calculate the contrast by solving the equation

$$p = l_\mathrm{W} + l_\mathrm{I}C_\mathrm{I}$$

which gives us

$$C_\mathrm{I} = \frac{p - l_\mathrm{W}}{l_\mathrm{I}}. \tag{3.5}$$

The contrast in the isocenter is then given by the sum of the contrast values C_I (defined by equation (3.5)) for the central rays where complementary rays are weighted by their variance.

3.2.6 Optimization

Unenhanced Scans

For unenhanced scans, the dose-weighted noise was minimized which was defined as follows:

$$N_D = \sqrt{D/D_\mathrm{ref}} \cdot N \quad \text{with} \quad D \coloneqq D_\mathrm{eff}. \tag{3.6}$$

This definition is invariant against scalings of the tube current as the dose is proportional to the current and the noise antiproportional to the square root of the current. Thus, regarding the tube current, only the relative course is relevant for the optimization. For the tube voltage, a voltage range of 70 kV to 150 kV was considered. After the optimization, the tube current can be scaled to achieve a certain noise. Solving equation (3.6) for the dose, the dose for any desired noise is given by

$$D = \left(\frac{N_D}{N}\right)^2 \cdot D_\mathrm{ref}$$

and we can therefore calculate the relative dose to a reference modulation with $N_{D,\mathrm{ref}}$ by

$$\text{Relative dose} = \frac{N_D^2}{N_{D,\mathrm{ref}}^2}.$$

The dose reduction compared to the reference modulation was defined as

$$\text{Dose reduction} = 1 - \text{Relative dose}.$$

Iodine-Enhanced Scans

For iodine-enhanced scans, the CNRD defined by

$$\text{CNRD} = \frac{C}{\sqrt{D/D_{\text{ref}}} \cdot N} \tag{3.7}$$

was maximized. Again, this definition is invariant to scalings of the tube current. For the tube voltage, an upper bound of 150 kV was set. For the lowest allowed voltage, four different scenarios were considered, namely 40 kV, 50 kV, 60 kV, and 70 kV. The optimization of the CNRD was formulated as a minimization of the negative CNRD.

The relative dose at constant CNR is given for enhanced scans by

$$\text{Relative dose} = \frac{\text{CNRD}_{\text{ref}}^2}{\text{CNRD}^2}.$$

Discretization

The tube current and the tube voltage were optimized for tube angles α with a spacing of 1°. For the calculation of noise and contrast, sinograms with an angular spacing of 1° for the tube angle α and 0.05° for the angle β within the fan were created. To obtain effective dose values at a pitch of 1°, the simulated effective dose values were interpolated. For the calculation of the overall noise (compare equation (3.4)), the noise at points (x, y) were evaluated on a grid with a spacing of approximately 7 mm. The integral over the angle ϑ (compare equation (3.4)) was performed in steps of 0.5°.

Optimization Algorithm

For the optimization, the implementation of the L-BFGS-B [61], [62] algorithm provided within the optimization framework of SciPy [64] was used. The L-BFGS-B algorithm builds upon the Broyden–Fletcher–Goldfarb–Shanno (BFGS) algorithm and allows for bounds on the input variables and operates with limited memory [61]. Furthermore, the L-BFGS-B algorithm is a quasi-Newton method that uses an approximate of the Hessian matrix [61]. Therefore, besides the objective function values, i.e. the dose-weighted noise or the CNRD, only the gradients with respect to every tube current and every tube voltage value were computed.

Baseline Tube Current Modulations

Two TCM methods as a baseline to riskTCTVM, namely riskTCM and mAsTCM were considered. For riskTCM, the dose-weighted noise as defined by equation (3.6) was minimized. This optimization was performed for voltages between 40 kV and 150 kV in

steps of 5 kV. For mAsTCM, the tube current values were calculated analytically for the same voltages as described in the following. For minimizing the image noise in the center at constant mAs-product, the optimal tube current is proportional to the square root of the attenuation [10]. Considering polychromatic attenuation undergoing a water precorrection, the following expression for the optimal tube current in the central ray approximation was derived in reference [15]:

$$I_{\mathrm{mAsTCM}}(\alpha) \propto \sqrt{e(p(\alpha), w)}$$

with the definition of $e(p)$ as defined by equation (3.3). As in reference [15], the 90th percentile of $p(\alpha, \beta)$ was used as a surrogate for $p(\alpha)$, and the detected spectrum w for the central ray with $\beta = 0$ was used.

3.3 Results

3.3.1 Dose-Weighted Noise Minimization

Figure 3.3 shows an example of the dose-weighted noise minimization for a slice in the pelvis. mAsTCM considers only the attenuation of the patient and increases the tube current for lateral views which have a higher attenuation than anterior-posterior views due to the eccentric body shape. riskTCM instead considers also the high effective dose for views from the right and anterior to the patient due to the colon; therefore, riskTCM turns the tube current off for these positions and increases the tube current on the left side of the patient. For mAsTCM and riskTCM, the optimal voltage is 150 kV; this means that the noise per effective dose is lowest for 150 kV. The effective dose per unit tube current, however, is highest for 150 kV (compare figure 3.3). The different tube current distribution of riskTCM results in a decrease in the effective dose of approximately 34 % compared to mAsTCM. riskTCTVM also selects 150 kV for the full rotation resulting in the same tube current curve and the same effective dose as riskTCM. For all patients and anatomical regions that were studied, at most slight deviations in the tube voltage to voltages below 150 kV occurred; however, also in the cases with slight deviations in the voltage, the decrease in effective dose compared to riskTCM was well below 1 %.

3.3.2 CNRD Optimization

i.) Example Modulations

Figure 3.4 shows the CNRD optimization for the same slice as in figure 3.3. The effective dose values are given for a constant CNR and relative to riskTCM for the voltage with the highest CNRD. For the CNRD optimization, lower voltages are beneficial compared to pure noise optimization as lower voltages increase the iodine contrast. Here, the effective dose benefit of riskTCTVM compared to riskTCM highly depends on the allowed voltage range in the optimization. For a lowest allowed voltage of $U_{\mathrm{low}} = 70\,\mathrm{kV}$,

riskTCTVM decreases the effective dose at constant CNR about 10 % compared to riskTCM at constant 70 kV. For a lowest allowed voltage of 60 kV, this effective dose benefit increases to 20 % compared to riskTCM at 60 kV which is the optimal voltage for riskTCM; a decrease of the lowest voltage to 50 kV thus does not offer a further decrease in effective dose for riskTCM. riskTCTVM instead lowers the voltage for some angular range to 50 kV which increases the effective dose benefit to 26 % compared to riskTCM at 60 kV. For a lowest voltage of 40 kV, there were no or only slight further reductions in effective dose of up to 3 % for all anatomies that were studied.

Figure 3.5 shows the CNRD optimization for a slice in the shoulder for which the highest reduction in effective dose by riskTCTVM compared to riskTCM was found. For this anatomy, riskTCTVM decreases the effective dose by about 35 % compared to riskTCM for a lowest allowed voltage of $U_{\text{low}} = 50\,\text{kV}$. For $U_{\text{low}} = 70\,\text{kV}$, the decrease in effective dose is 20 %. Remarkable for this voltage range is also the decrease in the maximum requested tube current. Although riskTCTVM irradiates the patient from a smaller angular range than mAsTCM, the maximum tube current is lower due to the partial increase of the tube voltage to 150 kV.

Figures 3.6 and 3.7 show example slices in the thorax and abdomen for which the maximum decreases in effective dose by riskTCTVM compared to riskTCM for a lowest allowed voltage of 50 kV are 9 % and 12 % and thus lower than for the examples in the pelvis and the shoulder. Furthermore, figure 3.8 shows a slice in the abdomen for which riskTCTVM shows no decrease in effective dose for a lowest voltage of 70 kV and a decrease in effective dose of only 3 % for a lowest allowed voltage of 50 kV.

ii.) Relative Effective Dose

Figure 3.9 shows the effective dose values of riskTCTVM relative to the effective dose of riskTCM for a lowest allowed voltage of 50 kV for all slices of all patients that were studied. The x-axis shows the ratio of the maximum to the minimum value of the maximum water intersection length l_{W} per projection angle. As especially visible in figures 3.4 and 3.5, riskTCTVM tends to increase the tube voltage for projection angles with high attenuation and thus high water intersection lengths for which mAsTCM increases the tube current. As figure 3.9 reveals, the effective dose benefit of riskTCTVM compared to riskTCM correlates with the ratio of the maximum to the minimum value of the maximum water intersection length l_{W} per projection angle; this correlation explains in part the differences between the mean values for the different body regions (compare table 3.1). For example, the effective dose benefits for the shoulder and the pelvis are on average higher than for the thorax and the abdomen which are less eccentric body regions and thus exhibit lower ratios of the maximum to the minimum value of the maximum water intersection per projection angle. The highest average decrease in effective dose of riskTCTVM compared to riskTCM was observed for the shoulder; here, the average effective dose decrease is 13 % for a lowest allowed voltage of 70 kV and 28 % for a lowest voltage of 50 kV with values ranging from 19 % to 35 %. For one patient, a decrease in effective dose of 35 % was also found for one slice in the pelvis but the average decrease in effective dose for the pelvis is 16 % and thus lower than for

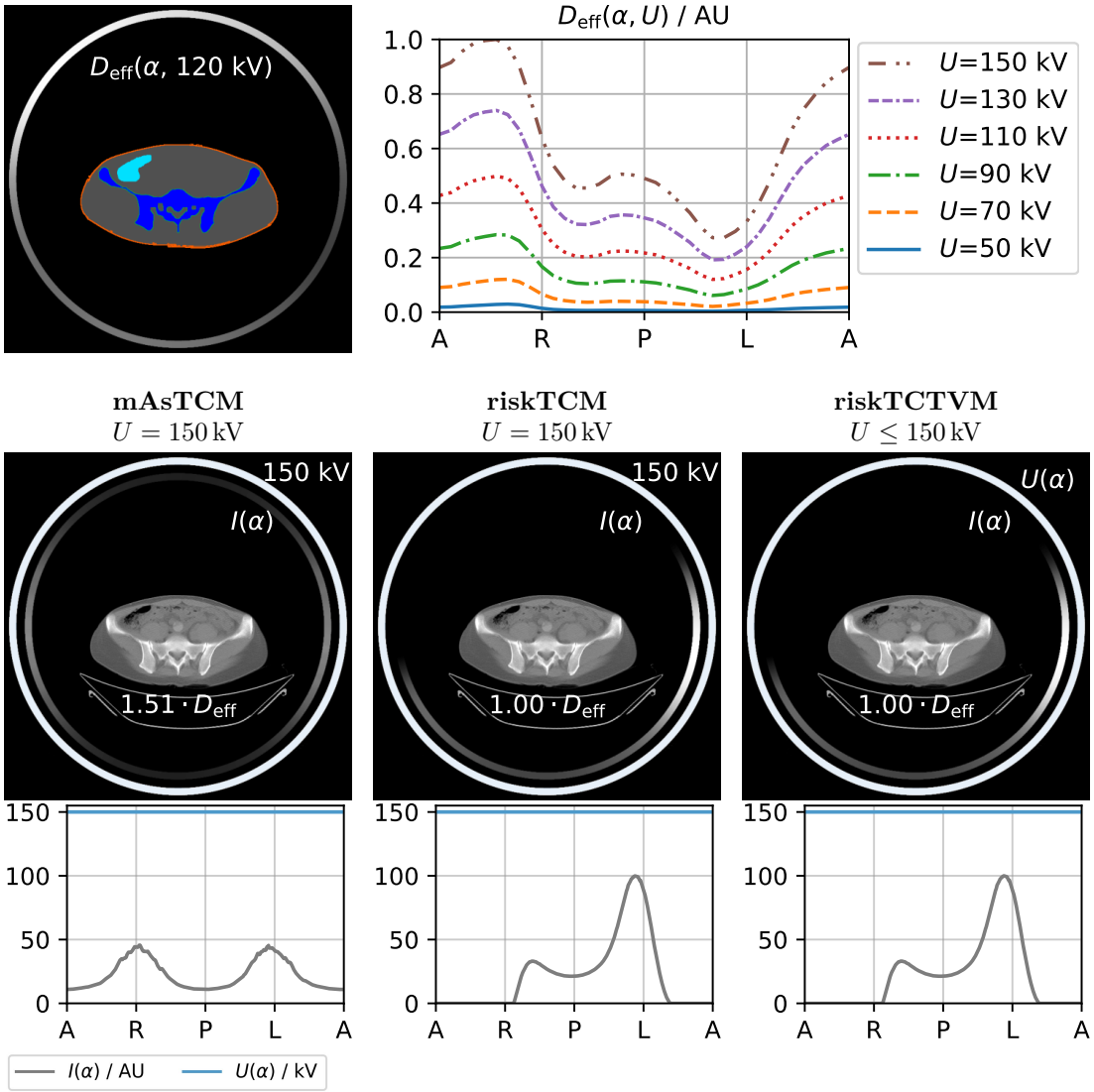

Figure 3.3: Dose-weighted noise optimization for a slice in the pelvis of a female patient. The top row shows the organ segmentation and per-view effective dose as a function of tube angle α and tube voltage U. The labeling of the x-axis corresponds to the tube positions anterior (A), right (R), posterior (P), left (L), and anterior (A) from the patient's perspective. Below, the resulting modulations for mAsTCM, riskTCM, and riskTCTVM are shown. The effective dose values are given for a constant noise level and relative to riskTCM at the best voltage for this anatomy which is $U = 150\,\text{kV}$.

the shoulder which can be explained in part by the wider spread of the eccentricity of the body shape in the pelvis compared to the shoulder.

Table 3.1: Effective dose values of the investigated modulation techniques relative to those of riskTCM for riskTCM's optimal tube voltage (i.e. the tube voltage for which riskTCM achieves the lowest effective dose). All values are mean values over all patients and slices given for a constant iodine CNR. The values in sub- and superscript denote the minimum and maximum values. U_{low} refers to the lowest tube voltage allowed in the simulation.

	U_{low}	mAsTCM	riskTCM	riskTCTVM
Shoulder	70 kV	$1.84\,^{2.21}_{1.35}$	$1.01\,^{1.03}_{1.00}$	$0.87\,^{0.96}_{0.80}$
	60 kV	$1.84\,^{2.21}_{1.35}$	$1.00\,^{1.00}_{1.00}$	$0.75\,^{0.85}_{0.68}$
	50 kV	$1.84\,^{2.21}_{1.35}$	$1.00\,^{1.00}_{1.00}$	$0.72\,^{0.81}_{0.65}$
Thorax	70 kV	$1.36\,^{2.01}_{1.05}$	$1.04\,^{1.11}_{1.00}$	$1.02\,^{1.11}_{0.92}$
	60 kV	$1.33\,^{2.00}_{1.05}$	$1.00\,^{1.00}_{1.00}$	$0.94\,^{1.01}_{0.85}$
	50 kV	$1.33\,^{2.00}_{1.05}$	$1.00\,^{1.00}_{1.00}$	$0.93\,^{0.98}_{0.81}$
Abdomen	70 kV	$1.73\,^{2.44}_{1.34}$	$1.06\,^{1.15}_{1.03}$	$1.05\,^{1.15}_{1.00}$
	60 kV	$1.69\,^{2.37}_{1.30}$	$1.00\,^{1.02}_{1.00}$	$0.94\,^{0.99}_{0.88}$
	50 kV	$1.69\,^{2.37}_{1.30}$	$1.00\,^{1.00}_{1.00}$	$0.89\,^{0.97}_{0.81}$
Pelvis	70 kV	$1.52\,^{2.49}_{1.11}$	$1.03\,^{1.06}_{1.01}$	$0.97\,^{1.06}_{0.81}$
	60 kV	$1.50\,^{2.49}_{1.08}$	$1.00\,^{1.00}_{1.00}$	$0.87\,^{1.00}_{0.69}$
	50 kV	$1.50\,^{2.49}_{1.08}$	$1.00\,^{1.00}_{1.00}$	$0.84\,^{0.99}_{0.65}$

iii.) Maximum Requested Tube Current

In clinical practice, the optimal voltage can not always be selected due to tube current constraints. In these cases, a higher tube voltage is chosen. Therefore, also the maximum tube current requested by riskTCTVM was compared to the maximum tube current of mAsTCM at 70 kV, the lowest available tube voltage in current clinical practice. Figure 3.10 shows the maximum tube current requested by riskTCTVM for a lowest voltage of 70 kV relative to the maximum tube current of mAsTCM at 70 kV. For anatomies in the abdomen and thorax, riskTCTVM for $U_{\text{low}} = 70\,\text{kV}$ requests maximum tube current values of up to 226 % and 211 % of the maximum tube current of mAsTCM at $U = 70\,\text{kV}$. For eccentric anatomies in the shoulder and the pelvis, the maximum tube current requested by riskTCTVM is instead lower than the maximum tube current requested by mAsTCM. Table 3.2 summarizes the results for the maximum requested tube current for the different body regions and different minimum voltages. Only for the shoulder, the maximum tube current requested by riskTCTVM for $U_{\text{low}} = 70\,\text{kV}$ is on average 15 % lower than for mAsTCM at 70 kV. For all other body regions and voltages, the maximum tube current requested by riskTCTVM is on average higher than the maximum tube current of mAsTCM at 70 kV. For riskTCM, the maximum requested tube current is always higher than the maximum tube current of mAsTCM at 70 kV.

Table 3.2: Maximum tube current values of the investigated modulation techniques relative to those of mAsTCM at 70 kV. All values are mean values over all patients and slices given for a constant iodine CNR. The values in sub- and superscript denote the minimum and maximum values. U_{low} refers to the lowest tube voltage allowed in the simulation. For mAsTCM, average values below one occur for the shoulder because the optimal voltage for mAsTCM is for some anatomies in the shoulder 75 kV.

	U_{low}	mAsTCM	riskTCM	riskTCTVM
Shoulder	70 kV	$0.92\,^{1.00}_{0.74}$	$1.50\,^{1.68}_{1.34}$	$0.85\,^{1.09}_{0.73}$
	60 kV	$0.92\,^{1.00}_{0.74}$	$2.08\,^{2.32}_{1.84}$	$1.15\,^{1.46}_{0.93}$
	50 kV	$0.92\,^{1.00}_{0.74}$	$2.08\,^{2.32}_{1.84}$	$1.95\,^{3.16}_{1.22}$
Thorax	70 kV	$1.00\,^{1.00}_{1.00}$	$1.63\,^{2.08}_{1.21}$	$1.60\,^{2.11}_{1.02}$
	60 kV	$1.38\,^{1.90}_{1.00}$	$2.68\,^{3.71}_{1.68}$	$2.90\,^{4.18}_{1.49}$
	50 kV	$1.38\,^{1.90}_{1.00}$	$2.68\,^{3.71}_{1.68}$	$4.91\,^{9.55}_{2.14}$
Abdomen	70 kV	$1.00\,^{1.00}_{1.00}$	$1.91\,^{2.17}_{1.65}$	$1.97\,^{2.26}_{1.68}$
	60 kV	$1.44\,^{1.92}_{1.31}$	$3.65\,^{4.38}_{2.40}$	$3.55\,^{4.15}_{2.36}$
	50 kV	$1.44\,^{1.92}_{1.31}$	$3.86\,^{5.65}_{2.40}$	$5.82\,^{8.02}_{3.89}$
Pelvis	70 kV	$1.00\,^{1.00}_{1.00}$	$1.61\,^{2.09}_{1.02}$	$1.39\,^{2.03}_{0.60}$
	60 kV	$1.32\,^{2.02}_{1.00}$	$2.53\,^{4.25}_{1.40}$	$2.01\,^{3.63}_{0.93}$
	50 kV	$1.32\,^{2.02}_{1.00}$	$2.53\,^{4.25}_{1.40}$	$2.59\,^{4.55}_{1.60}$

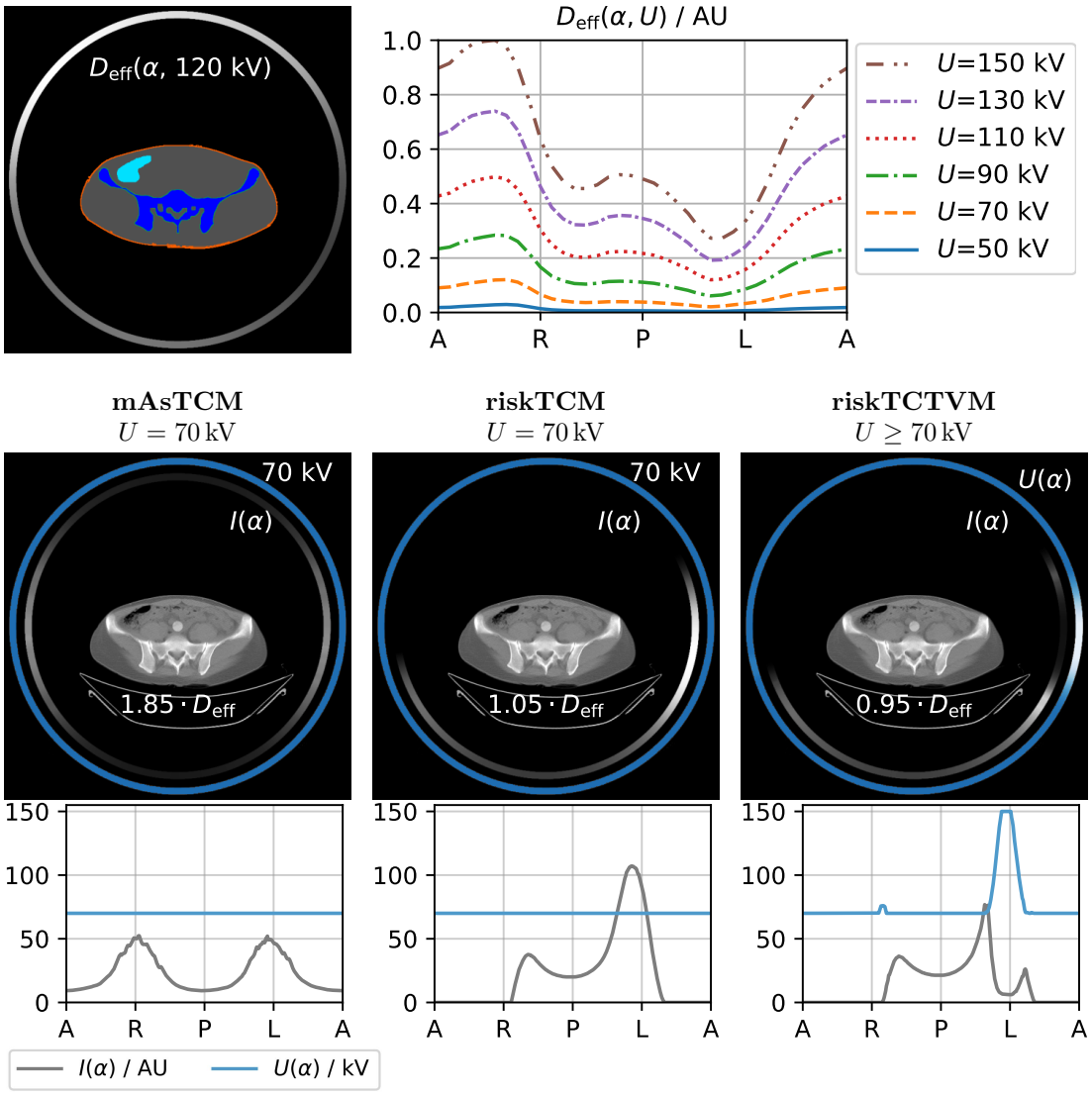

Relative effective dose

U_{low}	mAsTCM	riskTCM	riskTCTVM
70 kV	1.85	1.05	0.95
60 kV	1.82	1.00	0.80
50 kV	1.82	1.00	0.74

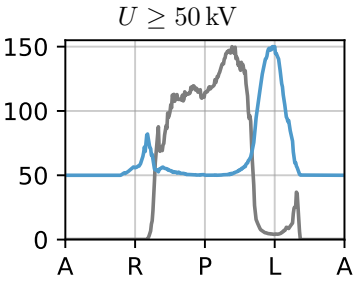

Figure 3.4: CNRD optimization for a slice in the pelvis of a female patient. The effective dose values are given at constant CNR and relative to riskTCM at its best voltage which is 60 kV for this anatomy.

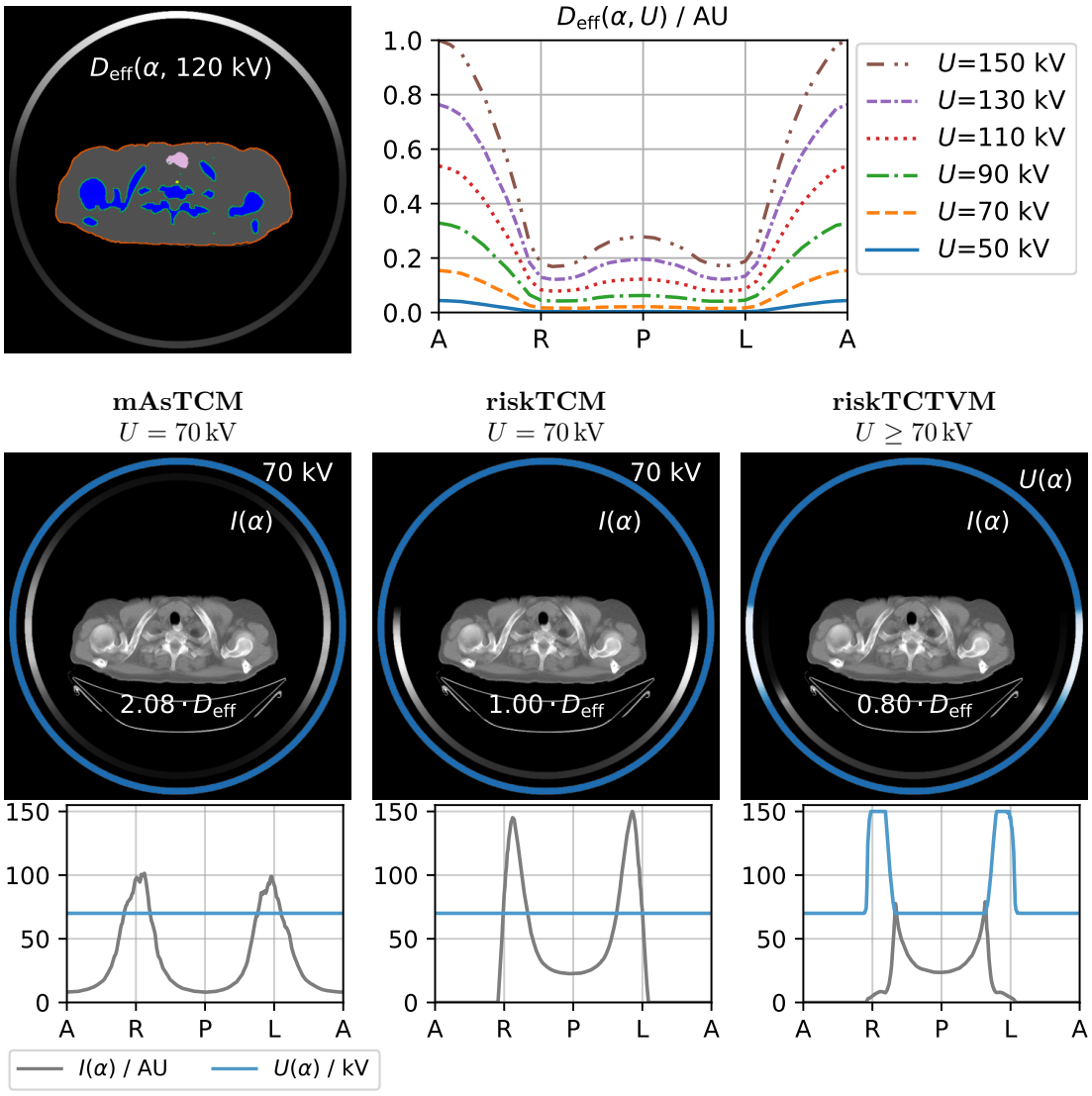

Relative effective dose

U_{low}	mAsTCM	riskTCM	riskTCTVM
70 kV	2.08	1.00	0.80
60 kV	2.08	1.00	0.68
50 kV	2.08	1.00	0.65

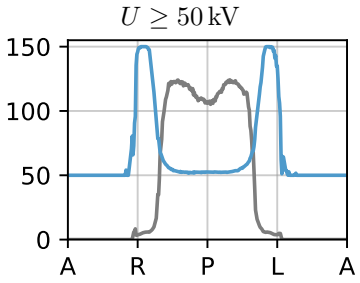

Figure 3.5: CNRD optimization for a slice in the shoulder of a male patient. The effective dose values are given at constant CNR and relative to riskTCM at its best voltage which is 70 kV for this anatomy.

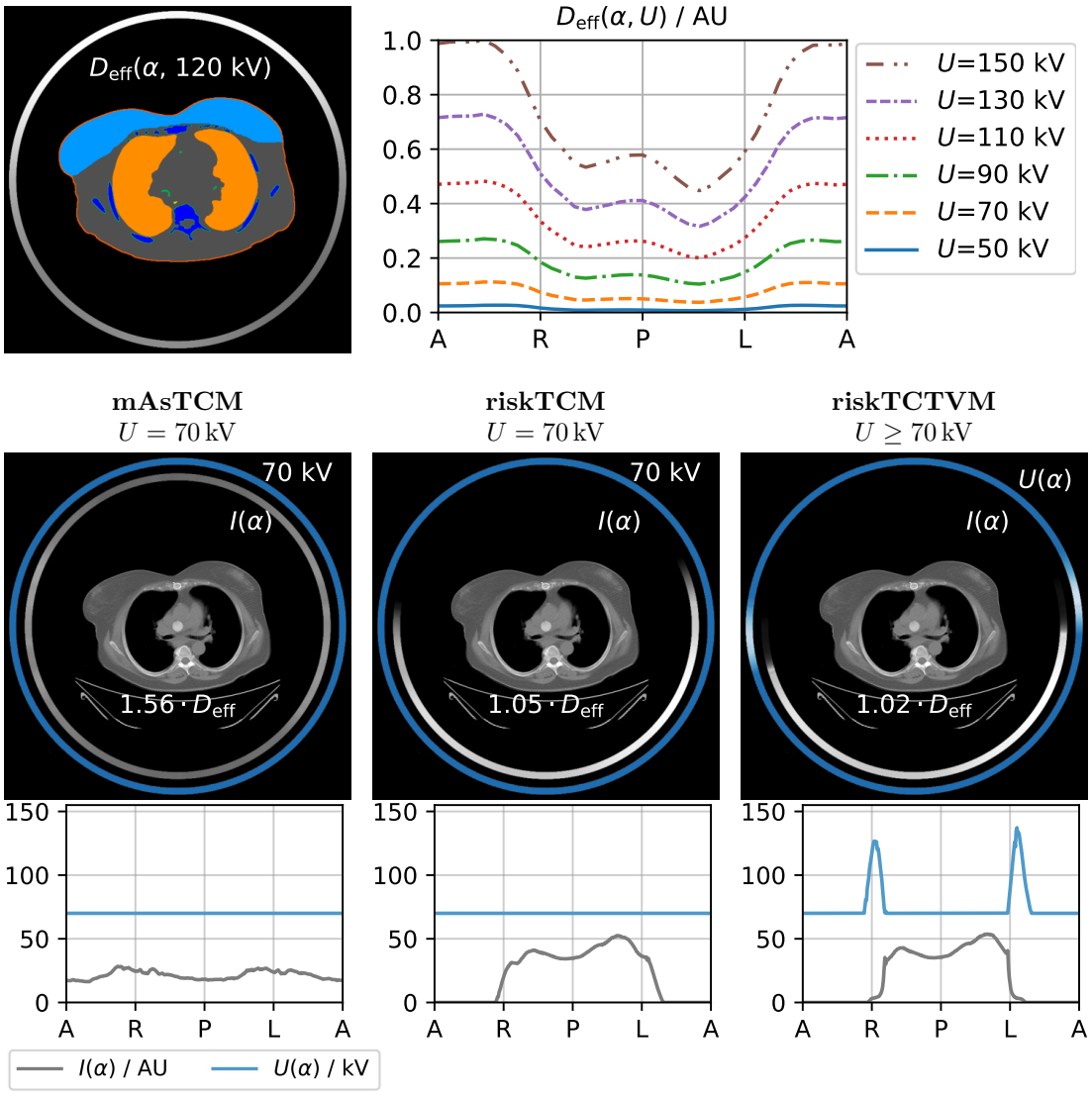

Relative effective dose

U_{low}	mAsTCM	riskTCM	riskTCTVM
70 kV	1.56	1.05	1.02
60 kV	1.53	1.00	0.92
50 kV	1.53	1.00	0.91

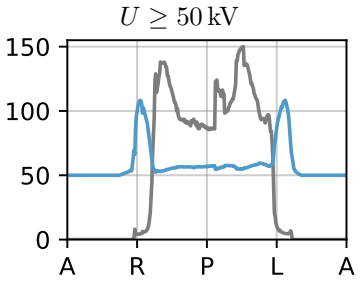

Figure 3.6: CNRD optimization for a slice in the thorax of a female patient. The effective dose values are given at constant CNR and relative to riskTCM at its best voltage which is 60 kV for this anatomy.

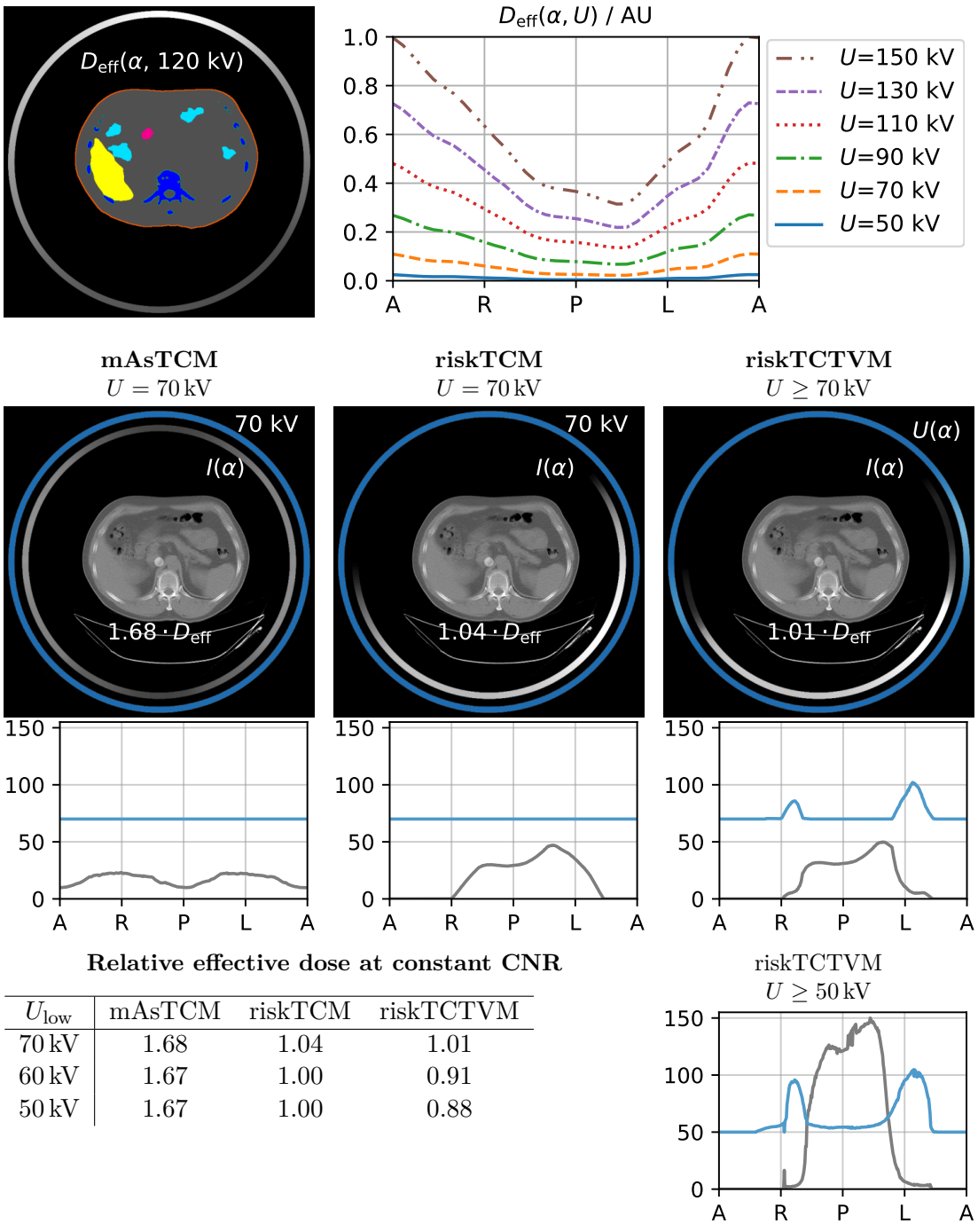

Relative effective dose at constant CNR

U_{low}	mAsTCM	riskTCM	riskTCTVM
70 kV	1.68	1.04	1.01
60 kV	1.67	1.00	0.91
50 kV	1.67	1.00	0.88

Figure 3.7: CNRD optimization for a slice in the abdomen of a male patient. The effective dose values are given at constant CNR and relative to riskTCM at its best voltage which is 60 kV for this anatomy.

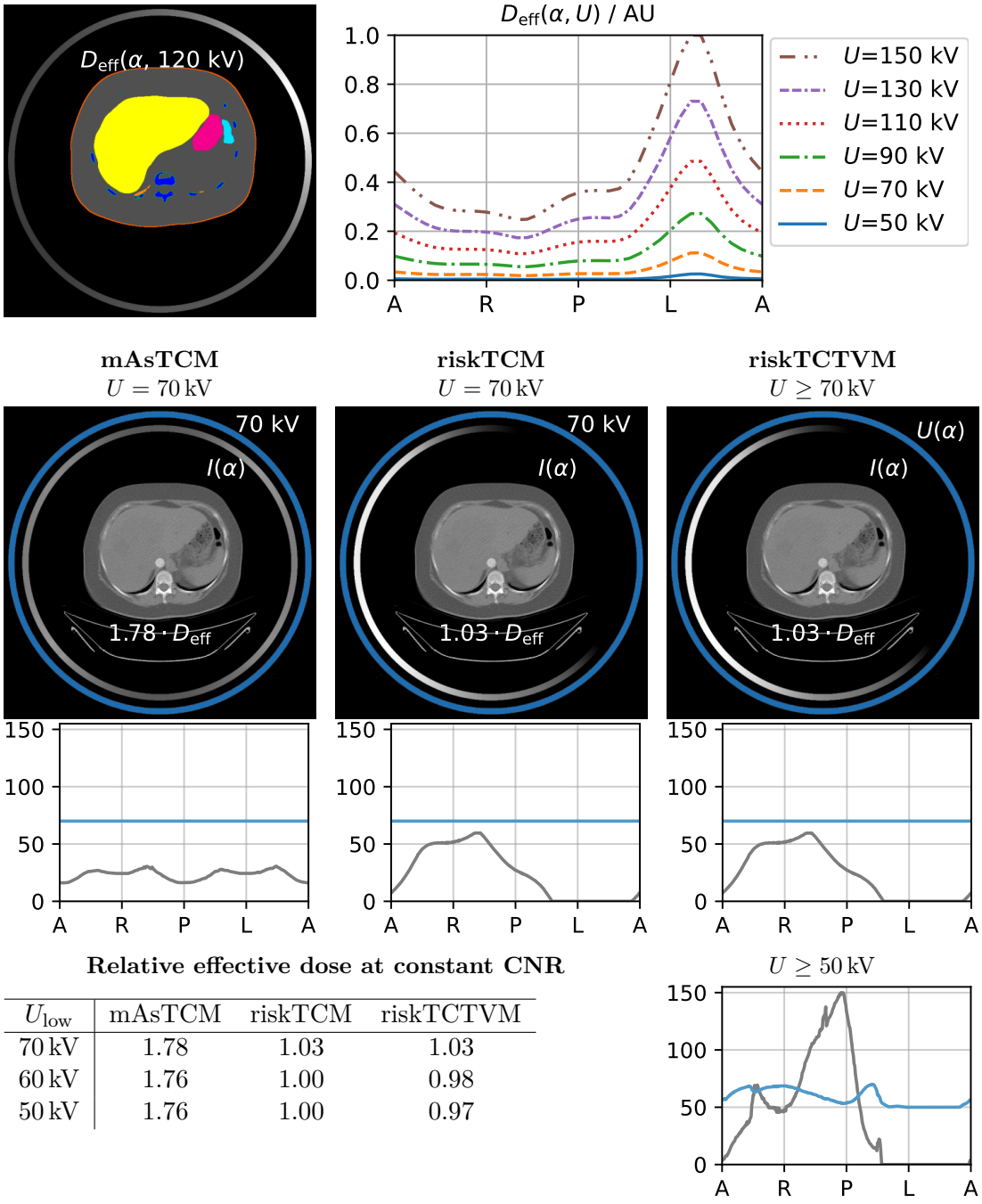

Relative effective dose at constant CNR

U_{low}	mAsTCM	riskTCM	riskTCTVM
70 kV	1.78	1.03	1.03
60 kV	1.76	1.00	0.98
50 kV	1.76	1.00	0.97

Figure 3.8: CNRD optimization for a slice in the abdomen of a female patient. The effective dose values are given at constant CNR and relative to riskTCM at its best voltage which is 60 kV for this anatomy.

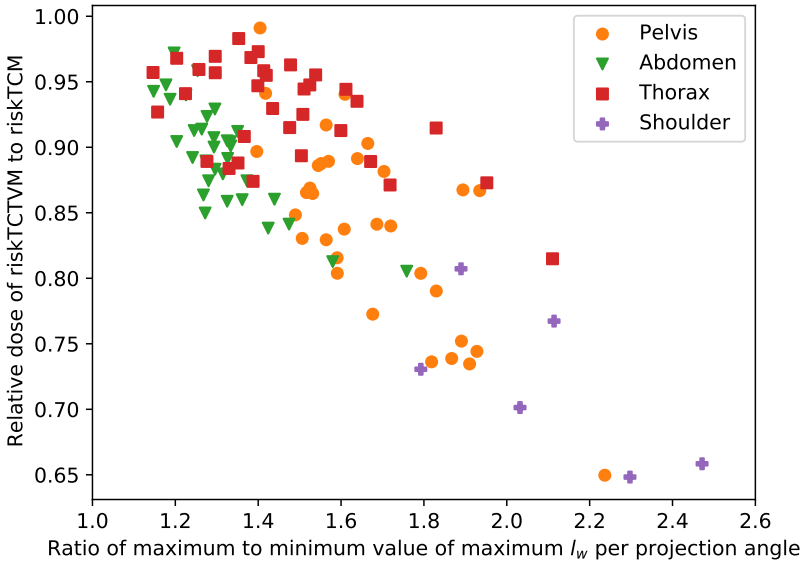

Figure 3.9: Effective dose of riskTCTVM relative to the effective dose of riskTCM for $U_{\text{low}} = 50\,\text{kV}$ for different body regions at constant iodine CNR. The x-axis shows the ratio of the maximum to the minimum value of the maximum water intersection length l_{W} per projection angle.

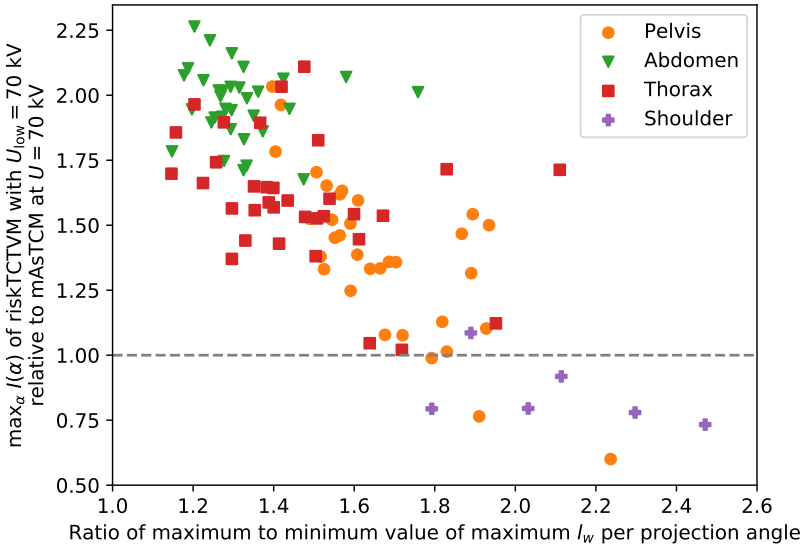

Figure 3.10: Maximum tube current requested by riskTCTVM for $U_{\text{low}} = 70\,\text{kV}$ relative to mAsTCM at $U = 70\,\text{kV}$ for different body regions at constant iodine CNR. The x-axis shows the ratio of the maximum to the minimum value of the maximum water intersection length l_{W} per projection angle.

4 Spiral Start Angle Optimization

This chapter reproduces the study on the spiral start angle optimization that was published in reference [65] under a CC BY-NC 4.0 license (`https://creativecommons.org/licenses/by-nc/4.0/`). I conducted the scientific work and wrote the original draft for reference [65]. This chapter contains the introduction, materials and methods, and the results section of reference [65]. The formatting was adapted to match the format of this thesis. The introduction and the subsection regarding the effective dose calculation in the materials and methods section were shortened with references to the previous chapters to avoid repetitions. A discussion of the study is given in chapter 5 which contains reproduced parts of the discussion in reference [65].

4.1 Introduction

The approach proposed in chapter 3 considers a combined tube current and tube voltage modulation. While the voltage affects the photon's energy distribution, the tube current controls the number of photons emitted by the X-ray tube. The study presented in this chapter investigates an approach different from controlling the photons' energy distribution or the number of photons incident on the patient's body. Instead, this study investigates the effect of rotations of spiral tube trajectories, produced by different tube start angles, on patient dose. For spiral scan trajectories, non-uniform quasiperiodic dose patterns are created, resulting in dose variations particularly in the periphery regions of the scanned object [17], [66], [67]. The tube start angle determines the longitudinal shift of these quasiperiodic dose patterns which affects organ dose values, especially for small peripheral organs [18]. Since the tube start angle is currently not controlled in scan protocols on clinical scanners and can be considered a random scan parameter, many studies quantifying the dose induced by a CT scan treat the tube start angle as a source of uncertainty about the true dose distribution [68]. Other studies instead considered the potential of reducing the dose to single organs by selecting the optimal start angle, i.e. the one resulting in the lowest organ dose [17], [18]. Crucial parameters here are the table feed per rotation d and the collimation C of the scanner whose ratio $p = d/C$ is named pitch value. If an organ is sufficiently small compared to the table feed and the collimation, the selection of the optimal start angle can cause the

complete avoidance of X-ray tube positions anterior to that organ. For organs that are longer than the table feed, different tube start angles might change the number of times the X-ray passes in front of this organ or the longitudinal position of anterior irradiation; e.g. the dose for an anterior position in the center of the longitudinal range of the organ could be different to a position in the periphery of the organ. Hence, the collimation of the scanner and the choice of pitch value determine for a given patient anatomy the organ dose variations caused by different start angles. Winslow et al. considered in their study a collimation of 24 mm [17] and Zhang et al. collimations up to 40 mm [18]. We here extend their studies by considering collimations of 40 mm, 60 mm, and 80 mm which became available since then. Furthermore, besides the dose reduction potential for single organs, we study if the effective dose as a weighting of different organ doses and measure of the overall radiation risk would also benefit from a dose-optimized choice of the tube start angle. Moreover, in addition to single source CT (SSCT), we also consider dual source CT (DSCT) which allows us to study pitch values above 1.5; a pitch value of about 1.5 is the limit for SSCT for mathematically complete projection data [69]. High pitch values decrease the scan time which is for example beneficial to reduce breathing or cardiac motion artifacts, or to avoid sedation when scanning babies and toddlers [70]. A pitch value of 3 for example allows to scan the entire chest in the order of 1.5 s [70]. Finally, in addition to a constant tube current, we also consider today's standard tube current modulation (TCM) minimizing the mAs-product.

In summary, compared to previous studies regarding a dose reduction potential for single organs by selecting a start angle for scans with constant tube current and collimations up to 40 mm [17], [18], our study makes the following contributions:

- study of collimations between 40 mm and 80 mm
- study of the dose reduction potential of the effective dose as a weighting of different organ doses
- study of DSCT
- consideration of mAs–minimizing tube current modulation (mAsTCM).

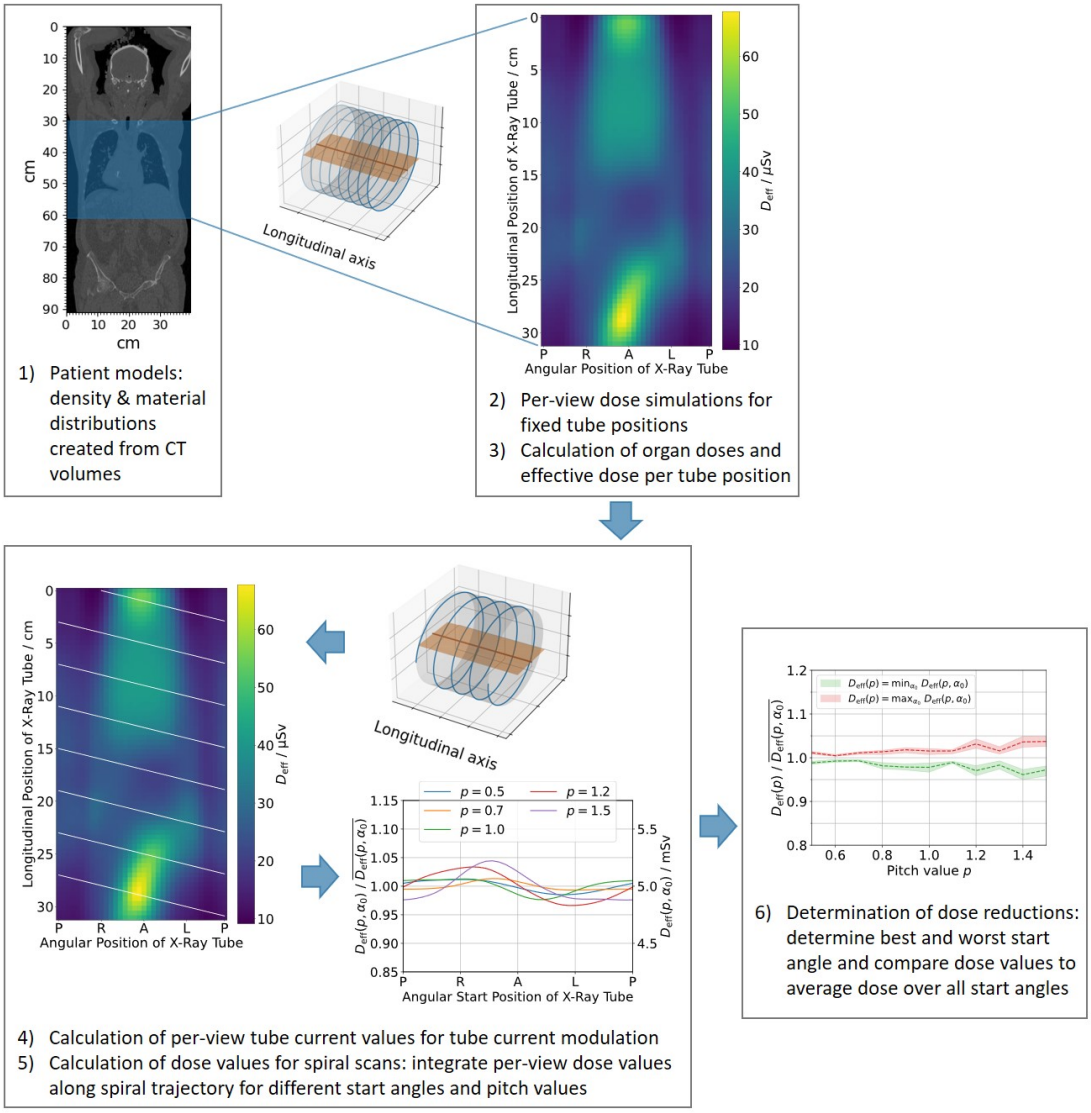

Figure 4.1: Sketch of the general concept of our study. For patient models derived from CT volumes (1), dose simulations at different tube positions in the thorax region are performed (2) and the respective organ doses and effective doses are calculated (3). Including tube current modulation (4), these per-view doses are then integrated along spiral trajectories for different pitch values and tube start angles (5). Finally, the dose decrease and increase of the best and worst start angle are calculated with respect to the mean dose over all start angles (6).

4.2 Materials and Methods

Figure 4.1 shows the general concept of our study. In short, the procedure is as follows:

1. create patient models by calculating density and material distributions from patient CT volumes
2. perform per-view Monte Carlo dose simulations for X-ray tube positions covering the whole scan range
3. calculate per-view organ doses and effective doses from the resulting dose distributions
4. calculate per-view tube current values according to mAsTCM
5. integrate per-view dose values along spiral trajectories for different tube start angles and different pitch values considering either a constant tube current or mAsTCM
6. determine the best and worst tube start angle, i.e. the one resulting in the lowest and the highest dose, for every pitch value and calculate the corresponding doses relative to the average dose over all start angles

The following sections 4.2.1-4.2.6 describe each of the steps in more detail.

4.2.1 Patient Models

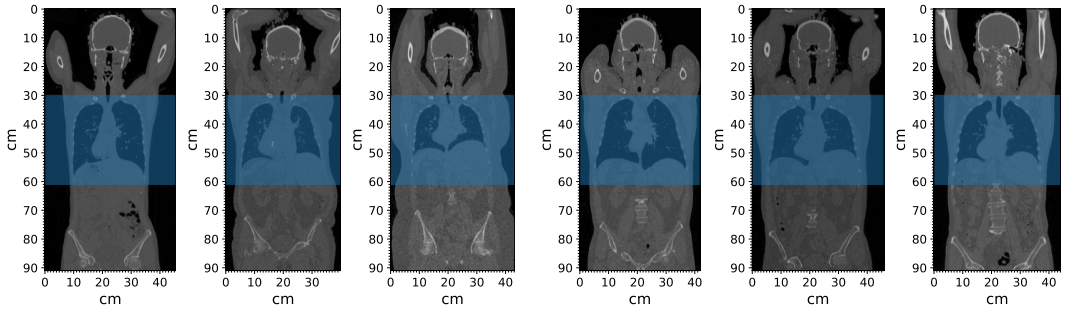

(a) Female patients (b) Male patients

Figure 4.2: Patients that were used for the dose simulations in this study. The blue rectangulars indicate the scan range for which dose simulations were performed.

The patient models were based on three female and male patients from the Visual Concept Extraction Challenge in Radiology (Visceral) [63] (see Figure 4.2). Applying a threshold-based segmentation, every voxel of the CT volume was assigned to one of five materials (air, lung tissue, fat, water, bone). The corresponding density distribution $\rho(\boldsymbol{r})$ was calculated from the CT values. We used the organ segmentations that were

already used for the risk-minimizing tube current modulation riskTCM [15] and were created as described in reference [15].

4.2.2 Dose Simulations

Our procedure to obtain dose values for different spiral scans is as follows: we once perform dose simulations for single tube positions to obtain per-view dose values; subsequently, we integrate these per-view dose distributions along spiral trajectories with different pitch values and different tube start angles considering either a constant tube current or mAsTCM. Using our in-house Monte Carlo dose simulation software, we simulated dose distributions $D(\boldsymbol{s}(\alpha, z), \boldsymbol{r})$ for tube positions described by

$$\boldsymbol{s}(\alpha, z) = \begin{pmatrix} R_\mathrm{F} \sin\alpha \\ -R_\mathrm{F} \cos\alpha \\ z \end{pmatrix} \quad \text{with } R_\mathrm{F} = 595\,\mathrm{mm} \tag{4.1}$$

where R_F denotes the distance from the X-ray tube to the isocenter, α the angular position of the X-ray tube, and z the longitudinal position along the table axis. We performed simulations for tube positions with an angular increment of $\Delta\alpha = 10^\circ$ and a longitudinal increment of $\Delta z = 4.5\,\mathrm{mm}$ over a scan range of 31.5 cm (resulting in 70 longitudinal positions) in the thorax region of the patients. The thorax was chosen as short scan times and thus high pitch values are particularly relevant in this body region due to breathing and cardiac motion. With a pitch value of 3, for example, the entire chest can be scanned in the order of 1.5 s and the heart in a third of a second [70]. These short scan times are advantageous for scanning adults who cannot hold their breath, to reduce motion artifacts, and to avoid sedation when scanning babies and toddlers [70]. The simulations were performed for three different collimation values C, namely $C = 40\,\mathrm{mm}, 60\,\mathrm{mm}$, and $80\,\mathrm{mm}$ which can be related to a range of high-end and mid-range CT systems [3]. For the source spectrum, we used a Tucker spectrum [26] at 120 kV filtered by 6 mm aluminum and a bowtie filter. All simulations were performed with the same number of photons. As the number of photons is proportional to the tube current, the dose simulations can be considered to be performed for a constant tube current. As dose is also proportional to the number of photons and thus the tube current, scaling the dose values to a different tube current is a simple multiplication. This relationship allows us to use the same simulations for scans with and without TCM as we obtain per-view dose values for TCM by multiplying each dose value with the respective tube current value for this view.

4.2.3 Calculation of Organ Doses and Effective Dose

The calculation of organ doses and effective dose from the simulated dose distributions was performed as described in section 3.2.3.

4.2.4 Tube Current Modulation (TCM)

In our study, we consider spiral scans with constant tube current and with mAs-minimizing tube current modulation. According to the derivation by Gies et al., the tube current should be proportional to the square root of the attenuation in order to minimize the noise in the central pixel at constant mAs-product [10]. In the polychromatic case, the projection value q for a line L through the object is

$$q(L) = -\ln \int dE\ w(E) e^{-\int dL \mu(\boldsymbol{r},E)}$$

where $w(E)$ denotes the detected X-ray spectrum normalized to unit area and $\mu(\boldsymbol{r}, E)$ denotes the attenuation value as a function of position $\boldsymbol{r}$ and photon energy E. For the detector, we assumed an energy integrating Gd_2O_2S (gadolinium oxysulfide) scintillator layer with a thickness of 1.4 mm and density of $7.32\,\mathrm{g\,cm^{-3}}$.

For the polychromatic case, we thus find for the tube current

$$I_{\mathrm{mAsTCM}}(\alpha) \propto \sqrt{e^{q(\alpha)}}$$

where $q(\alpha)$ is the polychromatic attenuation for a specific projection. Considering water-precorrection introduces the derivative of the water precorrection function $P(q)$ to q to the control of the tube current:

$$I_{\mathrm{mAsTCM}}(\alpha) \propto P'(q(\alpha))\sqrt{e^{q(\alpha)}}.$$

Hence, the tube current is only depending on the projection values q. This dependency allows us to precompute the tube current values for every patient for all tube positions. By multiplying the dose values for every tube position with the tube current value at the respective position, we obtain dose values as a function of tube position for TCM. We want to stress here that the TCM curves computed by us model only the relative course of the tube current applied in a clinical scan. To obtain the absolute dose values that a patient would receive during a clinical scan, we would need to know the scaling of the tube current. However, the scaling of the tube current values does not affect the relative dose values presented in this study. As the dose is proportional to the tube current, a different scaling of the tube current does not change these relative dose values.

4.2.5 Calculation of Dose Values for Spiral Scans

Given the dose values for every tube position, we can calculate the dose for a spiral scan by integrating these per-view dose values along the respective spiral trajectory. The tube positions are defined by the longitudinal position z and the angular position α (see equation 4.1). For the integration along a spiral trajectory, we parameterize the tube angle α with the longitudinal position z. For a given spiral defined by a start position (α_0, z_0) and the pitch value $p = d/C$, where d denotes the table feed per full

gantry rotation, this parameterization of the tube angle α reads

$$\alpha(z, p, a_0, z_0) = \pm\frac{z - z_0}{p \cdot C} \cdot 360^\circ + \alpha_0. \tag{4.2}$$

In the following, we drop the dependency on the longitudinal tube start position z_0 as z_0 is constant throughout our study. Whether there is a plus or minus in front of the first term in equation 4.2 depends on the rotation of the X-ray tube relative to the patient table movement, i.e. if the rotation is clockwise or counterclockwise to the table axis (compare figure 4.3). With equations 4.2 and 4.1 we can define a spiral trajectory $\boldsymbol{s}_{\text{spiral}}$ by

$$\boldsymbol{s}_{\text{spiral}}(z, p, \alpha_0) = \boldsymbol{s}(\alpha(z, p, \alpha_0), z)$$

With this definition, we can express the integration of dose along a spiral trajectory:

$$D_{\text{eff}}(p, \alpha_0, I) = \sum_z D_{\text{eff}}(\boldsymbol{s}_{\text{spiral}}(z, p, \alpha_0)) \cdot I(\boldsymbol{s}_{\text{spiral}}(z, p, \alpha_0)), \tag{4.3}$$

where we used a longitudinal increment of $\Delta z = \Delta\alpha/360^\circ \cdot pC$ with $\Delta\alpha = 10^\circ$ and linear interpolation of $D_{\text{eff}}(\boldsymbol{s}(\alpha, z))$ in z. We considered a constant tube current (noTCM) and mAs-minimizing TCM (mAsTCM) as described in section 4.2.4. This gives us the dose for SSCT with and without TCM. For the case of DSCT, we evaluated equation (4.3) for two spiral trajectories with a difference of 90° in the tube start angle α_0 and summed both values up. Figure 4.3 visualizes one example of such two trajectories for DSCT besides a clockwise and counterclockwise spiral trajectory for SSCT.

4.2.6 Determination of Dose Reductions

In our study, we consider four different scan scenarios, i.e. SSCT and DSCT with and without mAsTCM. For SSCT, we consider pitch values between 0.5 and 1.5 for SSCT and pitch values between 0.5 and 3 for DSCT. For SSCT, the maximum pitch value that yields mathematically complete projection data is about 1.5 [69]. For DSCT, the pitch value may even exceed 3, depending on the desired field of view [69]. For a field of view of 35.4 cm, a pitch of 3 is the maximum pitch value for Siemens scanners [71].

For a given pitch value and scan scenario, we calculate the dose according to equation 4.3 for spiral scans with start angles between zero and 360 degrees. As a random start angle is common in clinical practice, we report all dose values relative to the mean dose value over all start angles which can be interpreted as the expectation value of the dose. Consequently, the dose reduction of the best start angle compared to the mean dose for a given pitch value is given by

$$\text{Dose reduction}(p) = 1 - \frac{\min_{\alpha_0} D(p, \alpha_0)}{\overline{D(p, \alpha_0)}}. \tag{4.4}$$

Analogously, the dose increase of the worst start angle compared to the mean dose is

$$\text{Dose increase}(p) = \frac{\max_{\alpha_0} D(p, \alpha_0)}{\overline{D(p, \alpha_0)}} - 1. \tag{4.5}$$

Furthermore, we also define the maximum dose reduction as Zhang et al. [18] for which the dose of the best start angle is compared to the dose of the worst start angle:

$$\text{Dose reduction}_{\max}(p) = 1 - \frac{\min_{\alpha_0} D(p, \alpha_0)}{\max_{\alpha_0} D(p, \alpha_0)}. \tag{4.6}$$

For the study of these relative doses, we considered always both directions of rotation (compare equation (4.2) and figure 4.3).

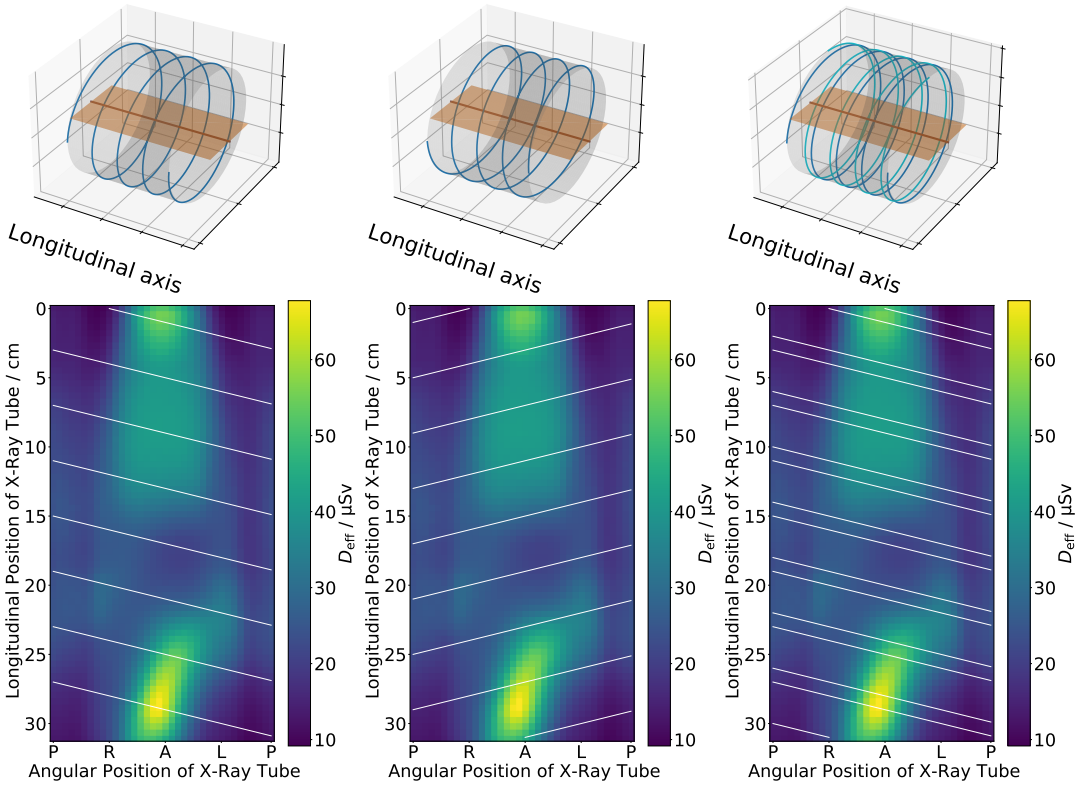

(a) SSCT, clockwise (b) SSCT, counterclockwise (c) DSCT, clockwise

Figure 4.3: Visualization of different spiral trajectories with pitch value $p = 1$ for a collimation of $C = 40\,\text{mm}$ for clockwise (a) and counterclockwise (b) rotation in the case of SSCT and clockwise rotation in the case of DSCT (c) where the angular difference between both trajectories is 90°. Visualizations are in the three-dimensional space (top row) and overlayed in white over the effective dose as a function of longitudinal and angular position for one example patient (bottom row). The labels of the angular tube position refer to posterior (P), right (R), anterior (A), left (L), and posterior (P) from the patient's perspective.

4.3 Results

4.3.1 Contributions of Single Organ Doses

Figure 4.4 shows the simulated effective dose as a function of the angular and longitudinal tube position for all studied patients for a constant tube current. As the effective dose is defined as a weighted sum of organ doses, these plots of the effective dose are a weighted overlay of the different organ contributions. Although the dependency of the effective dose on the tube position is different for every patient due to different anatomies, it is dominated by a few radiosensitive organs. These organs are the stomach, the thyroid gland, and the lung for the studied scan region. For the female patients, also the breast induces major contributions to the effective dose. Figure 4.5 shows the decomposition of the effective dose to these organs with major contributions for one female patient. These visualizations of the organ doses as a function of the tube position show also the spatial extent and location of the organs which has a major impact on the possible dose reductions for a single organ. This is illustrated by the overlayed best and worst trajectory for a SSCT scan with constant tube current and pitch 1.5. In the case of the thyroid gland, the worst trajectory irradiates the thyroid from anterior positions resulting in high thyroid doses whereas the best trajectory avoids these positions by starting with irradiation from side and posterior positions so that once the tube passes anterior positions, the dose deposited to the thyroid gland is already close to zero due to the small longitudinal extent of the thyroid. Consequently, the thyroid dose of the worst start angle is more than twice as high as the lowest dose as figure 4.6 shows. Compared to the other organs, this is the highest relative dose variation caused by different start angles. In contrast, the dose variations for the lung, which expands over a large region, are negligible. For the breast, the dose variations are also negligible below a pitch of 1.5 (compare figure 4.6). For a pitch of 1.5, figure 4.5 shows that the worst trajectory irradiates the breasts three times from anterior positions whereas this is reduced to two times by the best trajectory. For the stomach, the situation is similar: here, the best trajectory irradiates the stomach just once from anterior positions whereas the worst trajectory does so twice. This difference results in a dose difference of about 20 % between the best and the worst start angle (see figure 4.6).

The best start angle in the case of the effective dose is the one that minimizes the weighted sum of organ doses. Hence, high dose reductions for different single organs might not be achievable if the corresponding start angles are very different. One example shows the comparison between pitch 1.2 and 1.5. While a pitch of 1.5 yields the highest dose reduction potential by selecting the best tube start angle for the stomach, the thyroid, and the breast, a pitch of 1.2 yields slightly higher dose reductions for the effective dose where the best tube start angles for the stomach and the thyroid are closer together (both close to the left side of the patient). Overall, however, dose variations are below 5 % for the effective dose. Here, the effective dose was scaled in a way that the average over all start angles is 5 mSv which was the mean effective dose of a chest CT in the years 2012-2013 in Germany [4]. For a mean effective dose of 5 mSv, dose variations below 5 % would correspond to absolute dose variations of below 0.25 mSv.

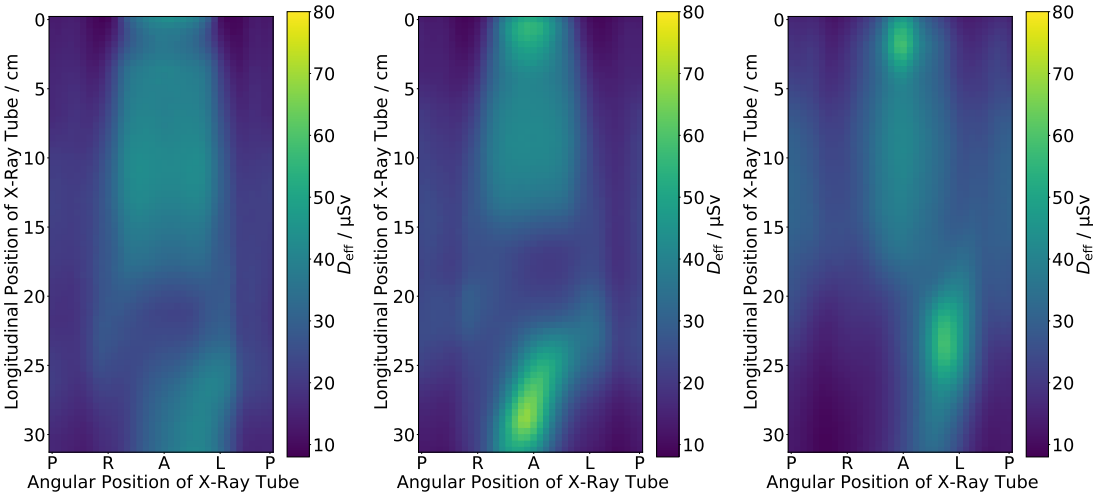

(a) Female patients

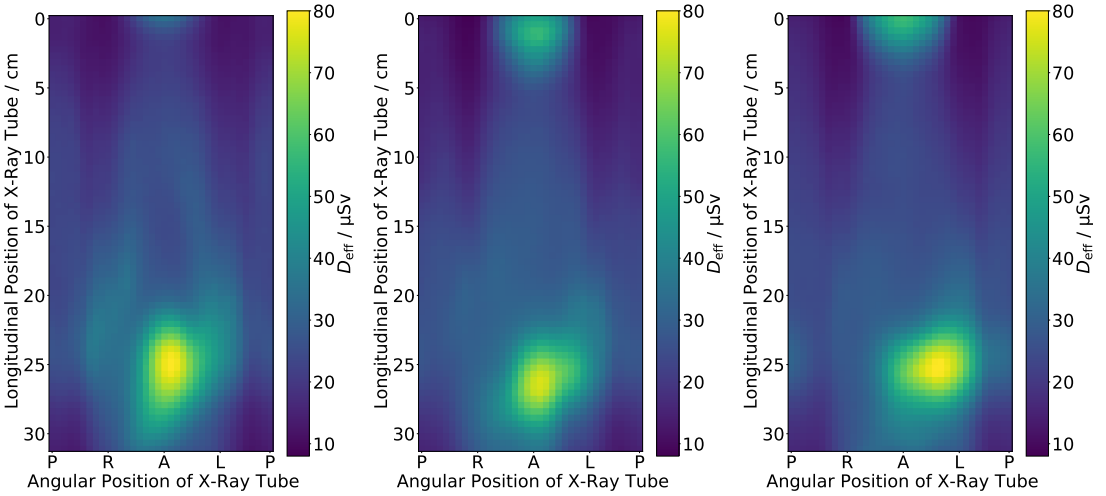

(b) Male patients

Figure 4.4: Simulated effective dose as a function of tube angle and longitudinal position for the studied female patients (a) and male patients (b) for a collimation of $C = 40\,\text{mm}$ and constant tube current. The dose values were scaled in a way such that the mean dose of a spiral trajectory with pitch 1.5 is 5 mSv. The labels of the angular tube position refer to posterior (P), right (R), anterior (A), left (L), and posterior (P) from the patient's perspective.

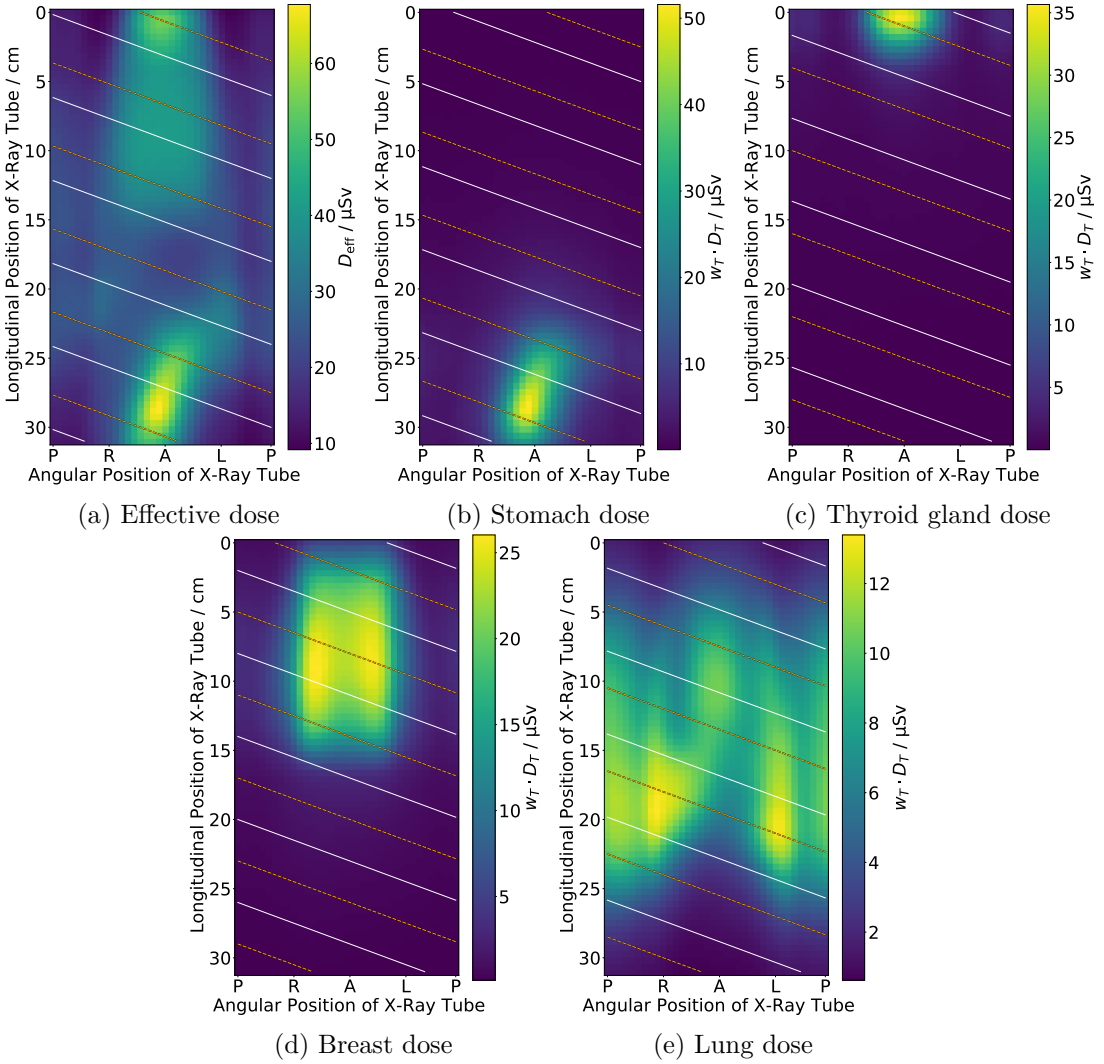

(a) Effective dose (b) Stomach dose (c) Thyroid gland dose

(d) Breast dose (e) Lung dose

Figure 4.5: Example of simulated effective dose (a) and weighted organ doses (b-e) as a function of tube angle and longitudinal position for a female patient for a collimation of $C = 40\,\text{mm}$ and constant tube current. The dose values were scaled in a way such that the average effective dose of a spiral trajectory with pitch 1.5 is 5 mSv. White solid lines indicate the best and orange dashed lines the worst trajectory for the effective dose and for the respective organ for a SSCT scan with clockwise rotation, constant tube current, and pitch 1.5. The labels of the angular tube position refer to posterior (P), right (R), anterior (A), left (L), and posterior (P) from the patient's perspective.

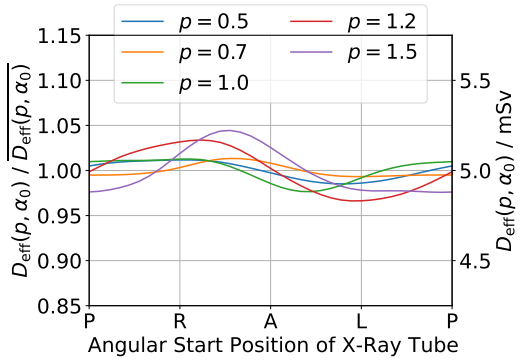

(a) Effective dose

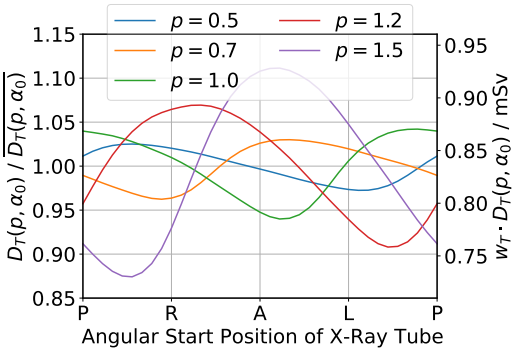

(b) Stomach dose

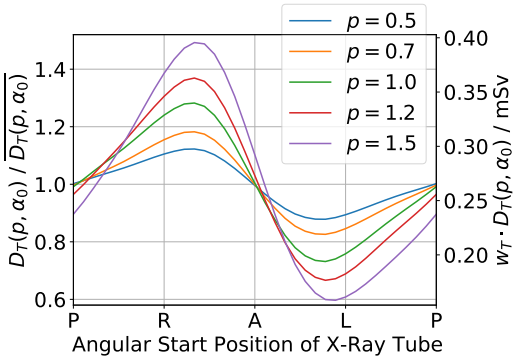

(c) Thyroid gland dose

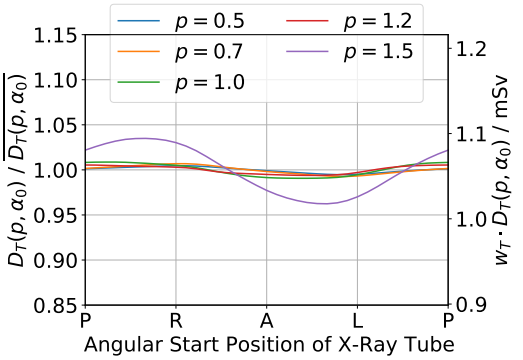

(d) Breast dose

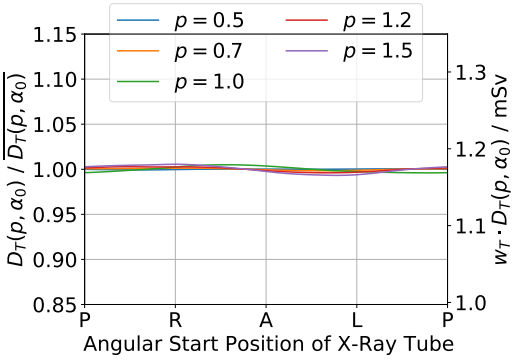

(e) Lung dose

Figure 4.6: Effective dose (a) and different organ doses (b-e) as a function of tube start angle for different pitch values p for SSCT with clockwise rotation, constant tube current, and a collimation of $C = 40\,\text{mm}$. The labels of the angular tube position refer to posterior (P), right (R), anterior (A), left (L), and posterior (P) from the patient's perspective. The dose values were scaled in a way such that the mean effective dose is 5 mSv.

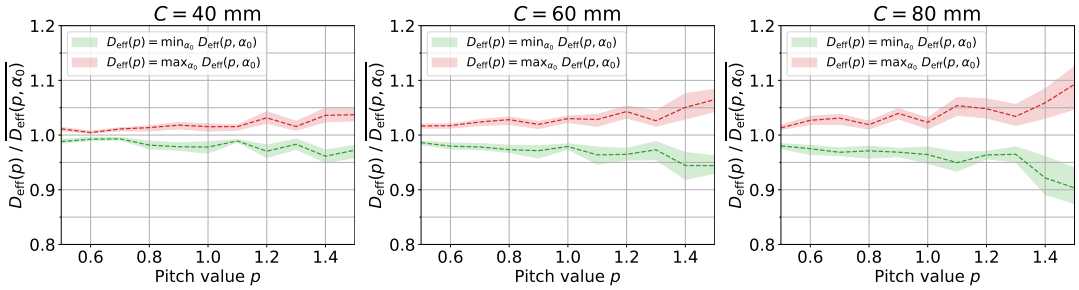

(a) SSCT, noTCM

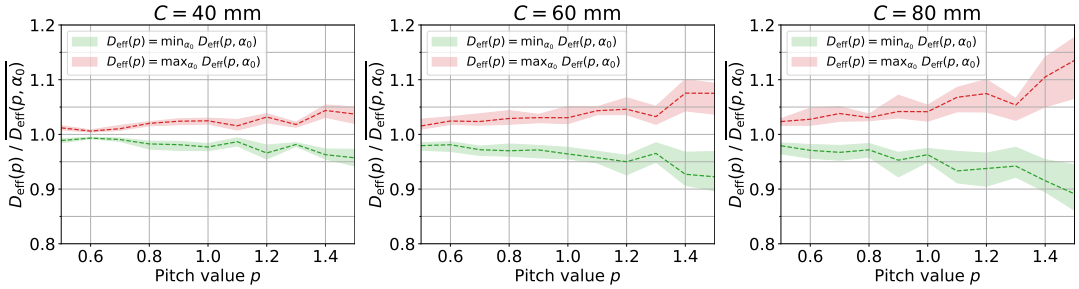

(b) SSCT, mAsTCM

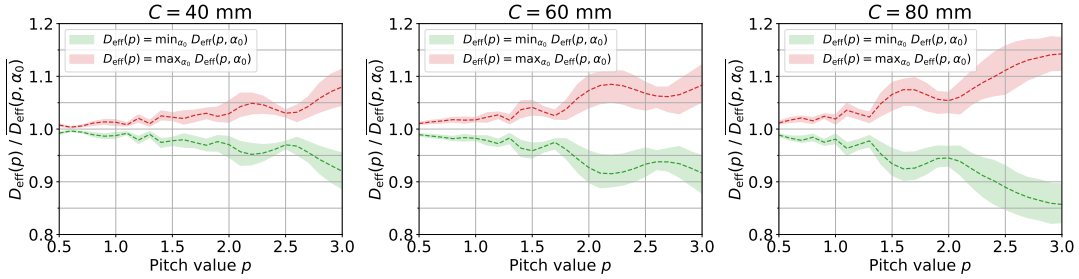

(c) DSCT, noTCM

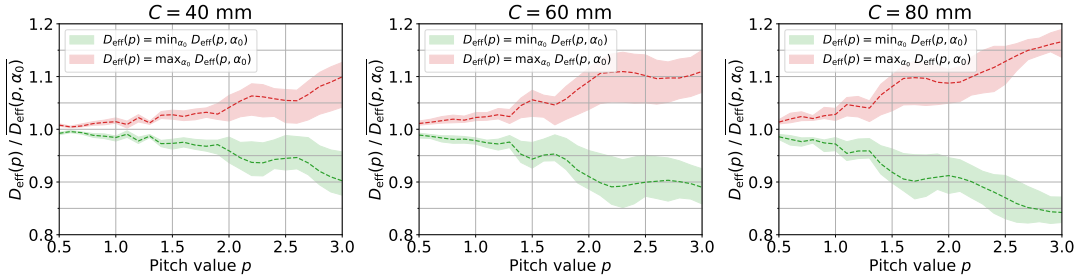

(d) DSCT, mAsTCM

Figure 4.7: Effective dose of the best (in green) and the worst (in red) start angle per pitch relative to the mean effective dose over all start angles. The dashed lines indicate the mean value over all patients. The color filling represents the range of the values among the studied patients.

4.3.2 Reduction of the Effective Dose for Different Scan Scenarios

We determined the best and the worst start angle and compared the resulting effective dose values to the mean value over all start angles, i.e. the expectation value of the effective dose for a random start angle as it is common clinical practice. We performed this calculation for all patients for different pitch values for SSCT and DSCT scans with and without TCM for three different collimations. The results are summarized in figure 4.7. Complementarily, table 4.1 displays the mean dose reduction of the best start angle to the average dose over all start angles and table 4.2 to the dose of the worst start angle for the highest studied pitch values. For the case of TCM, the dose deviations from the mean dose tend to be slightly higher than for noTCM. With increasing collimation, the dose variations increase. For a collimation of $C = 40\,\text{mm}$ and SSCT, the deviations from the mean dose value stay below 5 % for all patients. For DSCT with TCM, these deviations rise to 10 % on average for a pitch value of 3. For a collimation of $C = 80\,\text{mm}$ in SSCT, the minimum dose deviates on average up to 11 % from the mean value. The highest dose reduction potential we find for a pitch of 3 for the case of DSCT with TCM and a collimation of $C = 80\,\text{mm}$; here, the dose of the best starting angle is 16 % lower than the mean value and 28 % lower than the maximum value on average over the patients.

Table 4.1: Mean dose reductions of the best start angle compared to the average effective dose over all start angles in percent for the highest studied pitch values, i.e. 1.5 for SSCT and 3 for DSCT.

	Pitch		Collimation		
			40 mm	60 mm	80 mm
SSCT	1.5	noTCM	3 %	6 %	10 %
		mAsTCM	4 %	8 %	11 %
DSCT	3	noTCM	8 %	8 %	14 %
		mAsTCM	10 %	11 %	16 %

Table 4.2: Mean dose reductions of the best start angle compared to the worst start angle in percent for the highest studied pitch values, i.e. 1.5 for SSCT and 3 for DSCT.

	Pitch		Collimation		
			40 mm	60 mm	80 mm
SSCT	1.5	noTCM	6 %	11 %	17 %
		mAsTCM	8 %	14 %	21 %
DSCT	3	noTCM	15 %	15 %	25 %
		mAsTCM	18 %	20 %	28 %

5 | Summary and Discussion

This thesis proposes two automatic exposure approaches to reduce the patient's radiation risk in terms of effective dose, which is a weighted sum of organ doses. The first approach is a combined tube current and tube voltage modulation. The second approach is the optimization of the tube start angle. This chapter discusses both approaches, including the potential effective dose reductions as well as limitations of the studies, prerequisites for a possible translation to clinical practice, and future research questions.

5.1 Tube Current and Tube Voltage Modulation

Tube current modulation (TCM) techniques reducing the tube current time product of the scan [10], [11], here called mAsTCM, are already in clinical practice. Furthermore, TCM approaches minimizing the effective dose as a risk measure for the patient have been proposed [15], [16]; here, such an approach is called riskTCM in the following according to reference [15]. However, automatic tube voltage selection (ATVS) systems on clinical scanners select a constant voltage. Since the optimal voltage depends on the patient attenuation which can vary between different projections, the effective dose might be decreased by an additional tube voltage modulation that, similar to TCM, selects a tube voltage per projection angle.

For the study of a tube voltage modulation in addition to a TCM, scans with and without iodine contrast were considered. For the simulation of unenhanced scans, tube current and tube voltage curves were optimized to reduce the dose-weighted noise in simulated circular scans. The modulation resulting from the simultaneous optimization of tube current and tube voltage was named risk–minimizing tube current and tube voltage modulation (riskTCTVM). The dose-weighted noise refers here to the product of average noise across the patient's body and the square root of the effective dose. Since the effective dose is proportional to the tube current and the noise is antiproportional to the square root of the tube current, this definition of the dose-weighted noise is invariant to scalings of the tube current. The optimization of the dose-weighted noise can be viewed as a dose minimization at constant noise or a noise minimization at constant effective dose. The effective dose values at constant noise were compared to riskTCM and mAsTCM at constant voltages from 40 kV to 150 kV in steps of 5 kV.

For the study of iodine-enhanced scans, an iodine disk was artificially inserted into CT images in the isocenter and the dose-weighted contrast-to-noise ratio (CNRD) was

optimized. The combined tube current and tube voltage optimizations were performed for different voltage ranges with a maximum voltage of 150 kV and varying minimum voltages of 40 kV, 50 kV, 60 kV, and 70 kV. The effective dose values of riskTCTVM were compared at constant contrast-to-noise ratio (CNR) to riskTCM and mAsTCM.

Potential Effective Dose Reduction

For unenhanced scans, the additional tube voltage modulation riskTCTVM showed reductions of the effective dose of less than 1 % compared to riskTCM. For scans with iodine contrast, the potential effective dose benefit highly depends on the lowest available voltage and the anatomy. Generally, the effective dose benefit increases with the availability of low tube voltages down to 50 kV. A minimum voltage of 40 kV showed only slight further benefits of up to 3 % at maximum. Regarding the anatomy, the effective dose benefits of riskTCTVM compared to riskTCM show a correlation with the ratio of the maximum to the minimum value of the maximum water intersection length per projection angle; this ratio of the water intersection lengths relates to the eccentricity of the anatomy. With increasing eccentricity of the anatomy, the effective dose benefits increase. For eccentric anatomies in the shoulder and the pelvis, effective dose benefits compared to riskTCM of up to 35 % were found for a lowest allowed voltage of 50 kV. The average effective dose reduction for this voltage range were 28 % for the shoulder, 16 % for the pelvis, 11 % for the abdomen, and 7 % for the thorax. For a minimum voltage of 70 kV, which is the lowest voltage available in current clinical practice, the effective dose benefits of riskTCTVM for the shoulder were on average 14 % and for the other body regions the average values were below 6 %.

Maximum Tube Current

All optimizations were performed without a constraint on the tube current to study the maximum possible effective dose reductions. However, tube current limits can be exceeded for low voltages in clinical practice. For anatomies with high attenuation such as the shoulder, X-ray tubes with a high tube power are necessary. Currently, X-ray tubes with a maximum tube current of 1300 mA at 70 kV are available [3]. With such X-ray tubes, CT scans at 70 kV can be performed for head and neck scans including the shoulder [72]–[74].

To assess how realistic the realization of the optimized curves with currently available X-ray tubes is, the maximum requested tube current of the optimized curves was compared to the maximum tube current of mAsTCM at 70 kV. The maximum requested tube current of riskTCM at 70 kV was always higher than for mAsTCM including cases for which the maximum tube current was more than twice as high. The higher maximum tube current can be explained by the fact that riskTCM turns the tube current to zero for tube positions with a high effective dose; in some cases, this angular range is close to 180°. Also for riskTCTVM with a minimum voltage of 70 kV, the maximum requested tube current was more than twice as high as for mAsTCM for several anatomies. However, for eccentric anatomies in the shoulder and the pelvis, the maximum requested

tube current was lower. This decrease in maximum tube current is possible due to the increase in tube voltage for lateral projections which is especially beneficial for eccentric anatomies such as the shoulder. For the shoulder and a lowest allowed voltage of 70 kV, the maximum requested tube current by riskTCTVM was on average 15 % lower with an effective dose decrease of about 50 % compared to mAsTCM at 70 kV. For a lowest allowed voltage of 60 kV, the maximum requested tube current was on average 15 % higher compared to mAsTCM at 70 kV.

For riskTCM instead, the maximum requested tube current for the shoulder was on average 50 % higher for a lowest allowed voltage of 70 kV and more than twice as high for a lowest allowed voltage of 60 kV compared to mAsTCM. Thus, while the application of riskTCM in the shoulder is questionable for these voltages, the application of riskTCTVM seems at least for a lowest allowed voltage of 70 kV feasible regarding tube current constraints.

Limitations

The study was a pure simulation study for a first assessment of the potential dose benefits of a tube voltage modulation. Some simplifications were made including the simulation of contrast agent which was mimicked by placing an iodine disk of constant density in the isocenter; this insertion could serve as a simple model of a blood vessel filled with iodine and caused the general shift to lower voltages by the optimization when including contrast in the optimization. Future studies should include variations of the inserted contrast density, size, and location to determine the potential relevance of these parameters for the optimized tube current and tube voltage curves and the corresponding dose benefits.

Furthermore, the patient cohort should be considered when interpreting the results. The study included patients of different sex, e.g. three female and three male patients, and of different patient diameter. The study thus showed the benefit of riskTCTVM for a range of patients differing in relevant characteristics for risk reduction. For statements about the general population or a specific patient population, however, a higher number of patients with a representative composition as in the population of interest should be studied. Nevertheless, the observed correlation of the effective dose benefits with the eccentricity of the anatomy could indicate the expected dose benefits for other patients. Especially for very eccentric anatomies such as the shoulder region, riskTCTVM showed promising decreases in effective dose and maximum tube current for all patients.

Image Quality Considerations

As in reference [46], the CNRD was optimized which relates to a CNR optimization at a constant dose. The authors of reference [42] instead argued that CNR should be optimized under a noise constraint; otherwise, noise could increase as much as contrast increases which could be inappropriate for certain diagnostic tasks for which structures with little enhancement are also relevant for the diagnosis [42]. Also for ATVS systems on clinical scanners, the selection of the diagnostic application is common

which influences the adjustment of the tube current level [43] and thus the importance given to the contrast enhancement at lower voltages.

Furthermore, it is important to note that a patient-specific tube voltage modulation complicates the interpretation of the CT value of the contrast and its relation to the contrast density. Several higher-order beam hardening methods which consider besides water another material such as bone and iodine are already available for constant voltages [1]. For better interpretation of the contrast, such higher-order beam hardening corrections should be adapted to consider the change in tube voltage between different projections used in the acquisition. Without a higher-order beam hardening correction, the here proposed tube voltage modulation should only be considered for diagnostic applications in which solely the visualization of structures matters and the numerical value of the enhancement is not of interest.

Besides the importance given to the contrast, the noise metric to optimize could also be discussed. Here, the mean noise across the patient was optimized as proposed in reference [15]. The authors of reference [16] instead argued that the maximum noise should be minimized to establish a minimum image quality across the whole image. A simulation study regarding fluence field modulation with control of every ray indicated that minimizing the mean pixel variance yields different results from minimizing the maximum pixel variance [75]. In the future, the effect of different noise objectives on the optimized riskTCTVM curves and on the effective dose could be investigated. It should also be noted that the riskTCTVM optimization framework allows for a user-defined mask with varying weights given to the noise of different image pixels. These weights for the noise can be used for example to enforce a low noise in image regions of special diagnostic interest.

Finally, the image quality estimated in the simulations should ideally be verified with measurements on clinical scanners; this could also include the subjective image quality assessment by radiologists. However, the employment of riskTCTVM on a clinical scanner is currently not possible as discussed in the following section.

Prerequisites for a Translation to Clinical Practice

There are several challenges to address before the optimized riskTCTVM curves can be tested on a clinical scanner. First of all, clinical scanners give the user limited control over the tube current and tube voltage; however, a control on a per-view basis would be necessary which allows the user to specify tube current and tube voltage values as a function of tube position. Hence, the cooperation of vendors of CT systems is required here. If such a control was made available by vendors, for example in a research mode, the realization of the optimized tube current and tube voltage curves by the X-ray tube should be verified.

For the tube current, a potential issue might be the tube current inertia which was neglected in the present study. However, quite steep changes in the tube current are already implemented for example in the organ-specific tube current modulation (osTCM) XCare by Siemens [76]. The shape of the XCare tube current curve is similar to a step function that decreases the tube current for anterior-posterior projections to

reduce the dose to sensitive organs at the anterior of the patient such as the breast in particular. The decrease and increase of the tube current by a factor of five is realized in an interval of 20°. Furthermore, it is not clear whether the tube current could be switched off completely for some angular range as proposed by the optimized curves. It might therefore be necessary to include a lower limit on the tube current for the application on a clinical scanner. Similarly, also an upper limit of the tube current should be included to prevent the violation of tube current limits on available scanners. As discussed, all riskTCM and riskTCTVM optimizations were performed without a constraint on the tube current. The optimized curves thus show the maximum possible effective dose reductions by riskTCM and riskTCTVM. While riskTCTVM with a lowest voltage of 70 kV could lower the maximum requested tube current in the shoulder region compared to mAsTCM at 70 kV, the maximum requested tube current was higher for other anatomies and lower tube voltages. The maximum requested tube current by riskTCM was always higher compared to mAsTCM. The possible dose reductions of riskTCM and riskTCTVM subject to a tube current limit would therefore be of interest. The inclusion of an upper bound of the tube current also implies that the desired image quality has to be known for the optimization process.

Similar to the tube current, also the feasibility of the tube voltage control has to be verified. In most CT systems, the voltage remains constant throughout CT scans. However, CT systems with fast kV-switching are available. These systems switch between two different voltages in less than a millisecond for the acquisition in dual-energy CT [77]. The availability of such fast kV-switching techniques therefore seems promising for the realization of continuous voltage changes at a slower rate as proposed by the riskTCTVM optimization. However, the remaining challenge for tube voltage modulation is that calibration for every voltage has to be available to perform water precorrection. Here, the application of proposed calibration techniques for systems with tube voltage modulation [51], [52] could be considered.

Moreover, the study was limited to circular scans. As spiral scans are the common tube trajectory in clinical practice, an extension to spiral scans is necessary. As described and realized in reference [40] for riskTCM, the extension to spiral scans could be achieved by computing tube current and tube voltage curves for tightly spaced circular scans from which spiral trajectories can be obtained by interpolation. However, it should be noted that the proposed optimization framework for riskTCM and riskTCTVM assumes a complementary ray for every ray which restricts the pitch value of a spiral scan to pitch values below about 0.6 [40]. The presence and the optimal weighting of complementary rays by their variance is necessary for an optimal reduction of the effective dose as switching off the tube current for views with a particularly high effective dose can be compensated by the respective complementary ray. Pitch values above 0.6 are therefore not impossible but reduce the effective dose reduction potential of riskTCM and riskTCTVM.

Furthermore, as also discussed for riskTCM [15], [40], a reconstruction of the patient volume prior to the CT scan is necessary for the estimation of noise and contrast; moreover, an organ segmentation and a dose estimation for the determination of the effective dose per view angle are needed. The reconstruction of the patient volume could

be obtained by an estimation based on topograms [78]–[81]. Another option could be a low-dose 3D scout scan [82], [83]. It should be noted here that the reconstructed patient volume should ideally cover the whole body to accurately calculate the organ mass of all organs. The patient models used in this thesis are based on whole-body scans that cover the patients from the head to the knee (compare figure 3.1). Therefore, the organ doses of organs spanning across the whole body as the skin, the bone surface, the red bone marrow, and the remainder were underestimated resulting in an overestimation of the corresponding organ doses [40]. However, as the contribution of these organs is rather small compared to organs causing major peaks in the effective dose curve (compare figure 4.5) which dominate the riskTCM and riskTCTVM optimization, the overestimation of those minorly contributing organ doses was neglected as in reference [40]. If however the patient volume captured by a topogram or a scout scan is small or the scan range is adjacent to a sensitive organ, the unknown body parts should not be neglected. Approaches to estimate the unknown body parts might include a comparison of the patient in question to a patient or phantom atlas [84] or an estimation by deep learning models. Also, information from 3D cameras, if available, could support the estimation [85]. For a given patient volume reconstruction, the organ segmentation could possibly be retrieved with deep learning models [86], [87]. Finally, a fast dose estimation is necessary to estimate the dose deposition beforehand. This could also be based on deep learning as the deep dose estimation [88] employed for the study of riskTCM [15] that was trained to reproduce Monte Carlo simulations. Another option could be fast analytical dose estimations combining first-order estimates with convolution kernels to approximate higher-order interactions [89].

Future Research and Extensions

As discussed in the previous section, the current workflow of riskTCM and riskTCTVM is based on a CT volume reconstruction of the patient prior to the scan as well as a dose estimation and an organ segmentation to retrieve organ dose values. Other studies instead aimed at estimating organ doses, organ noise, and TCM tailored to specific organs directly from topograms [90]–[92]. Future studies thus could investigate which information required for the creation of riskTCTVM curves could potentially be directly derived from topograms and what accuracy is necessary to achieve the best optimization result for the patient. One study of riskTCM with age- and sex-specific risk measures, for example, suggested that changes in the risk curve do not necessarily cause considerable changes of the optimized tube current curves if the changes are only quantitative and not of qualitative nature [93], [94], i.e. for example peaks in the risk curve caused by certain sensitive organs might change their height but the order does not change, i.e. the highest peak stays the highest. Therefore, it might be insightful to study which information is actually necessary to create per-view radiation risk data that lead to the most risk-beneficial modulation curves. In this regard, other risk measures could also be investigated. The effective dose was chosen here as it is a widely used metric [95]. However, the effective dose was initially not intended for the risk assessment for individual patients and more patient-specific risk measures have been proposed [95].

Discussions on the most appropriate risk measure for individual protocol optimization are therefore relevant to follow for future developments of riskTCTVM whose workflow can easily be changed to consider another risk measure.

Another parameter that influences the X-ray spectrum is the prefilter thickness. A systematic study of the optimal combination of tube voltage and prefilter settings suggested that an optimal choice could reduce the CT dose index (CTDI) dose substantially compared to standard settings [96]. Therefore, an extension of riskTCTVM could be to include a prefilter thickness modulation to further decrease the radiation risk. Setups for the realization of a variable filter during CT acquisition have already been proposed [97], [98]. Again, tube current limits are here the restricting factor and should be included in the optimization. Ideally, the prefilter thickness would be so thick that the emitted X-rays are nearly monochromatic. Therefore, it might be insightful to perform an optimization with monochromatic X-rays to obtain an upper limit of the potential patient decrease in effective dose by a combined tube current, tube voltage, and prefilter thickness modulation that is subject to a tube current limit.

5.2 Spiral Start Angle Optimization

For the study of the start angle optimization, Monte Carlo dose simulations were performed for tube positions covering the thorax of three male and three female patients. The thorax region was chosen as short scan times and thus high pitch values are particularly relevant in this body region due to breathing and heart motion. The simulations were performed for collimations of 40 mm, 60 mm and 80 mm. From the simulated tube positions, spiral trajectories with pitch values from 0.5 to 1.5 for single source CT (SSCT) and from 0.5 to 3 for dual source CT (DSCT) were created for different start angles. For every pitch value, the effective dose of the best start angle, that is the angle resulting in the lowest effective dose was compared to the effective dose of the worst start angle and to the average effective dose over all start angles. The latter can be considered the expectation value for current clinical practice in which the tube start angle can be considered a random scan parameter. Scans with mAsTCM and without TCM, i.e. with a constant tube current, were studied.

Potential Effective Dose Reduction

The effective dose reductions by a start angle selection increase with increasing collimation width. Also with increasing pitch value, the effective dose reductions tend to increase. For scans with mAsTCM, only minor differences in effective dose reduction to scans without TCM were observed; yet, the average effective dose reductions tend to be slightly higher. For a collimation of $C = 40\,\text{mm}$, the possible dose reductions compared to the mean effective dose value stay below 5 % for SSCT. For DSCT and TCM with a pitch value of 3, reductions in effective dose were about 10 % compared to the mean value and 18 % to the worst start angle. The highest potential for reduction of effective dose was found for a pitch of three for the case of DSCT with TCM and a collimation of $C = 80\,\text{mm}$. For this scan scenario, effective dose reductions by the best start angle

were about 16 % to the mean value and 28 % to the worst start angle.

These findings add several contributions to the results of previous studies addressing the dose reduction potential for single organs by a control of the tube start angle [17], [18]. First of all, the results of the here presented study indicate that not only single organs but also the effective dose, a weighting of several organ doses, can benefit from a control of the start angle. Furthermore, also scans with TCM were considered. Moreover, the study of collimations up to 80 mm confirmed the higher dose reduction potential for higher collimation widths assumed in reference [18]. The maximum collimation considered by the authors of reference [18] was $C = 40\,\text{mm}$ and they concluded for this collimation that for adult patients, except for the eye lenses, potential organ dose reductions are rather small [18]. Finally, the inclusion of DSCT allowed to study pitch values up to three which show a higher dose reduction potential than the maximum pitch of 1.5 for SSCT.

Limitations

The study was a pure simulation study. Furthermore, it should be considered that only six patients were studied; these were the same patients as for the study of the tube voltage modulation. As discussed, the average effective dose reduction values could differ for the general population and the spread of the values could be higher. However, the studied patients exhibit differences in some relevant aspects. The studied patients include male as well as female patients and the patients show different diameters (compare figure 3.1). Figure 4.4 also shows that the organ dose magnitude and the angular and longitudinal extent of highly dose-contributing organs such as the breast and the stomach differ between the studied patients (see also figure 4.5 for a representative decomposition of the effective dose into organ doses). Considering these differences in sex and anatomy, the variations between the patients appear for most scan scenarios rather small: for the case of DSCT with mAsTCM and collimation of 80 mm for example which exhibits the highest effect with an average reduction in effective dose of the best start angle of 16 %, the spread between the patients only ranges from 13 % to 18 % reduction in effective dose (compare figure 4.7). Therefore, despite the small number of patients, the results might give a decent indication of the possible range of dose reduction values to expect from selecting the best tube start angle and show that this is a beneficial approach for various patients.

Image Quality Considerations

As well as for the tube voltage modulation, the image quality should be discussed. However, image quality changes only if the acquisition of the data or the image reconstruction is changed. In current clinical practice, the start angle is not controlled and is determined by the position of the rotating tube at the time of the scan start. Hence, the tube start angle can be considered a random parameter of the acquisition process. As this random choice is accepted by radiologists, the impact of the tube start angle on image quality, if any, can be considered negligible. Therefore, the tube start angle

can be selected without image quality concerns as this selection does not result in a new acquisition process but is just a selection of one of the accepted acquisitions which could have been chosen randomly otherwise. In other words, the current random choice of the tube start angle is simply replaced by an effective dose-optimized choice while all other parameters of the scan protocol and image reconstruction remain unchanged. A control of the start angle could therefore be introduced into clinical practice without image quality concerns.

Prerequisites for a Translation to Clinical Practice

In part, the same prerequisites for the tube voltage modulation apply to the employment of a start angle selection in clinical practice. These prerequisites include the per-view risk data which is currently retrieved from a patient volume reconstruction, an organ segmentation, and a dose estimation. Once per-view risk data are available, however, the control of the tube start angle in clinical practice seems feasible. Only for CT scans, for which the exact timing is crucial such as cardiac gated scans, it might not be possible to wait for the X-ray tube to be at the right angle to start.

Future Research

Future work could include besides a variable start angle a variable pitch throughout the scan, i.e. the pitch could be adapted depending on the length of the organs and the distance between them in the longitudinal direction. This adjustment of the pitch offers more flexibility and might further decrease the dose.

Moreover, the application of a start angle optimization for children could also be studied. Due to the smaller size of the organs, higher effective dose reductions might be possible for children compared to adults at the same pitch value.

Furthermore, for pitch values above 0.6, for which a complementary ray is not present for every ray which limits the effective dose reduction potential of riskTCTVM, it might be beneficial to combine riskTCTVM with a start angle optimization.

6 | Conclusions

This thesis proposes two automatic exposure approaches to reduce the patient's radiation risk in terms of the effective dose. Both proposed approaches offer promising reductions in effective dose for certain scenarios.

The first approach is a combined tube current and tube voltage modulation called riskTCTVM that was studied for circular scans. For unenhanced scans, riskTCTVM yields negligible dose benefits compared to a pure risk-minimizing tube current modulation (riskTCM). For iodine-enhanced scans, the effective dose benefits increase with the availability of low tube voltages and the eccentricity of the studied anatomy. To exploit the full potential of reducing the effective dose for iodine-enhanced scans, voltages down to 50 kV at sufficient tube power are required. For this scenario, all studied anatomical regions from the shoulder to the pelvis benefit from riskTCTVM. However, the lowest voltage currently available at clinical scanners is 70 kV. Nonetheless, also for a lowest voltage 70 kV, riskTCTVM shows promising results for eccentric anatomies in the shoulder and the pelvis. For these anatomies and for a lowest voltage of 70 kV, riskTCTVM can lower tube current demands compared to conventional mAs-minimizing TCM at 70 kV while substantially reducing the effective dose.

The second proposed approach is an optimal selection of the tube start angle. In current clinical practice, the tube start angle can be considered a random scan parameter. However, especially for high spiral pitch values and high collimation widths, an optimal selection of the tube start angle yields considerable reductions of the effective dose compared to the average over all start angles.

In conclusion, the use of riskTCTVM seems desirable for iodine-enhanced scans with low spiral pitch values and the use of a start angle selection seems desirable for spiral scans with high pitch values. In the future, both approaches could be combined to possibly increase the potential to reduce the effective dose for all pitch values.

List of Publications

During the time as a PhD student at the German Cancer Research Center (DKFZ) and Heidelberg University, I contributed to the following publications:

Published and submitted journal articles with direct reference to the dissertation

[1] **E. Baader** and M. Kachelrieß, "Risk-minimizing tube current and tube voltage modulation for CT: A simulation study," *Submitted to Med. Phys.*, 2024.

[2] **E. Baader**, L. Klein, J. Maier, S. Sawall, and M. Kachelrieß, "Patient radiation risk reduction by controlling the tube start angle in single and dual source spiral CT scans: A simulation study," *Med. Phys.*, volume 51, number 10, pages 7080–7092, 2024.

These articles are used in the dissertation.

Conference contributions with direct reference to the dissertation

[1] **E. Baader**, L. Klein, S. Sawall, J. Maier, and M. Kachelrieß, "CT tube current and tube voltage modulation to minimize the patient's radiation risk," *Insights into Imaging, ECR Book of Abstracts*, volume 14, number Supp. 4, 2023.

[2] **E. Baader**, L. Klein, J. Maier, S. Sawall, and M. Kachelrieß, "Impact of the tube start angle on patient dose in single and dual source spiral CT," *Program of the 109th Scientific Assembly and Annual Meeting of the RSNA*, R5A–SPPH–8, 2023.

[3] **E. Baader** and M. Kachelrieß, "Tube voltage modulation for contrast-enhanced CT scans," *Conference Record of the 8th International Conference on Image Formation in X–Ray Computed Tomography*, volume 8, pages 198–200, 2024.

These conference contributions contain preliminary work and results leading to the journal articles with direct reference.

Journal articles without direct reference to the dissertation

[1] C. Liu, L. Klein, Y. Huang, **E. Baader**, M. Lell, M. Kachelrieß, and A. Maier, "Two-view topogram-based anatomy-guided CT reconstruction for prospective risk minimization," *Scientific Reports*, volume 14, number 1, page 9373, 2024.

[2] S. Sawall, **E. Baader**, J. Wolf, J. Maier, H.-P. Schlemmer, S. O. Schönberg, I. Sechopoulos, and M. Kachelrieß, "Image quality of opportunistic breast examinations in photon-counting computed tomography: A phantom study," *Physica Medica*, volume 122, page 103 378, 2024.

[3] S. Sawall, **E. Baader**, P. Trapp, and M. Kachelrieß, "CT material decomposition with contrast agents: Single or multiple spectral photon-counting CT scans? A simulation study," *Med. Phys.*, 2025.

Reference [1] is cited in the dissertation.

Conference contributions without direct reference to the dissertation

[1] S. Sawall, S. Lehr, **E. Baader**, L. Rotkopf, J. Maier, H.-P. Schlemmer, S Schönberg, I. Sechopoulos, and M. Kachelrieß, "Dedicated imaging of the breast with a clinical photon-counting CT system: A phantom study," *Program of the 108th Scientific Assembly and Annual Meeting of the RSNA*, SSPH07–4, 2022.

[2] L. Klein, **E. Baader**, A. Byl, C. Liu, S. Sawall, A. Maier, M. M. Lell, J. Maier, and M. Kachelrieß, "Potential CT radiation dose reduction to the female breast by a novel risk-minimizing tube current modulation," *Program of the 108th Scientific Assembly and Annual Meeting of the RSNA*, R2–SPPH–8, 2022.

[3] S. Sawall, **E. Baader**, and M. Kachelrieß, "Decomposition of CT contrast agents: Single or multiple photon counting CT scans? Single or dual source PCCT?" *Program of the 109th Scientific Assembly and Annual Meeting of the RSNA*, M2–SPPH–6, 2023.

[4] S. Sawall, **E. Baader**, and M. Kachelrieß, "Optimal scan strategies for material decomposition in photon-counting CT with multiple contrast agents," *66th Annual Meeting of the AAPM*, 2024.

[5] S. Klubertz, **E. Baader**, and M. Kachelrieß, "Do we need age- and sex-dependent organ weights for the risk-specific tube current modulation (riskTCM) in diagnostic CT?" *Abstracts of the 5th European Congress of Medical Physics in Physica Medica*, volume 125, page 103 537, 2024.

Reference [5] is cited in the dissertation.

Note on the list of publications

Reference [1] of the journal articles with direct reference to the dissertation was published under a CC BY 4.0 license (https://creativecommons.org/licenses/by/4.0/) after the submission of the dissertation. Chapter 3 reproduces parts of the manuscript before final revision and acceptance for publication. These parts include a shortened version of the introduction, the materials and methods section, and the results section. Chapter 5 contains recproduced parts of the discussion of the manuscript before final revision and acceptance for publication.

The published journal article should be cited as follows:

E. Baader and M. Kachelrieß, "Risk-minimizing tube current and tube voltage modulation for CT: A simulation study," *Med. Phys.*, volume 52, number 8, e18047, 2025.

Bibliography

[1] M. Kachelrieß, "Computertomographie," in *Medizinische Physik: Grundlagen – Bildgebung – Therapie – Technik*, W. Schlegel, C. P. Karger, and O. Jäkel, Eds. Berlin, Heidelberg: Springer Berlin Heidelberg, 2018, pages 153–203.

[2] M. M. Lell, J. E. Wildberger, H. Alkadhi, J. Damilakis, and M. Kachelrieß, "Evolution in computed tomography: The battle for speed and dose," *Investigative Radiology*, volume 50, number 9, pages 629–644, 2015.

[3] M. Lell and M. Kachelrieß, "Computed tomography 2.0: New detector technology, AI, and other developments," *Investigative Radiology*, volume 58, number 8, pages 587–601, 2023.

[4] A. A. Schegerer, H.-D. Nagel, G. Stamm, G. Adam, and G. Brix, "Current CT practice in Germany: Results and implications of a nationwide survey," *European Journal of Radiology*, volume 90, pages 114–128, 2017.

[5] United Nations scientific committee on the effects of atomic radiation and others, "Sources and effects of ionizing radiation, United Nations scientific committee on the effects of atomic radiation (UNSCEAR) 2008 report, volume I: Report to the general assembly, with scientific annexes A and B–sources," 2010.

[6] E. Ron, "Cancer risks from medical radiation," *Health Physics*, volume 85, number 1, pages 47–59, 2003.

[7] A. B. de Gonzalez and S. Darby, "Risk of cancer from diagnostic x-rays: Estimates for the UK and 14 other countries," *The Lancet*, volume 363, number 9406, pages 345–351, 2004.

[8] ICRP 2007, "The 2007 recommendations of the International Commission on Radiological Protection," *ICRP Publication 103. Ann. ICRP*, volume 37, pages 2–4, 2007.

[9] K. J. Strauss and S. C. Kaste, "The ALARA (as low as reasonably achievable) concept in pediatric interventional and fluoroscopic imaging: Striving to keep radiation doses as low as possible during fluoroscopy of pediatric patients—a white paper executive summary," *Radiology*, volume 240, number 3, pages 621–622, 2006.

[10] M. Gies, W. A. Kalender, H. Wolf, C. Suess, and M. T. Madsen, "Dose reduction in CT by anatomically adapted tube current modulation. I. Simulation studies," *Med. Phys.*, volume 26, number 11, pages 2235–2247, 1999.

[11] W. A. Kalender, H. Wolf, and C. Suess, "Dose reduction in CT by anatomically adapted tube current modulation. II. Phantom measurements," *Med. Phys.*, volume 26, number 11, pages 2248–2253, 1999.

[12] A. Euler, Z. Szucs-Farkas, A. L. Falkowski, N. Kawel-Böhm, L. D'Errico, S. Kopp, J. Bremerich, and T. Niemann, "Organ-based tube current modulation in a clinical context: Dose reduction may be largely overestimated in breast tissue," *European Radiology*, volume 26, pages 2656–2662, 2016.

[13] J. Ota, H. Yokota, H. Takishima, A. Takada, R. Irie, Y. Suzuki, T. Nagashima, T. Horikoshi, K. Chida, Y. Masuda, and T. Uno, "Breast exposure reduction using organ-effective modulation on chest CT in asian women," *European Journal of Radiology*, volume 119, page 108 651, 2019.

[14] A. E. Papadakis and J. Damilakis, "Evaluation of an organ-based tube current modulation tool in pediatric CT examinations," *European Radiology*, volume 30, pages 5728–5737, 2020.

[15] L. Klein, C. Liu, J. Steidel, L. Enzmann, M. Knaup, S. Sawall, A. Maier, M. Lell, J. Maier, and M. Kachelrieß, "Patient-specific radiation risk-based tube current modulation for diagnostic CT," *Med. Phys.*, volume 49, number 7, pages 4391–4403, 2022.

[16] J. Sperl, D. Beque, B. Claus, B. De Man, B. Senzig, and M. Brokate, "Computer-assisted scan protocol and reconstruction (CASPAR)—reduction of image noise and patient dose," *IEEE Transactions on Medical Imaging*, volume 29, number 3, pages 724–732, 2010.

[17] J. F. Winslow, C. J. Tien, and D. E. Hintenlang, "Organ dose and inherent uncertainty in helical CT dosimetry due to quasiperiodic dose distributions," *Med. Phys.*, volume 38, number 6, pages 3177–3185, 2011.

[18] D. Zhang, M. Zankl, J. J. DeMarco, C. H. Cagnon, E. Angel, A. C. Turner, and M. F. McNitt-Gray, "Reducing radiation dose to selected organs by selecting the tube start angle in MDCT helical scans: A Monte Carlo based study," *Med. Phys.*, volume 36, number 12, pages 5654–5664, 2009.

[19] Beer, "Bestimmung der Absorption des rothen Lichts in farbigen Flüssigkeiten," *Annalen der Physik*, volume 162, number 5, pages 78–88, 1852.

[20] J. H. Lambert, *Photometria sive de mensura et gradibus luminis, colorum et umbrae*. sumptibus vidvae E. Klett, typis CP Detleffsen, 1760.

[21] P. Bouguer, *Essai d'optique sur la gradation de la lumière*. Claude Jombert, 1729.

[22] S. Greilich and J.-M. Osinga-Blättermann, "Strahlenphysik," in *Medizinische Physik: Grundlagen – Bildgebung – Therapie – Technik*, W. Schlegel, C. P. Karger, and O. Jäkel, Eds. Berlin, Heidelberg: Springer Berlin Heidelberg, 2018, pages 3–35.

[23] D. E. Cullen, J. H. Hubbell, and L. Kissel, "EPDL97: The evaluated photo data library97 version," Lawrence Livermore National Lab. (LLNL), Livermore, CA (United States), Tech. Rep., 1997.

[24] ICRU, II, "Tissue substitutes in radiation dosimetry and measurement," *International Commission on Radiation Units and Measurements*, 1989.

[25] R. Ringler, "Physikalisch-technische Grundlagen der Röntgendiagnostik," in *Medizinische Physik: Grundlagen – Bildgebung – Therapie – Technik*, W. Schlegel, C. P. Karger, and O. Jäkel, Eds. Berlin, Heidelberg: Springer Berlin Heidelberg, 2018, pages 123–138.

[26] D. M. Tucker, G. T. Barnes, and D. P. Chakraborty, "Semiempirical model for generating tungsten target X–ray spectra," *Med. Phys.*, volume 18, number 3, pages 211–218, 1991.

[27] P. D. Deak, O. Langner, M. Lell, and W. A. Kalender, "Effects of adaptive section collimation on patient radiation dose in multisection spiral CT," *Radiology*, volume 252, number 1, pages 140–147, 2009.

[28] K. Rajendran, M. Petersilka, A. Henning, E. R. Shanblatt, B. Schmidt, T. G. Flohr, A. Ferrero, F. Baffour, F. E. Diehn, L. Yu, P. Rajiah, J. G. Fletcher, S. Leng, and C. H. McCollough, "First clinical photon-counting detector CT system: Technical evaluation," *Radiology*, volume 303, number 1, pages 130–138, 2022.

[29] C. H. McCollough, K. Rajendran, F. I. Baffour, F. E. Diehn, A. Ferrero, K. N. Glazebrook, K. K. Horst, T. F. Johnson, S. Leng, A. Mileto, P. S. Rajiah, B. Schmidt, L. Yu, T. G. Flohr, and J. G. Fletcher, "Clinical applications of photon counting detector CT," *European Radiology*, volume 33, number 8, pages 5309–5320, 2023.

[30] K. Rajendran, B. A. Voss, W. Zhou, S. Tao, D. R. DeLone, J. I. Lane, J. M. Weaver, M. L. Carlson, J. G. Fletcher, C. H. McCollough, and S. Leng, "Dose reduction for sinus and temporal bone imaging using photon-counting detector CT with an additional tin filter," *Investigative Radiology*, volume 55, number 2, pages 91–100, 2020.

[31] L. Klein, S. Dorn, C. Amato, S. Heinze, M. Uhrig, H.-P. Schlemmer, M. Kachelrieß, and S. Sawall, "Effects of detector sampling on noise reduction in clinical photon-counting whole-body computed tomography," *Investigative Radiology*, volume 55, number 2, pages 111–119, 2020.

[32] M. Kachelrieß, "Reduktion von Metallartefakten in der Röntgen-Computer-Tomographie," Ph.D. dissertation, Friedrich-Alexander-Universität Erlangen-Nürnberg, 1998.

[33] J. Radon, "Über die Bestimmung von Funktionen durch ihre Integralwerte längs gewisser Mannigfaltigkeiten," *Akad. Wiss.*, volume 69, pages 262–277, 1917.

[34] G. Major, "Strahlenschutz," in *Medizinische Physik: Grundlagen – Bildgebung – Therapie – Technik*, W. Schlegel, C. P. Karger, and O. Jäkel, Eds. Berlin, Heidelberg: Springer Berlin Heidelberg, 2018, pages 89–120.

[35] H. Krieger, "Strahlenbiologie der Zelle," in *Grundlagen der Strahlungsphysik und des Strahlenschutzes*. Berlin, Heidelberg: Springer Berlin Heidelberg, 2023, pages 453–490.

[36] H. Krieger, "Risiken und Wirkungen ionisierender Strahlung," in *Grundlagen der Strahlungsphysik und des Strahlenschutzes*. Berlin, Heidelberg: Springer Berlin Heidelberg, 2023, pages 533–578.

[37] M. Doss, M. P. Little, and C. G. Orton, "Point/counterpoint: Low-dose radiation is beneficial, not harmful," *Med. Phys.*, volume 41, number 7, page 070 601, 2014.

[38] ICRP 1977, "Recommendations of the international commission on radiological protection.," *ICRP Publication 26. Ann. ICRP 1 (3)*, 1977.

[39] K. Treb and K. Li, "Accuracy of weighted CTDI in estimating average dose delivered to CTDI phantoms: An experimental study," *Med. Phys.*, volume 47, number 12, pages 6484–6499, 2020.

[40] L. V. Klein, "Patient risk-minimizing tube current modulation in x-ray computed tomography," Ph.D. dissertation, Heidelberg University, 2023.

[41] P Spanne, "X-ray energy optimisation in computed microtomography," *Phys. Med. Biol.*, volume 34, number 6, pages 679–690, 1989.

[42] L. Yu, H. Li, J. G. Fletcher, and C. H. McCollough, "Automatic selection of tube potential for radiation dose reduction in CT: A general strategy," *Med. Phys.*, volume 37, number 1, pages 234–243, 2010.

[43] A. Winklehner, R. Goetti, S. Baumueller, C. Karlo, B. Schmidt, R. Raupach, T. Flohr, T. Frauenfelder, and H. Alkadhi, "Automated attenuation-based tube potential selection for thoracoabdominal computed tomography angiography: Improved dose effectiveness," *Investigative Radiology*, volume 46, number 12, pages 767–773, 2011.

[44] L. Grodzins, "Optimum energies for x–ray transmission tomography of small samples," *Nuclear Instruments and Methods*, volume 206, pages 541–545, 1983.

[45] F. A. Dilmanian, X. Y. Wu, E. C. Parsons, B Ren, J Kress, T. M. Button, L. D. Chapman, J. A. Coderre, F Giron, D Greenberg, D. J. Krus, Z Liang, S Marcovici, M. J. Petersen, C. T. Roque, M Shleifer, D. N. Slatkin, W. C. Thomlinson, K Yamamoto, and Z Zhong, "Single- and dual-energy CT with monochromatic synchrotron x-rays," *Phys. Med. Biol.*, volume 42, number 2, pages 371–387, 1997.

[46] W. A. Kalender, P. Deak, M. Kellermeier, M. Van Straten, and S. V. Vollmar, "Application- and patient size-dependent optimization of x-ray spectra for CT," *Med. Phys.*, volume 36, number 3, pages 993–1007, 2009.

[47] H. W. Goo and D. S. Suh, "The influences of tube voltage and scan direction on combined tube current modulation: A phantom study," *Pediatric Radiology*, volume 36, pages 833–840, 2006.

[48] P. Chen and Y. Han, "Varying-energy CT imaging method based on EM-TV," *Measurement Science and Technology*, volume 27, number 11, page 114 004, 2016.

[49] P. Chen, S. Yang, Y. Han, J. Pan, and Y. Li, "High-dynamic-range X-ray CT imaging method based on energy self-adaptation between scanning angles," *OSA Continuum*, volume 3, number 2, pages 253–266, 2020.

[50] Y. Li, X. Zhao, Y. Han, and P. Chen, "Improving CT quality for complex objects with the novel autoexposure imaging of stepped voltage scanning," *IEEE Transactions on Instrumentation and Measurement*, volume 72, pages 1–10, 2023.

[51] L. Ritschl, F. Bergner, C. Fleischmann, and M. Kachelrieß, "Water calibration for CT scanners with tube voltage modulation," *Phys. Med. Biol.*, volume 55, number 14, page 4107, 2010.

[52] J. Zou, X. Hu, H. Lv, and X. Hu, "An investigation of calibration phantoms for CT scanners with tube voltage modulation," *International Journal of Biomedical Imaging*, volume 2013, number 1, page 563 571, 2013.

[53] H. Haseljić, R. Frysch, V. Kulvait, T. Pfeiffer, B. Hensen, F. Wacker, I. Brüsch, T. Werncke, G. Rose, and D. Punzet, "The effect of x-ray tube voltage modulation to quality of perfusion images in cone beam C-arm CT," *SPIE Medical Imaging Proc.*, volume 12031, pages 542–546, 2022.

[54] T. P. Szczykutowicz and G.-H. Chen, "Dual energy CT using slow kVp switching acquisition and prior image constrained compressed sensing," *Phys. Med. Biol.*, volume 55, number 21, page 6411, 2010.

[55] L. Shen and Y. Xing, "Multienergy CT acquisition and reconstruction with a stepped tube potential scan," *Med. Phys.*, volume 42, number 1, pages 282–296, 2015.

[56] T. Su, J. Zhu, J. Yang, D. Liang, and Y. Ge, "Multi-material decomposition in spectral CT with angular tube voltage modulation," *SPIE Medical Imaging Proc.*, page 191, 2022.

[57] Y. Yang, S. Wang, G. M. Stevens, and A. S. Wang, "Tube voltage modulation for reducing noise in photon counting CT," *Conference Record of the 8th International Conference on Image Formation in X–Ray Computed Tomography*, volume 8, pages 102–105, 2024.

[58] K. B. Mathieu, A. C. Turner, M Khatonabadi, M. F. McNitt-Gray, C. H. Cagnon, and D. D. Cody, "Varying kVp as a means of reducing CT breast dose to pediatric patients," *Phys. Med. Biol.*, volume 58, number 13, pages 4455–4469, 2013.

[59] E. Baader, L. Klein, S. Sawall, J. Maier, and M. Kachelrieß, "CT tube current and tube voltage modulation to minimize the patient's radiation risk," *Insights into Imaging, ECR Book of Abstracts*, volume 14, number Supp. 4, 2023.

[60] E. Baader and M. Kachelrieß, "Tube voltage modulation for contrast-enhanced CT scans," *Conference Record of the 8th International Conference on Image Formation in X–Ray Computed Tomography*, volume 8, pages 198–200, 2024.

[61] R. H. Byrd, P. Lu, J. Nocedal, and C. Zhu, "A limited memory algorithm for bound constrained optimization," *SIAM Journal on Scientific Computing*, volume 16, number 5, pages 1190–1208, 1995.

[62] C. Zhu, R. H. Byrd, P. Lu, and J. Nocedal, "Algorithm 778: L-BFGS-B: Fortran subroutines for large-scale bound-constrained optimization," *ACM Trans. Math. Softw.*, volume 23, number 4, 550–560, 1997.

[63] O. Jimenez-del Toro, H. Müller, M. Krenn, K. Gruenberg, A. A. Taha, M. Winterstein, I. Eggel, A. Foncubierta-Rodríguez, O. Goksel, A. Jakab, G. Kontokotsios, G. Langs, B. H. Menze, T. Salas Fernandez, R. Schaer, A. Walleyo, M.-A. Weber, Y. Dicente Cid, T. Gass, M. Heinrich, F. Jia, F. Kahl, R. Kechichian, D. Mai, A. B. Spanier, G. Vincent, C. Wang, D. Wyeth, and A. Hanbury, "Cloud-based evaluation of anatomical structure segmentation and landmark detection algorithms: VISCERAL anatomy benchmarks," *IEEE Transactions on Medical Imaging*, volume 35, number 11, pages 2459–2475, 2016.

[64] P. Virtanen, R. Gommers, T. E. Oliphant, M. Haberland, T. Reddy, D. Cournapeau, E. Burovski, P. Peterson, W. Weckesser, J. Bright, S. J. van der Walt, M. Brett, J. Wilson, K. J. Millman, N. Mayorov, A. R. J. Nelson, E. Jones, R. Kern, E. Larson, C. J. Carey, İ. Polat, Y. Feng, E. W. Moore, J. VanderPlas, D. Laxalde, J. Perktold, R. Cimrman, I. Henriksen, E. A. Quintero, C. R. Harris, A. M. Archibald, A. H. Ribeiro, F. Pedregosa, P. van Mulbregt, and SciPy 1.0 Contributors, "SciPy 1.0: Fundamental Algorithms for Scientific Computing in Python," *Nature Methods*, volume 17, pages 261–272, 2020.

[65] E. Baader, L. Klein, J. Maier, S. Sawall, and M. Kachelrieß, "Patient radiation risk reduction by controlling the tube start angle in single and dual source spiral CT scans: A simulation study," *Med. Phys.*, volume 51, number 10, pages 7080–7092, 2024.

[66] D. Zhang, A. S. Savandi, J. J. Demarco, C. H. Cagnon, E. Angel, A. C. Turner, D. D. Cody, D. M. Stevens, A. N. Primak, C. H. McCollough, and M. F. McNitt-Gray, "Variability of surface and center position radiation dose in MDCT: Monte Carlo simulations using CTDI and anthropomorphic phantoms," *Med. Phys.*, volume 36, number 3, pages 1025–1038, 2009.

[67] K. Yang, X. Li, L. Yu, B. Li, T. A. Marschall, and B. Liu, "Visualization and comparison of CT dose distribution between axial and helical acquisitions," *Med. Phys.*, volume 50, number 8, pages 4797–4808, 2023.

[68] J. S. Muryn, A. G. Morgan, C. L. Liptak, F. F. Dong, W. P. Segars, A. N. Primak, and X. Li, "Analysis of uncertainties in Monte Carlo simulated organ and effective dose in chest CT: Scanner- and scan-related factors," *Phys. Med. Biol.*, volume 62, number 8, page 3175, 2017.

[69] M. Petersilka, H. Bruder, B. Krauss, K. Stierstorfer, and T. G. Flohr, "Technical principles of dual source CT," *European Journal of Radiology*, volume 68, number 3, pages 362–368, 2008.

[70] K. Boroto, M. Remy-Jardin, T. Flohr, J.-B. Faivre, V. Pansini, N. Tacelli, B. Schmidt, A. Gorgos, and J. Remy, "Thoracic applications of dual-source CT technology," *European Journal of Radiology*, volume 68, number 3, pages 375–384, 2008.

[71] V. Sandfort, M. A. Ahlman, E. C. Jones, M. Selwaness, M. Y. Chen, L. R. Folio, and D. A. Bluemke, "High pitch third generation dual-source CT: Coronary and cardiac visualization on routine chest CT," *Journal of Cardiovascular Computed Tomography*, volume 10, number 4, pages 282–288, 2016.

[72] Y. Chen, X. Zhang, H. Xue, Y. Zhu, Y. Wang, Y. Li, Z. Zhang, and Z. Jin, "Head and neck angiography at 70 kVp with a third-generation dual-source CT system in patients: Comparison with 100 kVp," *Neuroradiology*, volume 59, pages 1071–1081, 2017.

[73] A. Bedernik, W. Wuest, M. S. May, R. Heiss, M. Uder, and M. Wiesmueller, "Image quality comparison of single-energy and dual-energy computed tomography for head and neck patients: A prospective randomized study," *European Radiology*, volume 32, number 11, pages 7700–7709, 2022.

[74] A Eller, M Wiesmüller, W Wüst, R Heiss, M Kopp, M Saake, M Brand, M Uder, and M. May, "Carotid CTA at the lowest tube voltage (70 kV) in comparison with automated tube voltage adaption," *American Journal of Neuroradiology*, volume 40, number 8, pages 1374–1382, 2019.

[75] S. S. Hsieh and N. J. Pelc, "Algorithms for optimizing CT fluence control," *SPIE Medical Imaging Proc.*, volume 9033, page 90330M, 2014.

[76] D. Ketelsen, M. Buchgeister, M. Fenchel, B. Schmidt, T. G. Flohr, R. Syha, C. Thomas, I. Tsiflikas, C. D. Claussen, and M. Heuschmid, "Automated computed tomography dose-saving algorithm to protect radiosensitive tissues: Estimation of radiation exposure and image quality considerations," *Investigative Radiology*, volume 47, number 2, pages 148–152, 2012.

[77] C. H. McCollough, S. Leng, L. Yu, and J. G. Fletcher, "Dual- and multi-energy CT: Principles, technical approaches, and clinical applications," *Radiology*, volume 276, number 3, pages 637–653, 2015.

[78] J. C. Montoya, C. Zhang, Y. Li, K. Li, and G.-H. Chen, "Reconstruction of three-dimensional tomographic patient models for radiation dose modulation in CT from two scout views using deep learning," *Med. Phys.*, volume 49, number 2, pages 901–916, 2022.

[79] L. Shen, W. Zhao, and L. Xing, "Patient-specific reconstruction of volumetric computed tomography images from a single projection view via deep learning," *Nature Biomedical Engineering*, volume 3, number 11, pages 880–888, 2019.

[80] X. Ying, H. Guo, K. Ma, J. Wu, Z. Weng, and Y. Zheng, "X2CT-GAN: Reconstructing CT from biplanar x-rays with generative adversarial networks," in *Proceedings of the IEEE/CVF conference on computer vision and pattern recognition*, 2019, pages 10 619–10 628.

[81] C. Liu, L. Klein, Y. Huang, E. Baader, M. Lell, M. Kachelrieß, and A. Maier, "Two-view topogram-based anatomy-guided CT reconstruction for prospective risk minimization," *Scientific Reports*, volume 14, number 1, page 9373, 2024.

[82] "Lung screening at ultra low dose - made possible with 3D scanogram and silverbeam filter," *Visions*, volume 40, pages 60–62, 2023.

[83] L. J. Oostveen, S. Tunissen, and I. Sechopoulos, "Comparing organ and effective dose of various CT localizer acquisition strategies: A Monte Carlo study," *Med. Phys.*, volume 52, number 1, pages 576–584, 2025.

[84] E. Kollitz, H. Han, C. H. Kim, M. Pinto, M. Schwarz, M. Riboldi, F. Kamp, C. Belka, W. Newhauser, G. Dedes, and K. Parodi, "A patient-specific hybrid phantom for calculating radiation dose and equivalent dose to the whole body," *Phys. Med. Biol.*, volume 67, number 3, page 035 005, 2022.

[85] F. Geissler, R. Heiß, M. Kopp, M. Wiesmüller, M. Saake, W. Wuest, A. Wimmer, V. Prell, M. Uder, and M. S. May, "Personalisierte Computertomografie – automatisierte Abschätzung von Größe und Gewicht durch Simulation eines digitalen Zwillings mit einer 3D-Kamera und künstlicher Intelligenz," *RöFo*, volume 193, number 04, pages 437–445, 2021.

[86] S. Wang, M. J. Medrano, A. A. Z. Imran, W. Lee, J. J. Cao, G. M. Stevens, J. R. Tse, and A. S. Wang, "Automated estimation of individualized organ-specific dose and noise from clinical CT scans," *Phys. Med. Biol.*, volume 70, number 3, page 035 014, 2025.

[87] J. Wasserthal, H.-C. Breit, M. T. Meyer, M. Pradella, D. Hinck, A. W. Sauter, T. Heye, D. T. Boll, J. Cyriac, S. Yang, M. Bach, and M. Segeroth, "TotalSegmentator: Robust segmentation of 104 anatomic structures in CT images," *Radiology: Artificial Intelligence*, volume 5, number 5, e230024, 2023.

[88] J. Maier, L. Klein, E. Eulig, S. Sawall, and M. Kachelrieß, "Real-time estimation of patient-specific dose distributions for medical CT using the deep dose estimation," *Med. Phys.*, volume 49, number 4, pages 2259–2269, 2022.

[89] B. De Man, M. Wu, P. FitzGerald, M. Kalra, and Z. Yin, "Dose reconstruction for real-time patient-specific dose estimation in CT," *Med. Phys.*, volume 42, number 5, pages 2740–2751, 2015.

[90] M. Medrano, S. Wang, A. A. Z. Imran, G. Stevens, J. R. Tse, and A. Wang, "Personalized, scout-based dose estimation for prospective optimization of CT tube current modulation," *SPIE Medical Imaging Proc.*, volume 12925, 129251J, 2024.

[91] A. A. Z. Imran, D. Pal, S. Wang, S. Dutta, E. Zucker, and A. Wang, "Personalized CT organ noise estimation from scout images," *SPIE Medical Imaging Proc.*, volume 12031, 120310R, 2022.

[92] S. Wang, M. J. Medrano, J. J. Cao, W. Lee, G. M. Stevens, J. R. Tse, and A. S. Wang, "Learned tube current modulation from scout images for individualized organ-level CT dose and image quality," *Conference Record of the 8th International Conference on Image Formation in X–Ray Computed Tomography*, volume 8, pages 320–323, 2024.

[93] S. Klubertz, E. Baader, and M. Kachelrieß, "Do we need age- and sex-dependent organ weights for the risk-specific tube current modulation (riskTCM) in diagnostic CT?" *Abstracts of the 5th European Congress of Medical Physics in Physica Medica*, volume 125, page 103 537, 2024.

[94] S. Klubertz, "Investigation of age- and sex-dependent organ weights for the risk-specific tube current modulation (riskTCM) in comparison to the effective dose," M.S. thesis, Heidelberg University, 2024.

[95] J. C. Ocampo Ramos, L. M. Carter, J. L. Brown, H. Marquis, C. F. Uribe, P. B. Zanzonico, W. E. Bolch, and A. L. Kesner, "The risk index as a basis for risk/benefit analyses and protocol optimization in diagnostic nuclear imaging," *Med. Phys.*, volume 50, number 12, pages 7390–7399, 2023.

[96] J. Steidel, J. Maier, S. Sawall, and M. Kachelrieß, "Dose reduction potential in diagnostic single energy CT through patient-specific prefilters and a wider range of tube voltages," *Med. Phys.*, volume 49, number 1, pages 93–106, 2022.

[97] G. J. Gang, A. Mao, W. Wang, J. H. Siewerdsen, A. Mathews, S. Kawamoto, R. Levinson, and J. W. Stayman, "Dynamic fluence field modulation in computed tomography using multiple aperture devices," *Phys. Med. Biol.*, volume 64, number 10, page 105 024, 2019.

[98] S. M. Huck, G. S. Fung, K. Parodi, and K. Stierstorfer, "On the potential of ROI imaging in x-ray CT – a comparison of novel dynamic beam attenuators with current technology," *Med. Phys.*, volume 48, number 7, pages 3479–3499, 2021.

Acknowledgments

I would like to take the opportunity to thank everyone who made this dissertation possible and supported me in the process:

I am grateful for the DKFZ International PhD Program Fellowship which allowed me to choose a group and a topic for my thesis at the DKFZ. Furthermore, I want to thank the team of the PhD program office and the career service at DKFZ for their support.

I want to thank Prof. Dr. Marc Kachelrieß for the opportunity to work with him, his openness in the choice of the topic and his scientific supervision and guidance with numerous and often spontaneous meetings.

I want to thank Prof. Dr. Mark Ladd for agreeing to be the first examiner of my thesis and for sharing his thoughts in the meetings with my thesis advisory committee.

I want to thank Prof. Dr. Jürgen Hesser for being a member of my thesis advisory committee and the discussions during the meetings.

I want to thank Prof. Dr. Loredana Gastaldo and Prof. Dr. Joerg Jaeckel for agreeing to serve as examiners for the oral defense.

I want to thank all current and former members of the division of X-ray imaging and CT at the DKFZ for the pleasant and supportive working environment. In particular, I want to thank Dr. Joscha Maier and Dr. Stefan Sawall for their helpfulness and for sharing their expertise with me. Moreover, I want to thank the Bachelor and Master students Johanna, Lennard, Moritz, Sophia, and Philipp. I was privileged to work with them and our many discussions helped me deepen my knowledge and understanding.

Furthermore, I am grateful to everyone who made me feel welcome and at home in Heidelberg during the last three years. The foundation for this was laid by my flatmates, who created a space in which I felt comfortable and felt home every time entering our flat and speaking with them. I am glad for having and having had such caring flatmates! Moreover, I am grateful to the DKFZ PhD council and especially the social events and networking team for organizing so many great events to meet and

catch up with people. I am very happy about the great friendships that have developed from those events. I am also very grateful to all the volunteers, trainers, and training colleagues of the sports clubs I joined who contributed to my physical and mental well-being through the sports offer, the community, the exciting tournaments, and the amazing training camps.

Finally, I want to thank my family and all my friends in and outside Heidelberg who fill my life with joy and support me. I would especially like to thank my family for their constant support.

The Monte Carlo dose estimation method RayConStruct-MC, parts of the projection simulation software RayConstruct-PS, and the image reconstruction software RayConStruct-IR were provided by RayConStruct® GmbH, Nürnberg, Germany.

I hereby assure, that I composed this work by myself and did not use any other than the listed resources.

Heidelberg, March 24, 2025